

MODELLING AND SIMULATION OF FRICTION
IN DEEP DRAWING

A THESIS SUBMITTED TO
THE GRADUATE SCHOOL OF NATURAL AND APPLIED SCIENCES
OF
MIDDLE EAST TECHNICAL UNIVERSITY

BY

MURAT BAŞPINAR

IN PARTIAL FULFILLMENT OF THE REQUIREMENTS
FOR
THE DEGREE OF MASTER OF SCIENCE
IN
MECHANICAL ENGINEERING

SEPTEMBER 2011

Approval of the thesis:

**MODELLING AND SIMULATION OF FRICTION
IN DEEP DRAWING**

submitted by **Murat BAŞPINAR** in partial fulfillment of the requirements for the degree of **Master of Science in Mechanical Engineering Department, Middle East Technical University** by,

Prof. Dr. Canan Özgen
Dean, Graduate School of **Natural and Applied Sciences**

Prof. Dr. Suha Oral
Head of Department, **Mechanical Engineering**

Prof. Dr. Metin Akkök
Supervisor, **Mechanical Engineering Dept., METU**

Examining Comittee Members:

Prof. Dr. Mustafa İlhan Gökler
Mechanical Engineering Dept., METU

Prof. Dr. Metin Akkök
Mechanical Engineering Dept., METU

Prof. Dr. Haluk Darendeliler
Mechanical Engineering Dept., METU

Prof. Dr. Müfit Gülgeç
Mechatronic Engineering Dept., Çankaya University

Prof. Dr. Suat Kadioğlu
Mechanical Engineering Dept., METU

Date: 06/09/2011

I hereby declare that all information in this document has been obtained and presented in accordance with academic rules and ethical conduct. I also declare that, as required by these rules and conduct, I have fully cited and referenced all material and results that are not original to this work.

Name, Last Name : Murat Bařpınar

Signature :

ABSTRACT

MODELLING AND SIMULATION OF FRICTION IN DEEP DRAWING

Başpınar, Murat

M.Sc., Department of Mechanical Engineering

Supervisor: Prof. Dr. Metin Akkök

September 2011, 139 pages

Different contact surface parameters and operating characteristics are observed during the deep drawing process. It is not possible to find a formulation that can be used for all lubrication regimes. Therefore, several friction models have been developed in order to overcome this problem. In this study, a math program is developed which combines Wilson's and Khonsari's friction models in a new model in order to increase accuracy and efficiency in friction calculations. By comparing the results of both friction models, the film thickness ratio of 0.035 is introduced for 0.15 μm standard deviation of surface summits. Below the ratio of 0.035, Khonsari's model gives more accurate results since asperity friction is dominant and the model is based on asperity contact. Above the ratio of 0.035, Wilson's model gives more accurate results since hydrodynamic friction is dominant and the model is based on lubricant flow.

In this study, a finite element program is used to simulate $\text{Ø}48$ mm cylindrical and 50.5×50.5 mm square shallow drawing processes which are performed in single stage. The final cup depths are selected as 18 mm and 23 mm for square and

cylindrical cup drawing respectively. The FEM model and the program codes developed are verified by the previous studies in literature. After verification, the simulation results of the cylindrical and square cup drawing are input to a math program which calculates local friction coefficients using the combined friction model. Finally, the combined friction model and the results are further discussed.

Keywords: Friction, modeling, deep drawing, cylindrical cup drawing, square cup drawing.

ÖZ

DERİN ÇEKMEDE SÜRTÜNMENİN MODELLENMESİ VE SİMÜLASYONU

Başpınar, Murat

Yüksek Lisans, Makina Mühendisliği Bölümü

Tez Yöneticisi: Prof. Dr. Metin Akkök

Eylül 2011, 139 sayfa

Derin çekme işlemi sırasında değişik temas yüzeyi parametreleri ve işlem karakteristikleri görülmektedir. Bütün yağlama rejimlerini kapsayabilecek herhangi bir formülasyonun bulunması mümkün değildir. Bu nedenle, bu problemi aşmak için birkaç sürtünme modeli geliştirilmiştir. Bu çalışmada, sürtünme hesaplamalarında hassasiyet ve verimi arttırmak amacıyla, Wilson ve Khonsari'nin sürtünme modellerini yeni bir model altında bileştiren, bir matematik programı geliştirilmiştir. Derin çekmede, sürtünme modellerinden elde edilen sonuçlar karşılaştırılarak, 0.035 film kalınlığı oranı, yüzey tepelerinin dağılımının standart sapması 0.15 μm için belirlenmiştir. 0.035 oranının altında, pürüzlerden doğan sürtünme baskın olduğu için Khonsari modeli daha hassas sonuçlar vermektedir çünkü, model pürüzlerin temasını baz almaktadır. 0.035 oranının üstünde, hidrodinamik sürtünme baskın olduğu için Wilson modeli daha hassas sonuçlar vermektedir çünkü, model yağ akışını baz almaktadır.

Bu çalışmada, $\varnothing 48$ mm'lik silindirik ve 50.5×50.5 mm'lik kare kabın tek seferde çekimini simule etmesi için sonlu elemanlar programı kullanılmıştır. Kapların son

derinliđi sırasıyla kare ve silindirik kap çekme için 18 mm ve 23 mm olarak seçilmiştir. Sonlu elemanlar modeli ve program kodları, literatürdeki sonuçlarla doğrulanmıştır. Doğrulamadan sonra, silindirik ve kare kap çekme simülasyon sonuçları, geliştirilen bir matematik programına girilerek, lokal sürtünme katsayılarının hesaplanmasında kullanılmıştır. Son olarak, birleşik model ve sonuçlar ayrıntısıyla tartışılmıştır.

Anahtar Kelimeler: Sürtünme, modelleme, derin çekme, silindirik kap çekme, kare kap çekme

To My Family

ACKNOWLEDGEMENTS

The author wishes to express his gratitude to his supervisor Prof. Dr. Metin Akkök who offered invaluable support, guidance and criticism which formed the basis of this work.

The author would also like to thank his family and colleagues for their patience and support throughout this work.

TABLE OF CONTENTS

ABSTRACT	iv
ÖZ	vi
ACKNOWLEDGEMENTS	ix
TABLE OF CONTENTS	x
LIST OF TABLES	xiii
LIST OF FIGURES	xiv
LIST OF SYMBOLS	xviii
CHAPTERS	
1. INTRODUCTION	1
1.1 Friction and Lubrication in Metal Forming Operations	1
1.2 The Stribeck Curve and Lubrication Regimes	2
1.3 Objective of This Research.....	5
2. DEEP DRAWING AND FRICTION.....	7
2.1 Deep Drawing and the Tribological System.....	7
2.2 Surface Roughness and Rough Surface Contact in Tribology	9
2.2.1 Surface Roughness.....	9
2.2.2 Rough Surface Contact	13
2.3 Tribology in Deep Drawing.....	14
2.3.1 Contact Regions in Deep Drawing	15
2.3.2 General Characteristics of Deep Drawing	18
3. MODELING OF FRICTION ON LUBRICATED ROUGH SURFACES.....	19
3.1 Literature Survey on Rough Contact	19

3.2 Hertzian Contact Theory.....	26
3.3 Rough Surface Friction Models.....	28
3.3.1 Wilson’s Friction Model.....	29
3.3.2 Khonsari’s Friction Model.....	35
4. SIMULATION OF LUBRICATED ROUGH SURFACE FRICTION MODELS.....	41
4.1 Deep Drawing Components.....	41
4.2 FEM Model of Cylindrical Cup Drawing.....	43
4.3 FEM Program Validation	45
4.4 Friction Models Code Validation	49
4.4.1 Code of Khonsari’s Friction Model	50
4.4.2 Code of Wilson’s Friction Model	52
4.5 Simulation Results for Cylindrical Cup Drawing.....	52
4.5.1 Von-Mises Stress Distribution.....	55
4.5.2 Strain Distribution.....	56
4.5.3 Thickness Distribution	57
4.5.4 Punch Force Variation	58
4.5.5 Variation of Coefficient of Friction	59
4.5 The Combined Friction Model	66
4.7 Parameters for Cylindrical Cup Drawing.....	69
4.8 Results of the Combined Friction Model.....	69
5. CASE STUDY: SQUARE CUP DRAWING	72
5.1 Deep Drawing Components.....	72
5.2 FEM Model of Square Cup Drawing.....	74
5.3 Parameters for Square Cup Drawing	76
5.4 Simulation Results for Square Cup Drawing	77

5.4.1 Von-Mises Stress Distribution.....	80
5.4.2 Strain Distribution.....	81
5.4.3 Thickness Distribution.....	84
5.4.4 Punch Force Variation.....	86
5.4.5 Variation of Coefficient of Friction.....	87
6. FACTORS AFFECTING DEEP DRAWING PROCESS.....	96
6.1 Deep Drawing Parameters.....	96
6.1.1 The Effect of Coefficient of Friction on Deep Drawing.....	97
6.1.2 The Effect of Clamping Force on Deep Drawing.....	106
6.2 Discussion of Results.....	113
7. CONCLUSIONS AND RECOMMENDATIONS.....	115
7.1 Conclusions.....	115
7.2 Recommendations for Future Work.....	116
REFERENCES.....	112
APPENDICES.....	115
A. RADIUS OF CURVATURE CALCULATION STEPS.....	121
B. CALCULATION OF THE LOCAL VELOCITIES.....	122
C. SAMPLE COEFFICIENT OF FRICTION INPUT FOR LS-DYNA.....	125
D. CODE OF COMBINED FRICTION MODEL.....	127

LIST OF TABLES

TABLES

Table 2.1 Probability density functions for different skewness and kurtosis values [6]	11
Table 3.1 Hertzian contact formulas for point and line contacts [20].....	28
Table 4.1 Spur gear contact parameters [27]	51
Table 4.2 Axisymmetric deep drawing process parameters [4].....	52
Table 4.3 Cylindrical cup drawing process parameters	69
Table 5.1 Square cup drawing process parameters	77

LIST OF FIGURES

FIGURES

Figure 1.1 Stribeck curve [2]	3
Figure 1.2 Boundary lubrication (BL), mixed lubrication (ML) and hydrodynamic lubrication (HL) representation.....	4
Figure 2.1 Stages of deep drawing process.....	9
Figure 2.2 (a) Probability density function distribution with varying skewness (b) kurtosis [6]	11
Figure 2.3 Mean line representation.....	12
Figure 2.4 Contact regions in deep drawing	15
Figure 2.5 Free deformation zones in deep drawing [8]	17
Figure 3.1 Contact between elastic rough, soft surface and rigid smooth surface.....	20
Figure 3.2 Wedge-shaped, infinitely long asperities.....	24
Figure 3.3 Hertzian contact types (a) point contact (b) line contact	26
Figure 3.4 Equivalent radius representations	27
Figure 3.5 Flow chart of Wilson’s friction model [1].....	34
Figure 3.6 Flow chart of Khonsari’s friction model [33].....	40
Figure 4.1 Tool geometry of cylindrical cup drawing	42
Figure 4.2 FEM model for cylindrical cup drawing	43
Figure 4.3 BC defined node set.....	45
Figure 4.4 Radial strain distributions at 18 mm and 23 mm cup depths ($f_p=0.15$, $f_{die}=0.05$, $f_{bh}=0.05$)	46
Figure 4.5 Circumferential strain distributions at 18 mm and 23 mm cup depths ($f_p=0.15$, $f_{die}=0.05$, $f_{bh}=0.05$)	48
Figure 4.6 Thickness strain distributions at 18 mm and 23 mm cup depths ($f_p=0.15$, $f_{die}=0.05$, $f_{bh}=0.05$)	49
Figure 4.7 Stribeck curve for the data given in Table 4.1	51
Figure 4.8 (a) Initial and (b) final (18 mm cup depth) blank geometries of cylindrical cup drawing.....	53

Figure 4.9 Kinetic and internal energy variation for cylindrical cup drawing.....	54
Figure 4.10 Von-Mises stress distribution for cylindrical cup drawing at 18 mm cup depth ($f_{die}=0.05$, $f_{bh}=0.05$)	55
Figure 4.11 Effective strain distribution for cylindrical cup drawing at 18 mm cup depth ($f_{die}=0.05$, $f_{bh}=0.05$)	56
Figure 4.12 Thickness variations in the radial direction for cylindrical cup drawing at 18 mm cup depth ($f_{die}=0.05$, $f_{bh}=0.05$)	58
Figure 4.13 Variation of punch force in cylindrical cup drawing ($f_{die}=0.05$, $f_{bh}=0.05$)	59
Figure 4.14 Pressure distribution for cylindrical cup drawing at 18 mm cup depth ($f_{die}=0.05$, $f_{bh}=0.05$)	60
Figure 4.15 Average and relative velocity variations for cylindrical cup drawing at 18 mm cup depth ($f_{die}=0.05$, $f_{bh}=0.05$)	61
Figure 4.16 Film thickness variation for cylindrical cup drawing at 18 mm cup depth ($f_{die}=0.05$, $f_{bh}=0.05$)	62
Figure 4.17 Film thickness ratio (h/σ) variation for cylindrical cup drawing at 18 mm cup depth ($f_{die}=0.05$, $f_{bh}=0.05$)	63
Figure 4.18 Scaling factor variations for cylindrical cup drawing at 18 mm cup depth ($f_{die}=0.05$, $f_{bh}=0.05$)	64
Figure 4.19 Variation of local friction coefficient for cylindrical cup drawing at 18 mm cup depth ($f_{die}=0.05$, $f_{bh}=0.05$)	66
Figure 4.20 Flow chart of the combined friction model	68
Figure 4.21 Variation of local friction coefficient for cylindrical cup drawing at cup depths of 6 mm, 12 mm and 18 mm ($f_{die}=0.05$, $f_{bh}=0.05$).....	70
Figure 5.1 Tool geometry of square cup drawing.....	73
Figure 5.2 FEM model for square cup drawing	75
Figure 5.3 BC defined node set for square cup drawing.....	76
Figure 5.4 (a) Initial and (b) final (18 mm cup depth) blank geometries of square cup drawing.....	78
Figure 5.5 0° and 45° directions of blank in square cup drawing.....	79
Figure 5.6 Kinetic and internal energy variation for square cup drawing	79

Figure 5.7 Von-Mises stress distribution for square cup drawing at 18 mm cup depth ($f_{die}=0.05, f_{bh}=0.05$)	80
Figure 5.8 Thickness strain distributions for square cup drawing along 0° and 45° directions at 18 mm cup depth ($f_{die}=0.05, f_{bh}=0.05$)	81
Figure 5.9 Strain distributions in rolling direction for square cup drawing along 0° and 45° directions at 18 mm cup depth ($f_{die}=0.05, f_{bh}=0.05$)	83
Figure 5.10 Effective strain distribution for square cup drawing at 18 mm cup depth ($f_{die}=0.05, f_{bh}=0.05$)	84
Figure 5.11 Thickness change along 0° and 45° directions for square cup drawing at 18 mm cup depth ($f_{die}=0.05, f_{bh}=0.05$)	85
Figure 5.12 Variation of punch force in square cup drawing ($f_{die}=0.05, f_{bh}=0.05$)....	86
Figure 5.13 Pressure distributions for square cup drawing along 0° and 45° directions ($f_{die}=0.05, f_{bh}=0.05$)	87
Figure 5.14 Average and relative velocity variations for square cup drawing (a) along 0° direction (b) along 45° direction at 18 mm cup depth ($f_{die}=0.05, f_{bh}=0.05$)	89
Figure 5.15 Film thickness variation along 0° and 45° directions for square cup drawing at 18 mm cup depth ($f_{die}=0.05, f_{bh}=0.05$)	90
Figure 5.16 Film thickness ratio (h/σ) variation for square cup drawing at 18 mm cup depth ($f_{die}=0.05, f_{bh}=0.05$)	91
Figure 5.17 Scaling factor variation for square cup drawing (a) along 0° direction (b) along 45° direction at 18 mm cup depth ($f_{die}=0.05, f_{bh}=0.05$)	92
Figure 5.18 Variation of local friction coefficient for square cup drawing (a) along 0° direction (b) along 45° direction at cup depths of 6 mm, 12 mm and 18 mm ($f_{die}=0.05, f_{bh}=0.05$)	94
Figure 6.1 Blank thickness deviations at different punch surface friction coefficients for square cup drawing (a) along 0° direction (b) along 45° direction at 18 mm cup depth ($f_{die}=0.05, f_{bh}=0.05$)	98
Figure 6.2 Blank thickness deviations at different punch surface friction coefficients for cylindrical cup drawing at 18 mm cup depth ($f_{die}=0.05, f_{bh}=0.05$).....	100
Figure 6.3 Punch force variations at different punch surface friction coefficients for square cup drawing ($f_{die}=0.05, f_{bh}=0.05$).....	100

Figure 6.4 Punch force variations at different punch surface friction coefficients for cylindrical cup drawing ($f_{die}=0.05$, $f_{bh}=0.05$).....	101
Figure 6.5 Blank thickness deviations at different blank holder and die interface friction coefficients for square cup drawing (a) along 0° direction (b) along 45° direction at 18 mm cup depth ($f_p=0.15$)	102
Figure 6.6 Blank thickness deviations at different blank holder and die interface friction coefficients for cylindrical cup drawing at 18 mm cup depth ($f_p=0.15$)	104
Figure 6.7 Punch force variations at different blank holder and die interface friction coefficients for square cup drawing ($f_p=0.15$).....	105
Figure 6.8 Punch force variations at different blank holder and die interface friction coefficients for cylindrical cup drawing ($f_p=0.15$).....	106
Figure 6.9 Blank thickness deviations at different clamping forces for square cup drawing (a) along 0° direction (b) along 45° direction at 18 mm cup depth ($f_p=0.15$, $f_{die}=0.05$, $f_{bh}=0.05$)	107
Figure 6.10 Blank thickness deviations at different clamping forces for cylindrical cup drawing at 18 mm cup depth ($f_p=0.15$, $f_{die}=0.05$, $f_{bh}=0.05$)	109
Figure 6.11 Punch force variations at different clamping forces for square cup drawing ($f_p=0.15$, $f_{die}=0.05$, $f_{bh}=0.05$).....	110
Figure 6.12 Punch force variations at different clamping forces for cylindrical cup drawing ($f_p=0.15$, $f_{die}=0.05$, $f_{bh}=0.05$).....	111
Figure 6.13 Local friction coefficient variations at different clamping forces for square cup drawing along 45° direction ($f_{die}=0.05$, $f_{bh}=0.05$).....	111
Figure 6.14 Local friction coefficient variations at different clamping forces for cylindrical cup drawing ($f_{die}=0.05$, $f_{bh}=0.05$).....	112
Figure B.1 Local velocities at the punch radius contact	123
Figure B.2 Local velocities at the die radius contact	123
Figure C.1 Friction input data for LS-Dyna.....	125
Figure C.2 Stribeck curves at different pressures	126

LIST OF SYMBOLS

a	: Half width of Hertzian contact
A	: Fractional contact area
B	: Length of line contact
c	: Adhesion coefficient
d_d	: Distance between mean line of summits and mean line of smooth surface
E_1	: Modulus of elasticity of surface 1
E_2	: Modulus of elasticity of surface 2
\bar{E}	: Non-dimensional strain rate
E'	: Effective modulus of elasticity
f_c	: Friction coefficient in BL regime
f_p	: Friction coefficient at punch interface
f_{bh}	: Friction coefficient at blank holder interface
$F_{f,H}$: Hydrodynamic friction force
$F_{f,C}$: Asperity contact friction force
F_C	: Asperity contact force
F_H	: Hydrodynamic force
F_{sq}	: Squeeze force
F_S	: Steady load
F_T	: Total load

- h : Mean lubricant film thickness
- H_{eff} : Non-dimensional effective hardness
- k : Sheet shear strength
- l : Length of line contact
- l_{asp} : Asperity half spacing
- \mathcal{L} : Lubrication number
- n : Density of asperities
- p_f : Fluid film pressure
- p_h : Hydrodynamic pressure
- p_H : Maximum Hertzian pressure
- p_m : Average pressure of the Hertzian contact
- p_T : Sum of asperity and fluid pressure
- R : Equivalent radius
- R_a : CLA surface roughness
- R_q : RMS surface roughness
- u_s : Sliding velocity
- w : Load per unit length
- z : Non-dimensional film thickness
- α : Pressure-viscosity index
- β : Average radius of the spherical asperities
- β_0 : The rate of limiting shear stress versus pressure

- γ_1 : Scaling factor for asperity contact load
 γ_2 : Scaling factor for hydrodynamic load
 $\dot{\epsilon}$: Sheet strain rate
 θ_t : Mean slope of tooling asperities
 μ : Dynamic viscosity
 μ_0 : Oil viscosity at inlet temperature
 ν_1 : Poisson's ratio of surface 1
 ν_2 : Poisson's ratio of surface 2
 σ : Combined surface roughness
 σ_s : Standard deviation of summits
 τ_a : Adhesion friction stress component
 τ_f : Friction stress
 τ_h : Hydrodynamic friction
 τ_p : Plowing friction stress component
 τ_0 : Eyring shear stress
 τ_{L0} : Limiting shear stress at ambient temperature
 ϕ_f : Shear stress factor

CHAPTER 1

INTRODUCTION

1.1 Friction and Lubrication in Metal Forming Operations

In metal forming processes, friction is an important factor which affects the loads (punch and clamping forces), stresses, strain distribution, metal flow, energy consumption and surface quality of the products. Among the metal forming processes, friction and lubrication are very important in deep drawing process. Strain distribution is strongly affected by the friction, since the sheet metal cross-sectional area is very small compared to the contact area with the tool. Thus, the formability of sheet metal depends on the friction at the tooling/workpiece interface in addition to its material properties [1].

Coefficient of friction is not a constant through the whole contact surface for lubricated contacts. In fact, different friction coefficients can be calculated locally by using the friction models available in tribology literature. The reason is that, internal and environmental conditions at a contact may vary in a wide range.

Surface quality of the products is influenced by the lubrication regime. Using thick lubricant film reduces the metal-to-metal contact and tooling wear but, it causes a rough product surface due to insufficient constraint by the tooling. In case of using insufficient lubricant, surface quality is decreased due to scoring and other surface defects. Therefore, lubrication system must be carefully controlled in order to achieve the optimum friction level at the tooling/workpiece interface and increase the production efficiency.

Tribology is a study of interacting surfaces in motion relative to each other. Friction is a branch of tribology and deep drawing set-up can be classified as a tribological system. Tribology has an extreme importance in technology since it has a wide application area from chemistry to physics. At the beginning of tribology, the area of interest was limited to reduce wear in bearings and gears. Hydrodynamic lubrication was the aim of the tribologists and studies were concentrated around this topic. Tribological systems were designed to operate in hydrodynamic lubrication in order to eliminate wear in which there is no physical contact. Recently more research and experiments are directed to mixed lubrication.

1.2 The Stribeck Curve and Lubrication Regimes

When two surfaces slide along each other, different lubrication regimes can be distinguished at the interface. The Stribeck Curve is a common diagram used in tribology literature. It is used to determine the lubrication regime a contact operates. It is a plot of friction with respect to variables such as film thickness ratio (h/σ), velocity (V) or non-dimensional parameters. One of the most common non-dimensional parameter, denoted by \mathcal{L} , can be written as [2]

$$\mathcal{L} = \frac{\mu_0 u_s}{p_{av} R_a} \quad (1.1)$$

where η_0 is the viscosity of the lubricant at inlet conditions, u_s is the sliding velocity, p_{av} is the average pressure and R_a is the surface roughness. This non-dimensional parameter is also used in this study.

Lubrication regime is divided into four main parts which are called as boundary, mixed, thin film and thick film regimes. These regimes can be observed on a generalized Stribeck curve as shown in Figure 1.1. Thin and thick film regimes are sometimes combined and called as the hydrodynamic regime. The lubrication regime is mainly decided by the local film thickness to the combined roughness of the two

surfaces. Deep drawing process, subject of this study, is mostly in the boundary lubrication regime or mixed lubrication regime.

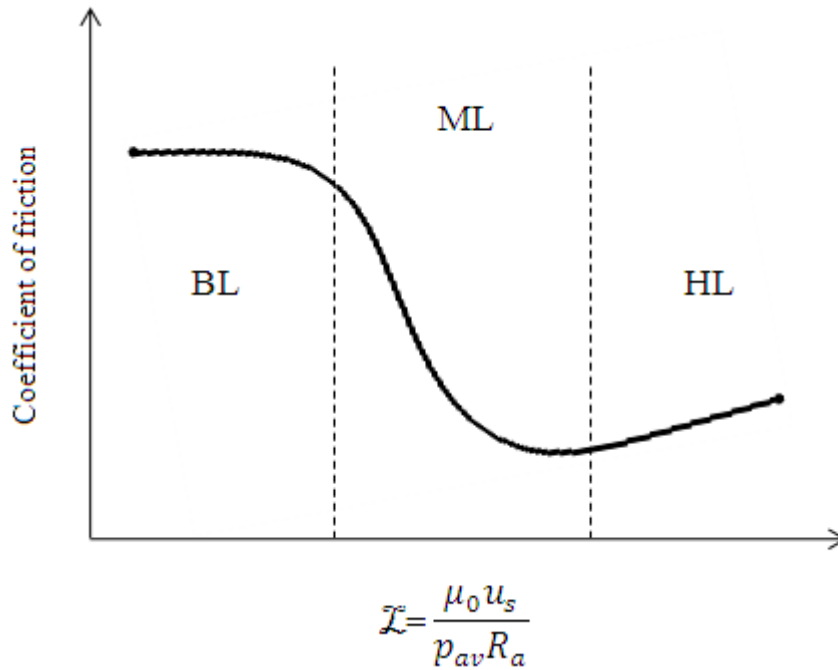


Figure 1.1 Stribeck curve [2]

Hydrodynamic Lubrication (HL): In hydrodynamic lubrication, the tool and the workpiece are separated by a film of lubricant and surfaces do not contact. There is only hydrodynamic component of friction. But, in this case there is not sufficient control of the surface roughness due to separation. Therefore, most of the processes tend to operate in the ML regime.

Mixed Lubrication (ML): In the mixed lubrication regime two surfaces are partly separated and partly in contact. Some portion of the load is carried by contacting asperities and the rest of the load is carried by the lubricant film.

Boundary Lubrication (BL): In the boundary lubrication regime, two surfaces are mostly in contact and the whole load is carried by the asperities. Dry friction between the asperities of both surfaces is prevented by thin boundary layers. In this regime, it is assumed that only the adhesion and plowing friction components are effective. In the BL and most of the ML regime the asperity friction is dominant while at the end of the ML regime and whole part of the HL regime, the hydrodynamic friction is dominant. Schematic representations of the three different lubrication regimes are shown in Figure 1.2.

Friction tests carried out by Emmens [3] shows that, the variation of pressure in steel blank drawing does not affect the Stribeck curve as much as aluminum blank drawing. Another factor that affects curve is the roughness characteristics of the blank which can be controlled by the sheet metal supplier and its manufacturing method. Experiments showed that the curve shifts to the right with increasing roughness and vice versa.

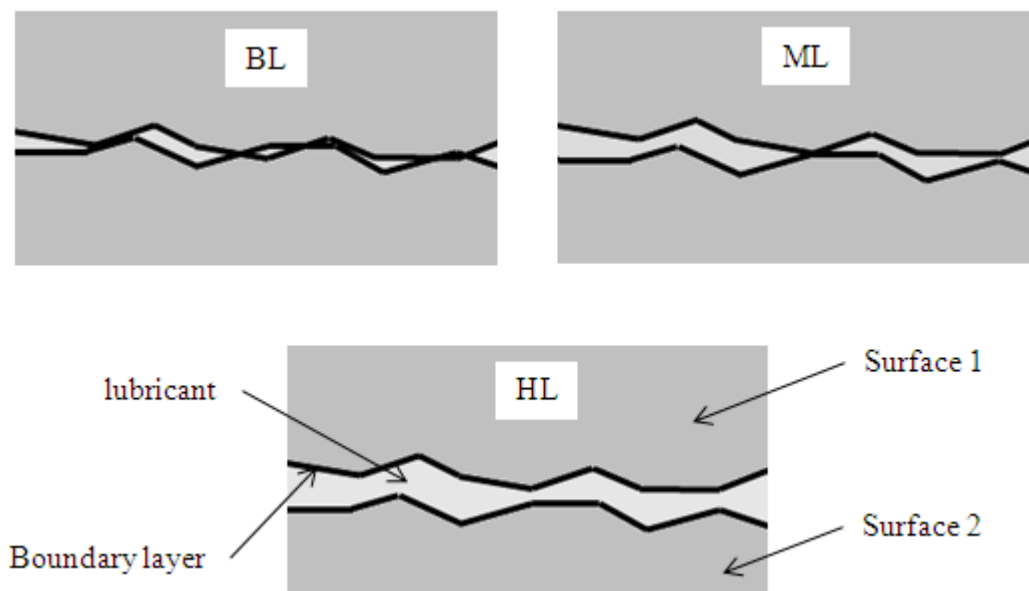


Figure 1.2 Boundary lubrication (BL), mixed lubrication (ML) and hydrodynamic lubrication (HL) representation

There are many parameters affecting the friction such as film thickness ratio, applied load, lubricant viscosity, surface roughness of the workpiece and tooling. In the BL regime, increasing the applied load causes more asperities to contact and this results a higher coefficient of friction. But, in the HL regime, the effect of the load is opposite. Increasing the load causes a decrease in the film thickness and as a result, coefficient of friction decreases. For a rough surface, higher film thickness is required to separate the asperities of both surfaces. Therefore, there will be more metal-to-metal contact under the same operating conditions. As a result, higher surface roughness increases the coefficient of friction.

In the BL regime, the chemical composition of the lubricant is important instead of its viscosity. As the viscosity decreases, metal-to-metal contact increases and higher friction coefficients are obtained in the ML regime. In the HL regime, lower viscosity causes the lubricant shear stress and coefficient of friction to decrease because; the coefficient of friction is directly proportional to the viscosity in this regime.

1.3 Objective of This Research

As it was noted earlier, there are different friction and lubrication regimes observed during deep drawing process. A better understanding of the friction and other parameters is needed to control the process and deformation. The main objective of this thesis is to minimize the necessity of experimental works which are more costly than running computer programs. Also, the results are obtained in a shorter time which is crucial for production. Therefore, it is aimed to obtain an improved friction model which can be coupled with simulation programs.

Cylindrical and square cup drawing are the most popular and simple deep drawing types. Firstly, cylindrical type is chosen to be investigated in this thesis because, it is easier and less critical than square cup drawing. The reason is that, there is tangential

symmetry in cylindrical cup drawing which gives the ability to analyze only a wedge-shaped sector of the blank. Then, square type is investigated as a case study, which is more difficult to handle parameters and takes more time to simulate.

In this study; variable friction models developed by Wilson and Khonsari are compared by applying to a cylindrical cup drawing simulation in Chapter 4. Then, a combined model is introduced which is a combination of the Wilson's and Khonsari's friction models. Forming processes are simulated by LS-Dyna, which is a transient dynamic finite element program, and outputs of the simulation are input to MATLAB in which the friction models are integrated. Additionally, the combined friction model is applied to a square cup drawing process in Chapter 5.

It is important to note that, some of the parameters of deep drawing process are not considered due to some simplifications. The reason is that, calculation of too many parameters cannot be handled by a single friction model. Important factors such as wear and dry friction are not included in friction models.

CHAPTER 2

DEEP DRAWING AND FRICTION

In this chapter, brief information is given about the theory of friction and deep drawing process. The properties of the tribological system to be investigated in this study are explained. Additionally, some parameters affecting tribology and friction are further discussed.

2.1 Deep Drawing and the Tribological System

Deep drawing is a process where the sheet metal is drawn into a forming die by the movement of a punch until final shape is obtained. The shape of the final product is determined by the geometry of the punch and forming die. Therefore, different tools are needed for products with different geometries. The process is called as “deep” drawing when the cup depth is larger than the minimum dimension of the die opening. The blank holder is pressed to the part of the blank which is not drawn by the punch and it avoids wrinkling. It also controls the material flow by letting the sheet metal to slide into the die radius which is different than stretch forming.

Softer materials such as aluminum and steel sheets are preferred as the blank material in order to deform easily and decrease the punch force. Tool and carbon steels are mostly used as the punch and die material. Tool steel is preferred for heavy duty jobs because it is harder than carbon steels. Another approach is to harden the soft tool material by coating with a harder material such as TiN, TiC or TiCN. Sheet metals are protected against corrosion by oil layers. Before the process, oil layers are

removed and deep drawing oils are applied in order to obtain a well lubricated contact between surfaces. After the process, drawn part is cleaned and another oil layer is applied to prevent corrosion. Nowadays, corrosion preventive oils also have lubrication properties. Thus, oil cleaning stages are eliminated which is a time-saving improvement. But, they are not efficient as much as the original deep drawing oils. Phosphates, heavy-duty emulsions, lead and wax films are some of the lubricant types used in deep drawing. Lubricant usage is also useful while pulling back the punch at the end of the process.

The schematic representations of stages in cylindrical cup drawing are shown in Figure 2.1. In the first stage, lubricant is applied to the blank in order to reduce the friction between the blank, punch and forming die. In the second stage, the clamping force is applied to the blank holder. Then, the punch is drawn until the desired shape is obtained in the third stage. Finally, the punch is removed out of the die, back to its original position.

There are different contact regions and different local parameters such as the velocity, strain rate, roughness distribution or contact pressure. Therefore, the whole tribological system cannot be identified with a single parameter like yield strength of the material. Properties of the contacting parts, lubricant and other environmental factors are effective in determining the characteristics of the contact. The tribological system, to be investigated in this study, is taken from the steel cup drawing simulation carried by Darendeliler et al. [4]. The same parameters and environmental conditions are used in friction models and calculations. Deep drawing simulation is performed up to cup depth of 23 mm. Friction models are applied to various cup depths in the following chapter. Then, a square cup drawing process is investigated as a case study in Chapter 5.

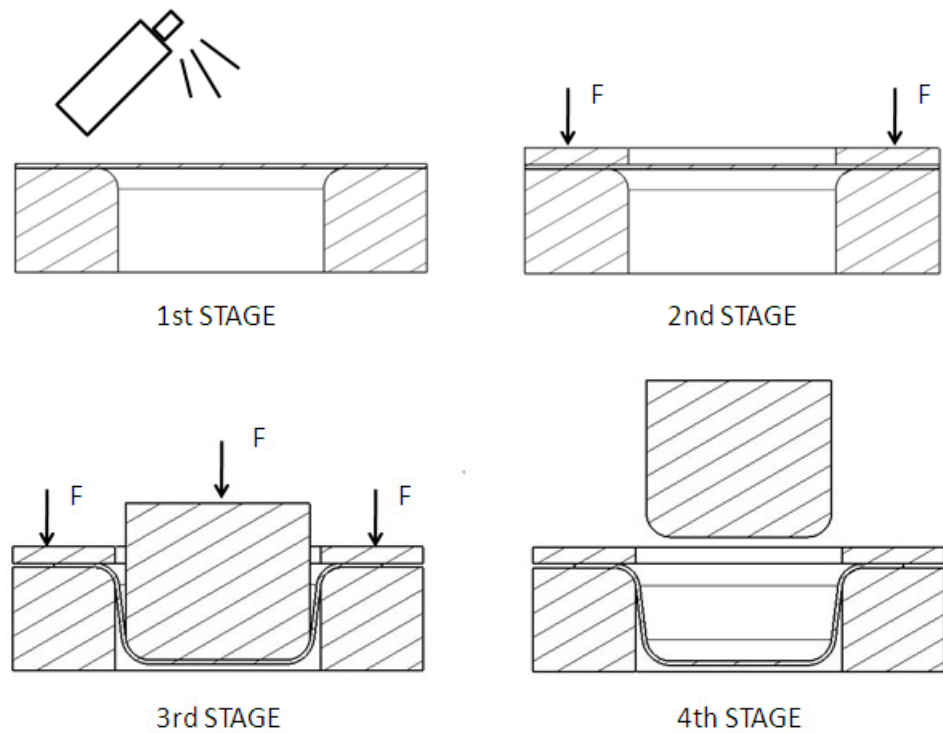


Figure 2.1 Stages of deep drawing process

2.2 Surface Roughness and Rough Surface Contact in Tribology

Brief information will be given about surface roughness parameters and a couple of measurement methods. Additionally, the contact between rough surfaces at different levels and basic principles about rough contacts are explained in the following sections.

2.2.1 Surface Roughness

Surface texture is composed of roughness (microroughness), waviness (macroroughness), lays and flaws. Even the most precise production methods leave a

surface texture at small fractions. Generally lays and flaws are omitted while defining a surface.

The difference between micro and macro roughness comes from the sampling length during measurements. Microroughnesses, such as asperities and valleys, are observed in short wavelengths which are larger than the atomic size. Also, the term of “asperity” is used in 2 dimensions while in 3 dimensions they are called as “summits”. In longer wavelengths waviness is observed, which is classified as macroroughness. There are various reasons for waviness which are originated from the deflections of the tool or workpiece during the process. Vibrations, thermal changes and warping are some of the factors which cause waviness. All the surface defects larger than roughness wavelength and smaller than waviness wavelength are classified in this category.

There are average roughness parameters such as R_a or CLA (center line average) roughness, R_q or RMS (root mean square) roughness, skewness or kurtosis. In order to include asymmetry, distribution concentration (flatness) or deviations from Gaussian distribution, two parameters are defined which are called as skewness (R_{sk}) and kurtosis (R_k). Probability density function, $\phi(s)$, is determined by these parameters. The effects of varying skewness and kurtosis values on probability function are shown in Figure 2.2. As seen from the figure, zero skewness means symmetry of the probability function. Negative skewness means a shift to the left and vice versa. Increasing kurtosis means a shift upwards and vice versa. If kurtosis is larger than 3 then the distribution is called as leptokurtic and if it is smaller than 3 then the distribution is called as platykurtic.

Pearson system is developed by Kotwal and Bhushan [5], which can be used to obtain different frequency curves to define surfaces. In this system, functions are obtained with varying skewness and kurtosis values. Some examples of probability functions are tabulated in Table 2.1. Machining processes leaves surfaces with different properties. Positive skewness is obtained after electrodischarge machining, turning and shaping operations. Negative skewness is obtained after milling, grinding and abrasion processes. High kurtosis is obtained after laser polishing process. For

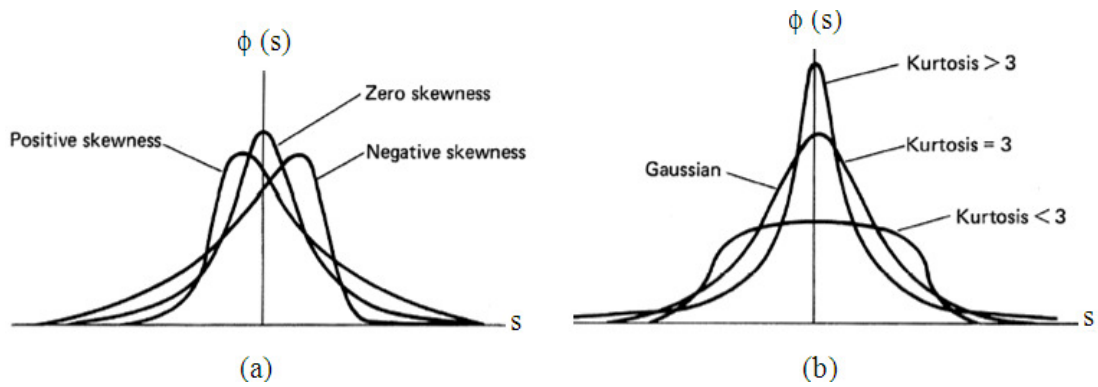


Figure 2.2 (a) Probability density function distribution with varying skewness (b) kurtosis [6]

the Gaussian case, skewness is zero and kurtosis is three. Then, Gaussian distribution is formulated as

$$\phi_s(s) = \frac{1}{\sqrt{2\pi}} e^{-\frac{s^2}{2}} \quad (2.1)$$

Table 2.1 Probability density functions for different skewness and kurtosis values [6]

R_{sk}	R_k	Type	Probability density function
0.0	3	Normal	$\phi(s^*) = 0.3989 \exp(-0.5(s^*)^2)$
0.3	3	I	$\phi(s^*) = 0.39(1+s^*/4.05)^{10.64}(1-s^*/10.72)^{29.80}$
0.5	3	I	$\phi(s^*) = 0.38(1+s^*/2.36)^{2.79}(1-s^*/6.36)^{9.21}$
0.8	3	I	$\phi(s^*) = 0.33(1+s^*/1.36)^{0.11}(1-s^*/3.86)^{2.14}$
0.0	2	II	$\phi(s^*) = 0.32(1-(s^*)^2/16)^{0.5}$
0.0	5	VII	$\phi(s^*) = 0.46(1+(s^*)^2/25)^{-4}$

$$s^* = s/\sigma$$

First of all, a mean line must be defined. The area created by surface peaks and valleys are divided into two by the mean line which is shown in Figure 2.3. In other words, the area created by the surface profile above mean line is equal to the area below mean line. Then, the arithmetic mean of the absolute values of deviations in vertical direction about mean line is called as R_a or CLA (center line average). R_a value of a surface can be expressed as

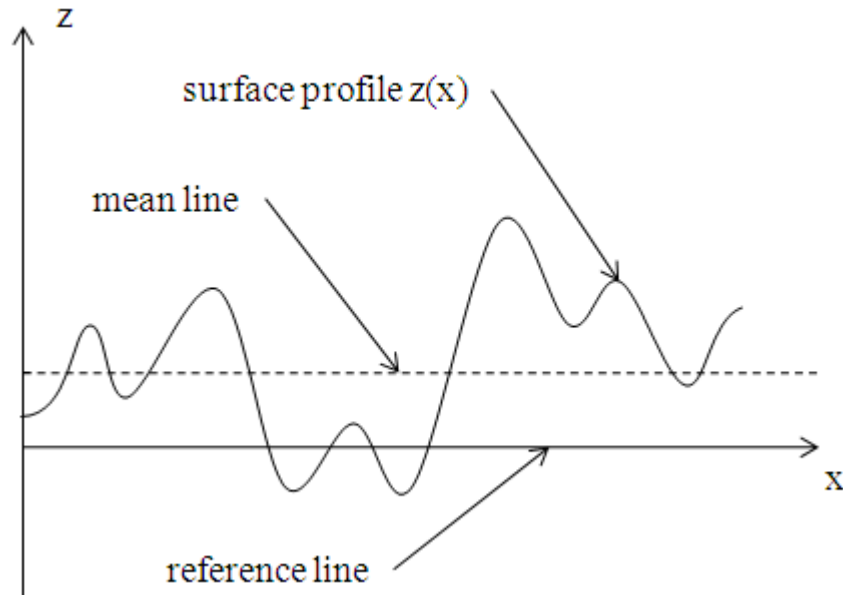


Figure 2.3 Mean line representation

$$R_a = \frac{1}{L} \int_0^L |z - m| dx \quad (2.2)$$

where L is the profile length (or sampling length)

$$m = \frac{1}{L} \int_0^L z dx \quad (2.3)$$

For a Gaussian distribution, σ is approximated as 1.25 times the R_a value [6].

The arithmetic mean of the square of deviations in vertical direction about mean line is called as R_q or RMS (root mean square). R_q value of a surface can be expressed as the following [6]

$$R_q^2 = \frac{1}{L} \int_0^L (z)^2 dx \quad (2.4)$$

2.2.2 Rough Surface Contact

As it was mentioned before, all the surfaces are not completely flat no matter how precise is the machining or forming process. There are asperities or deviations from the surface mean at micro or macro levels. Therefore, when two surfaces interact, contact does not occur at the whole projection area. Only at some fraction of the projection area contact occurs. At first, the highest asperities of two rough surfaces contact, as the contact pressure increases, more and more asperities start to contribute contact. The real contact area consists of very small contacts at asperity tips which are called as micro-contacts. The number of these micro-contacts is determined by the contact pressure, surface roughness and mechanical properties of the blank. At the beginning of the process, contact area depends on the asperity heights. As the load increases, contact area increases proportional to the nominal pressure until saturation is reached. Saturation means that maximum proportion of contact area is achieved. Thus, increasing the contact pressure does not cause an increase in contact area.

Different contact mechanisms are observed in deep drawing process and there are many problems arising from the scaling issues. For instance, roughness scale varies from microscopic waviness to atomic size. It is important to decide which scale level must be considered. In order to have a better understanding, contacts can be divided into two levels which are microscopic contact and asperity contact.

Microscopic Contact: In the microscopic level it is assumed that sheet metal has a higher roughness and lower hardness from the tooling materials. Therefore, the

contact between the sheet metal and tools can be modeled as the contact of a rough, soft surface (blank) and a smooth, hard surface (tool) for simplification. Sometimes, tools can be coated with harder materials which further increase the hardness difference. The driving force in this contact level is the roughness of the blank which varies as the process continues. First, a little decrease in the roughness is observed due to sinking of the asperities into the blank material. Then, as the plastic strain of the surface increases, roughness also increases due to reorientation of the grains towards outside.

Asperity Contact: Asperity contacts can be defined as very small-scale microscopic contacts. In asperity contact, the contact model can be reversed to represent contact mechanism. Then, the contact between the sheet metal and tools can be modeled as the contact of a smooth, soft (blank) surface and a rough, hard surface (tool) for simplification. In contrast to microscopic contact, in asperity contact tool roughness is the driving force.

2.3 Tribology in Deep Drawing

In light-deep drawing conditions, it is not necessary to use lubricant. But, for other cases lubricant usage is inevitable. The conditions of the deep drawing process of interest require lubricant application. Therefore, lubricated deep drawing process is the concern of this thesis.

The classical tribology paid little attention on the sheet metal forming processes. As a result, the number of studies based on deep drawing is low. There are different point of views between the classical view of tribology and deep drawing. They can be summarized as the following;

- In deep drawing, friction is a helpful tool to control material flow while, in classical view it must be minimized.

- The materials of the tool and product are very limited by the process in deep drawing. The final product properties are predetermined (mechanical, surface properties etc.) and the tool materials are tool steel or cast iron. The surface of the tools can be coated by a hard layer.
- In deep drawing process, new material is fed into the deformation zones (punch radius, die radius etc.), in classical tribology surfaces only interact once.

2.3.1 Contact Regions in Deep Drawing

There are different contact regions in deep drawing between the punch, die, blank holder and blank. Parameters such as contact pressure, local velocity, strain rate differs in different regions and results in different local friction values. Schey [7] classified these regions with respect to their friction characteristics, effects on punch force, clamping force and drawability of the blank. The regions are shown in Figure 2.4 and their properties can be summarized as the following;

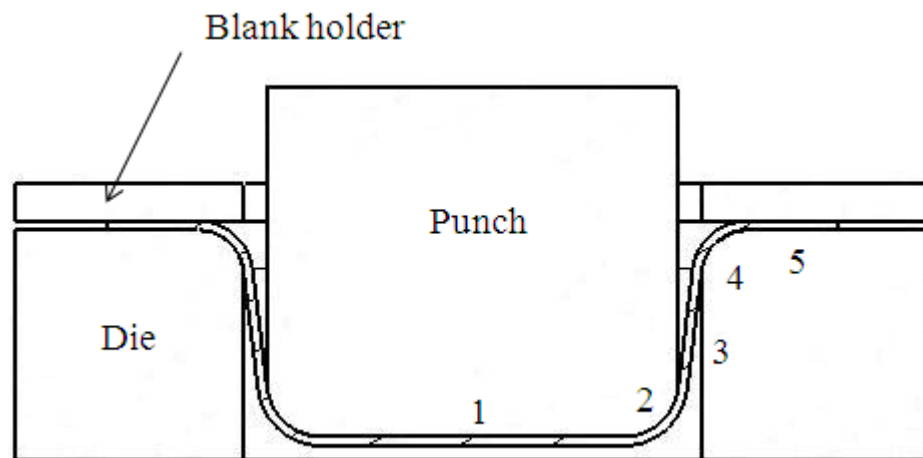


Figure 2.4 Contact regions in deep drawing

Punch and Blank Contact: This contact occurs between the nose (1) and radius (2) regions of the punch and the blank. Most of the deformation occurs at the punch radius contact. Therefore, the coefficient of friction distribution is more effective and important in this region. In literature, no attention is paid and there is no information about the contact and friction at the punch nose. The reason is that, friction in this region is not an important parameter and does not affect the deep drawing process significantly.

Contact pressure at the radius contact varies between 30-60 MPa which increases from the beginning of the punch radius to the end. Sheet metal is subjected to bending and stretching at the radius contact and biaxial stretching at the nose contact. At the radius contact, the friction must be high enough to ensure that the blank follows the motion of the punch. Boundary and mixed lubrication takes place due to concentration of pressure due to decreasing contact area at the radius contact.

Blank Holder & Die and Blank Contact: This contact is divided into two parts which are the die radius (4) and flange (5) contact regions. In the flange region, contact pressure is very low compared to other regions and blank is subjected to radial stress. Reduction in diameter causes circumferential compression. Although contact pressure is low, it must be sufficiently high to prevent wrinkling. Strains are relatively low due to sliding. In the flange region, mixed lubrication is observed due to low pressure about 10 MPa, which is directly proportional to the clamping force.

At the beginning of the process, pressure is evenly distributed over the flange region (5) due to the applied clamping force. As the process continues, contact and pressure distribution in flange region is not uniform due to thickening of the blank at the outer flange, while the clamping force is kept constant. Thickening may cause to the separation of the blank holder from the blank at the inner flange. Then, there are zones of “free deformation” at the inner flange, where surface normal forces are absent. In these zones, there is no contact between the tool and blank. Thickening and free deformation problems can be observed in the exaggerated view of the flange region as shown in Figure 2.5. Additionally, this problem results in very high pressures at the outer flange where the clamping force concentrates.

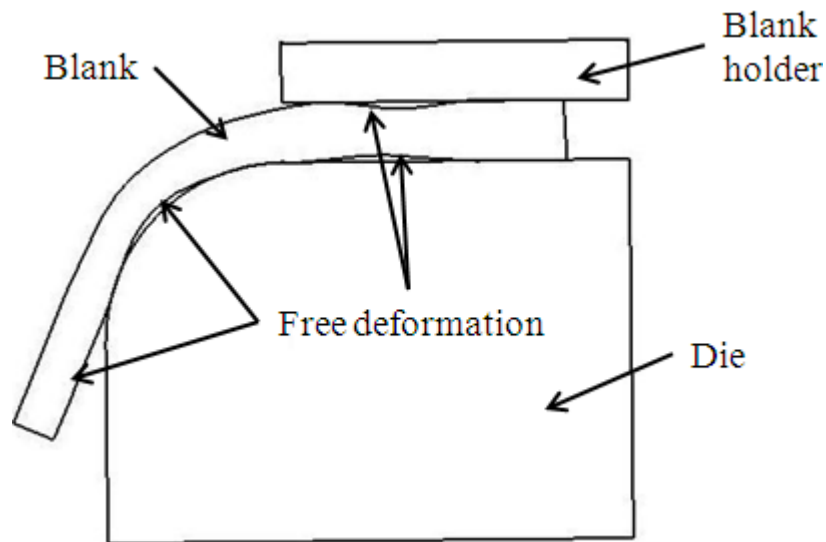


Figure 2.5 Free deformation zones in deep drawing [8]

At the die radius contact (4), there is bending and stretching of the blank. Also, the blank is subjected to radial stresses and tangential compressive stresses which cause wrinkles. In this region, boundary lubrication takes place due to concentration of pressure which is higher than the punch radius contact. Pressure concentrates more in steel blank drawing than aluminum blank drawing which varies between 40-60 MPa. Contact pressure decreases from the beginning of the die radius to the end.

In addition to the contact regions, there is another important region of the blank which has no contact to other parts. It is called as the wall (3) which is free drawn part of the blank. There is thinning of the wall due to tensile forces. The thinnest part can be observed at the place where contact ends between punch and blank. The thinnest section also determines the maximum stress that can be applied to the blank.

It is concluded that, there are different friction parameters and contact characteristics through the whole contact areas. Different deformation modes are observed simultaneously. Therefore, one single theory cannot represent all these contact types. Friction models are introduced to overcome this problem which will be explained in Chapter 3.

2.3.2 General Characteristics of Deep Drawing

Deep drawing processes have a number of internal and environmental characteristics which are similar in most of the applications. Axisymmetric deep drawing process, subject of this study, also shows these characteristics which can be summarized as the following;

- There is a blank, a punch, a die and a blank holder employed in the system.
- Tools are more smooth and softer than the blank; they can be coated with a harder material.
- The blank is rougher and relatively harder also, it deforms plastically during the process.
- The environment conditions are assumed to be at room temperature and atmospheric pressure.
- Always a commercial lubricant is used unless light-duty conditions exist.

CHAPTER 3

MODELING OF FRICTION ON LUBRICATED ROUGH SURFACES

In this chapter, different approaches and formulations of friction parameters are explained for lubricated rough surface contact. Then, two different friction models which will be used in calculations are explained in detail. Finally, a combined friction model is introduced. It is important to note that, dry friction and lubricant starvation conditions are not investigated in this study.

3.1 Literature Survey on Rough Contact

There are many approaches to rough contact modeling in literature which are based on different contact types and different parameters they include. Westenberg [2] classified four different rough contact types based on the stochastic contact, numerical contact, volume conservation and bulk deformation. Most of the methods assume a hard and smooth surface contacting a rough and soft one. Contact can be classified as elastic, plastic or elastic-plastic. Different rough contact model approaches are explained briefly as the following.

It is not possible to represent the whole surface characteristics with one parameter or property. Many parameters have been introduced for this purpose in literature but, it is not clear how many of them are needed or sufficient. Stochastic (statistical) contact modeling is preferred in many studies to overcome this problem.

In the stochastic approach, asperities are represented by simple geometrical shapes such as hemispherical tipped or spherical tipped asperities. For instance, spherical shaped asperities with radius β , asperity density n and surface statistical height distribution $\phi_s(s)$ is shown in Figure 3.1. These values can be obtained by experimental data or using roughness theory introduced by Greenwood [9]. Greenwood-Williamson model is the most common contact model used in literature. This model is used as basis of many friction models which will be discussed later. In the figure, σ_s is the standard deviation of the surface height and d_d is the separation between the mean plane of the summits and surface heights. The Gaussian distribution is assumed for asperity heights in most of the contact models for simplification. But, in real life applications it is not the case.

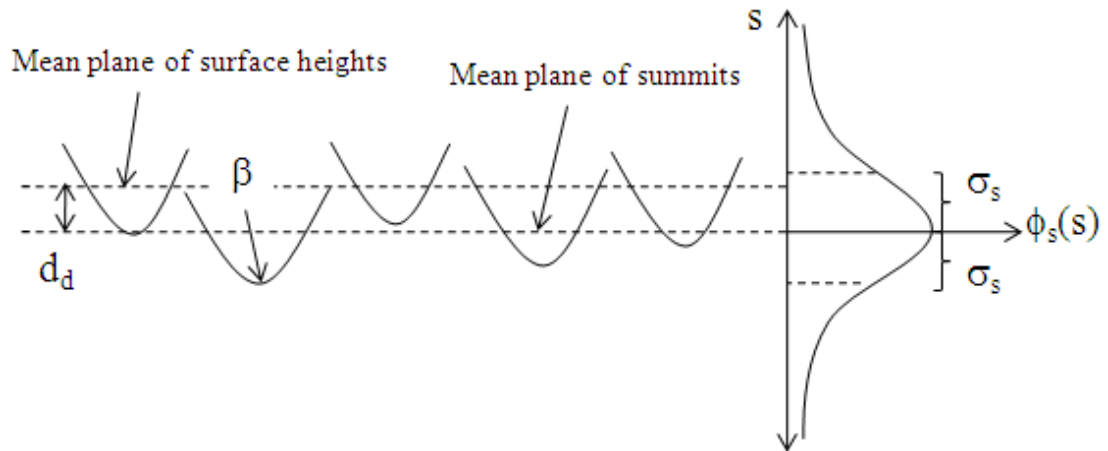


Figure 3.1 Contact between elastic rough, soft surface and rigid smooth surface

Different approaches are used to calculate fractional contact area and nominal pressure by using the statistical distribution given above. Calculated load and real contact area are divided by the nominal area then, nominal pressure (p) and fractional contact area (A) are obtained. Some of the approaches can be explained as the following;

1. In Greenwood-Williamson [9] model it is assumed that the summits are deformed elastically. The tip geometry of the asperities is hemispherical and constant for all asperities. The interactions among asperities are not considered in this model and the following equations are obtained:

$$p = \frac{2}{3} n E' \beta^{1/2} \sigma_s^{3/2} \frac{1}{\sqrt{2\pi}} \int_{d_d}^{\infty} (s - d_d)^{3/2} e^{-\frac{1}{2}s^2} ds \quad (3.1)$$

$$A = \pi n \beta \sigma_s \frac{1}{\sqrt{2\pi}} \int_{d_d}^{\infty} (s - d_d) e^{-\frac{1}{2}s^2} ds \quad (3.2)$$

2. Greenwood-Williamson elastic contact model is modified to be used with paraboloidal shaped asperities [10]. It is assumed that the geometry is constant for all asperities. The interactions among asperities are not considered in this model and the following equations are obtained:

$$p = \left(\frac{16\sqrt{2}}{15} \right) \pi (n \beta \sigma_s)^2 E' \sqrt{\frac{\sigma}{\beta}} \int_{d_d}^{\infty} (s - d_d)^{3/2} \phi'(s) ds \quad (3.3)$$

$$A = \pi^2 (n \beta \sigma_s)^2 \int_{d_d}^{\infty} (s - d_d)^2 \phi'(s) ds \quad (3.4)$$

3. Onions and Archard [11] improved the Greenwood-Williamson elastic contact model by introducing an exponential correlation function β' . The interactions among asperities are not considered in this model and the following equations are obtained:

$$p = \frac{4E' \sigma_s}{15(2.3\beta')} \int_{d_d}^{\infty} \int_{d_d}^{\infty} \frac{f'(s, C)}{N} dC ds \quad (3.5)$$

$$A = \frac{1}{5} \pi F_A(d_d) \quad (3.6)$$

where $f'(s, C)$ is the probability density, N is the ratio of peaks to ordinates and C is the non-dimensional asperity curvature.

4. Chang et al. [12] introduced an elastic-plastic asperity model. This model is based on the control volume conservation during plastic deformation. The following equations are obtained:

$$p = 0.6\pi n\beta H \frac{1}{\sqrt{2\pi}} \int_{d_d+\omega_c}^{\infty} (2(s-d_d) - \omega_c) e^{-\frac{1}{2}s^2} ds \quad (3.7)$$

$$A = \pi n\beta \frac{1}{\sqrt{2\pi}} \int_{d_d+\omega_c}^{\infty} (2(s-d_d) - \omega_c) e^{-\frac{1}{2}s^2} ds \quad (3.8)$$

where

$$\omega_c = \left(\frac{0.6\pi H}{2E'}\right)^2 \beta \quad (3.9)$$

5. Halling et al. [13] developed a model including both elastically and plastically (ideally) deformation of the asperity summits. The following equation sets are obtained.

Elastic deformation formulations are the following:

$$p = \frac{2}{3} nE' \beta^{1/2} \frac{1}{\sqrt{2\pi}} \int_{d_d}^{d_d+1/\psi^2} (s-d_d)^{\frac{3}{2}} e^{-\frac{1}{2}s^2} ds \quad (3.10)$$

$$A = \pi n\beta \frac{1}{\sqrt{2\pi}} \int_{d_d}^{d_d+1/\psi^2} (s-d_d) e^{-\frac{1}{2}s^2} ds \quad (3.11)$$

Plastic deformation formulations are the following:

$$p = 2\pi H n\beta \frac{1}{\sqrt{2\pi}} \int_{d_d+1/\psi^2}^{\infty} (s-d_d) e^{-\frac{1}{2}s^2} ds \quad (3.12)$$

$$A = 2\pi n\beta \frac{1}{\sqrt{2\pi}} \int_{d_d+1/\psi^2}^{\infty} (s-d_d) e^{-\frac{1}{2}s^2} ds \quad (3.13)$$

where ψ is the plasticity index.

The only unknown is d_d in the above equations. By substituting its value, pressure and fractional contact area can be calculated. The value of d_d is generally approximated by the standard deviation of summits ($\sim 1.15\sigma_s$).

All the rough contact models which are based on numerical contact approach treat asperities as bars. It is assumed that the contact occurs between a hard and a soft surface. All the formulations are based on elastic deformation of asperities while plastic deformation is not included. Some of the models using this approach were developed by Liu et al. [14] and Webster & Sayles [15].

Pullen & Williamson [16] developed a model based on volume conservation. It is assumed that the volume of the indented asperities is equal to the rising valleys. This model does not include work hardening and bulk deformation. One of the main advantages of this model is that, it can be applied to any arbitrary shaped asperity. Then, the following equations are obtained:

$$U = \int_{d-U}^{\infty} (s - d + U) e^{-\frac{1}{2}s^2} ds \quad (3.14)$$

$$A = \int_{d-U}^{\infty} e^{-\frac{1}{2}s^2} ds \quad (3.15)$$

where U is the rise of asperity valleys.

The bulk deformation has an important effect on flattening or roughing of a surface. So far, models have been developed which are concentrated on flattening while less attention is paid on roughening. Mostly, wedge-shaped asperities are assumed as shown in Figure 3.2. There are two different approaches, where workpiece asperities are smoothing or smooth workpiece is roughening by the tooling. Bulk deformation is an important factor in deep drawing and should be taken into account. Some of the models including bulk deformation were developed by Sutcliffe [17], Wilson & Sheu [18] and Kimura & Childs [19].

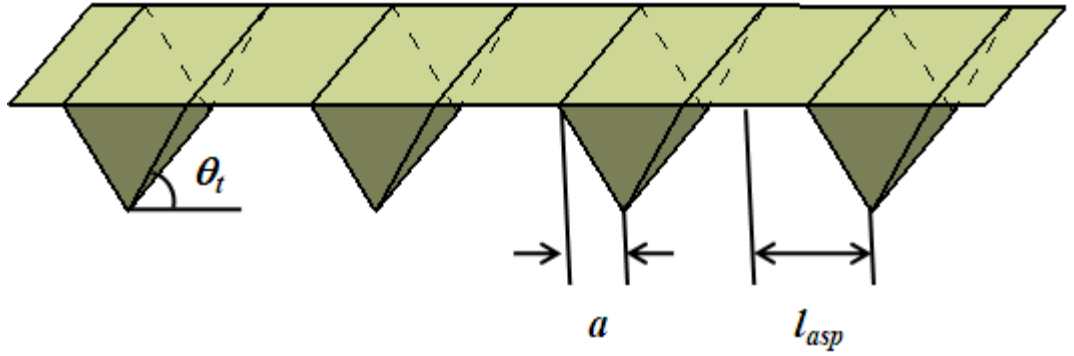


Figure 3.2 Wedge-shaped, infinitely long asperities

1. Sutcliffe [17] developed a bulk deformation model in which wedge-shaped asperities are investigated. Strains are assumed to be in perpendicular direction to the orientation of asperities and there is no strain in parallel direction. As a result, slipline analysis may be performed for an ideal plastic model. Sutcliffe introduced a non-dimensional parameter Φ , fan angle, which is given by:

$$\Phi = \frac{H_{eff}}{4} (1 - A) \quad (3.16)$$

where H_{eff} is the non-dimensional effective hardness. Another parameter W is obtained by applying slipline theory as the following:

$$W = \frac{(U_1 - U_2)}{\dot{\epsilon}l} \quad (3.17)$$

An expression is developed by fitting the results of a slipline analysis:

$$W = -0.184 + 1.21e^{1.47\Phi} \quad (3.18)$$

by substituting Equation (3.16) into (3.18) and rearranging $\bar{E} = 1/W$ gives:

$$H_{eff} = \frac{2.72}{1 - A} \ln\left(\frac{0.829}{\bar{E}} + 0.152\right) \quad (3.19)$$

2. Wilson and Sheu [18] used an upper-bound method to show that the presence of bulk plastic strain reduces the non-dimensional effective hardness (H_{eff}) of the workpiece surface which makes easy to flatten workpiece asperities. They investigated parallel, infinitely long and wedge-shaped asperities. The surface slope of asperities is assumed to be constant. Unlike Sutcliffe model, strains are assumed to be parallel to the orientation of the asperities and there is no strain in perpendicular direction. They developed a relation for the fractional contact area:

$$A = \frac{a}{l_{asp}} \quad (3.20)$$

where a is the half width of an asperity and l_{asp} is the half distance between asperities. Then, the following semi-empirical equations are developed for effective hardness

$$f_1(A) = -0.86A^2 + 0.345A + 0.515 \quad (3.21)$$

$$f_2(A) = \frac{1}{2.571 - A - A \ln(1 - A)} \quad (3.22)$$

$$\bar{E} = \frac{\dot{\epsilon} l_{asp}}{\theta_t (U_1 - U_2)} \quad (3.23)$$

$$H_{eff} = \frac{2}{f_1(A)\bar{E} + f_2(A)} \quad (3.24)$$

where $\dot{\epsilon}$ is the uniform elongation strain rate, θ_t is the tooling asperity slope and \bar{E} is the non-dimensional strain rate.

3.2 Hertzian Contact Theory

In contact mechanics, Hertzian contact has great importance and most of the friction models are based on its theory. Therefore, Hertzian theory must be understood well before the derivation of the friction models. Although it is applicable to any geometry, mostly simple geometries are considered such as sphere-sphere contact, cylinder-cylinder contact and sphere-flat contact.

In Hertzian theory, two elastic bodies are pressed against each other and deformed slightly under a normal load. Then, the shape of the contact, magnitude and distribution of pressure are calculated. Contact area is a rectangle with a width of “ $2a$ ” in a line contact and it is a circle with radius “ a ” in point contact. In friction modeling, point contact (sphere-sphere) and line contact (cylinder-cylinder) are the most popular contact types. Schematic representations of these contacts are shown in Figure 3.3.

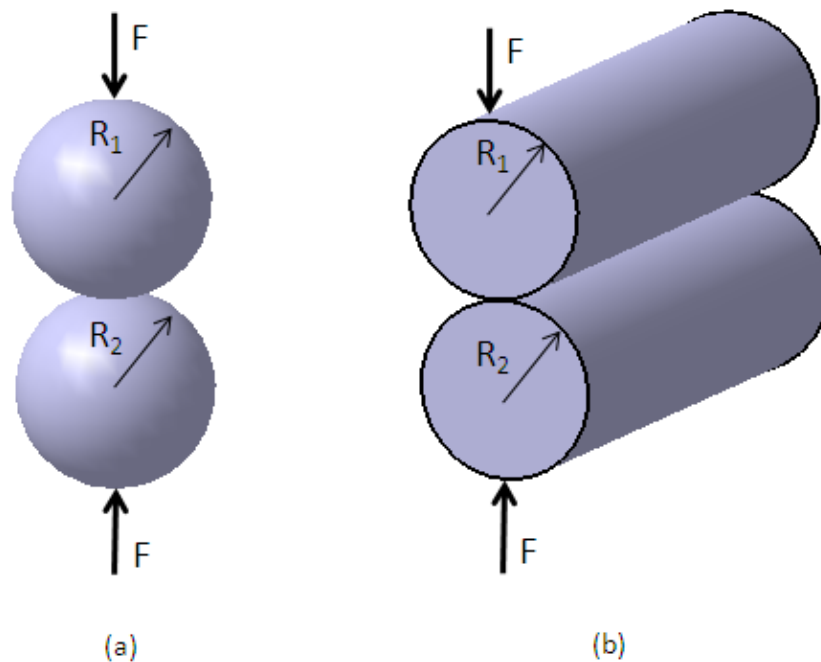


Figure 3.3 Hertzian contact types (a) point contact (b) line contact

The equivalent radius (R) is used in the calculations of film thickness. It is the equivalent geometry of two surfaces contacting each other with local radius of curvatures R_1 and R_2 . Equivalent system is composed of a body with the radius of curvature R contacting a flat body as shown in Figure 3.4. Then, R is calculated from [20]

$$R = \frac{R_1 \times R_2}{R_1 + R_2} \quad (3.25)$$

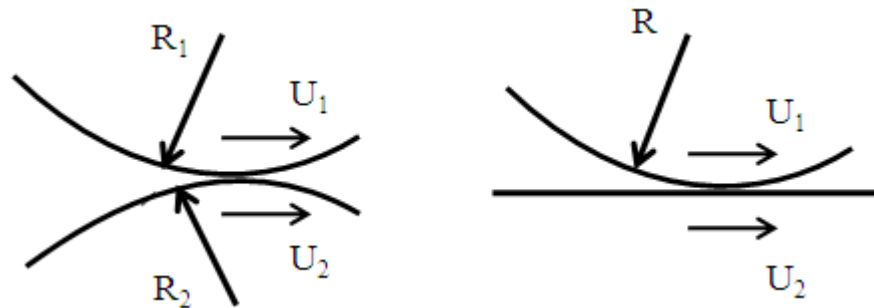


Figure 3.4 Equivalent radius representations

In the results of simulation, position of nodes is available and equivalent radius is calculated by using the coordinates of these nodes. For simplicity, calculations are performed for nodes on the same plane which lies on x and z axes. Then, the problem is in 2-D instead of 3-D, which is much easier to handle. In order to calculate the radius of curvature of a node, 2 neighbor nodes are used and it is concluded from the results that using 3 nodes provides accurate results. The calculation steps for equivalent radius are shown in Appendix A.

The maximum contact half width and the contact pressure values can be calculated for point and line contacts from the formulas in Table 3.1.

Table 3.1 Hertzian contact formulas for point and line contacts [20]

	Point Contact	Line Contact
Half Contact Width	$a = \sqrt[3]{\frac{3FR}{4E'}}$	$a = \sqrt{\frac{4FR}{\pi E'}}$
Maximum Pressure	$p_H = \frac{1}{\pi} \left(\frac{6F(E')^2}{R^2} \right)^{1/3}$	$p_H = \left(\frac{E'F}{\pi R} \right)^{1/2}$

* For line contact F is force per unit length.

Effective elastic modulus (E') is calculated from the elastic modulus and poisson ratio of the contacting bodies. Then Effective elastic modulus is calculated from [20]

$$\frac{1}{E'} = \frac{1}{2} \left(\frac{1 - \nu_1^2}{E_1} + \frac{1 - \nu_2^2}{E_2} \right) \quad (3.26)$$

3.3 Rough Surface Friction Models

Previous studies, which are based on the stochastic theory, are limited to one dimensional roughness structures either oriented transversely or longitudinally. Patir and Cheng [21,22] introduced the average flow model which determines the effects of surface roughness on partially lubricated and sliding contacts by using flow factors. Tripp [23] extended the studies of Patir and Cheng, by utilizing a perturbation expansion of the pressure in a nominal parallel film to calculate the values of the flow factors. Hess and Soom [24] investigated the friction-velocity characteristics of line contact in different lubrication regimes and had shown that with an increasing frequency of oscillation, a multi-valued coefficient of friction appeared. Polycarpou and Soom [25] developed two-dimensional models of boundary and mixed friction at a line contact to formulate the coefficient of friction

by explicitly considering the effects of the normal motions, load, lubricant properties and varying sliding velocities. Wilson and Sheu [18] developed models related to the tool-workpiece friction in metal forming processes operating in the boundary lubrication regime. These models include the influence of surface asperity flattening on workpiece, effective hardness of the surface, real area of the contact, interface pressure, sliding speed, and workpiece strain rate on friction.

In order to include asperity interaction at line contacts, Greenwood and Williamson [9] developed a statistical representation of surface roughness. Gelinck and Schipper [27] used deformation equation at a line contact to relate the asperity pressure with the maximum Hertzian pressure for load transmitted between asperities. Lu et al. [28] verified this method by experiment which is followed by the study of Akbarzadeh and Khonsari [29]. Zhai et al. [30] used a mixed film friction approach to include the unsteady behavior of friction.

In this study, among the friction models mentioned above, Wilson's friction model and Khonsari's friction model are chosen which are based on stochastic contact. Wilson's friction model considers bulk deformation and Khonsari's friction model is a modified version of Gelinck [27] which includes squeeze force of the lubricant.

3.3.1 Wilson's Friction Model

Wilson developed a realistic friction model which takes account of the different lubrication regimes that may occur at the tooling/workpiece interface. Wilson used the average Reynolds equation developed by Patir and Cheng which is a useful approach for treating the surface roughness on lubrication. In this model lubrication regime is divided into four main parts which are determined by the ratio of the mean lubricant film thickness (h) with respect to the combined surface roughness (σ) [1].

Film Thickness: Film thickness is calculated for a line contact by Equation (3.27). Line contact approach is more suitable than point contact approach because of the tangential symmetry in deep drawing process. It is reported by Dawson and

Higginson [31] that this formula gives accurate results for a wide range of lubrication regimes.

$$h = \frac{1.6\alpha^{1.6}(\mu_0 V)^{0.7}(E')^{0.03}R^{0.43}}{w^{0.13}} \quad (3.27)$$

where w is the force per unit length

$$w = \frac{32Rp^2}{\pi E'} \quad (3.28)$$

and $V = (V_1 + V_2)/2$ is the average local velocity of the contacting bodies. Calculation of V in cartesian coordinates are given in Appendix B.

Equivalent radius of curvature (R) and effective elastic modulus (E') values in the film thickness formulation are calculated from Equations (3.25)-(3.26).

Thick Film Regime: If $h > 10\sigma$, the system is in the thick film regime and the friction stress is contributed only from the hydrodynamic component and it is a function of hydrodynamic friction τ_h . Then, the friction stress is calculated from [1]

$$\tau_f = \tau_h = \frac{\mu V_r}{h} \quad (3.29)$$

where V_r is the local relative velocity of the contacting bodies. Calculation of V_r in cartesian coordinates are given in Appendix B.

Thin Film Regime: If $10\sigma \geq h > 3\sigma$, the system is in the thin film regime. Although the friction is still due purely viscous shear, the hydrodynamic friction formula must be modified in order to take account of roughness. Then, the shear stress factor is integrated into Equation (3.29) which gives [1]

$$\tau_h = \phi_f \frac{\mu V_r}{h} \quad (3.30)$$

In Wilson's friction model, the shear stress factor formula is taken from Patir and Cheng [22] for $h > 3\sigma$:

$$\phi_f = \frac{35}{32} z \left\{ (1 - z^2)^3 \ln \left(\frac{z+1}{z-1} \right) + \frac{z}{15} [66 + z^2(30z^2 - 80)] \right\} \quad (3.31)$$

where z is the non-dimensional film thickness defined by

$$z = \frac{h}{3\sigma} \quad (3.32)$$

Mixed & Boundary Lubrication Regime: If $h \leq 3\sigma$, then the system is either in the mixed or boundary lubrication regime. In order to determine the correct regime, the system is assumed to be in the mixed regime and the mean lubricant pressure, p_b , in the roughness valleys are estimated. If the pressure is positive then, the system is in the mixed lubrication regime. If it is negative then, the system is in the boundary lubrication regime. In the mixed regime, the mean pressure in the lubricant valleys is obtained from [1]

$$p_b = p - AH_{eff}k \quad (3.33)$$

Sheet shear strength (k), is the strength of the material against shear. It is approximated by the tensile yield strength (TYS) or ultimate tensile strength (UTS) of the material. Approximate estimation of these values yield

$$k \cong 0.75 \times UTS \cong 0.58 \times YYS \quad (3.34)$$

It is noted before that the real contact and nominal contact areas are not the same. Contact occurs only at some fraction of the nominal area. Christensen [32] developed a formula based on the ratio of film thickness to the combined surface roughness. Then, the fractional contact area is calculated from

$$A = \frac{35}{32} \left[\frac{16}{35} - z + z^3 - \frac{3}{5}z^5 + \frac{1}{7}z^7 \right] \quad (3.35)$$

Workpiece effective hardness is calculated from Equations (3.21)-(3.24) developed by Wilson & Sheu [18] for a system similar to deep drawing. Then, the mean lubricant pressure can be found and the regime can be determined. If mean pressure

is positive then, it can be concluded that mixed lubrication takes place while negative sign means boundary lubrication. In the mixed lubrication regime, the frictional stress τ_f can be expressed as

$$\tau_f = \tau_a A + \tau_p A + \tau_h(1 - A) \quad (3.36)$$

The adhesion and plowing components of friction are given by:

$$\tau_a = ck \quad (3.37)$$

$$\tau_p = \theta_t k H_{eff} \quad (3.38)$$

The adhesion and plowing friction expressions are very rough estimates of the asperity contact by taking the adhesion coefficient (c) and mean slope of the tooling asperities (θ_t) as constants. They do not include the effects of variables like contact pressure, film thickness or viscosity etc. Therefore, the accuracy of the results is reduced.

The hydrodynamic component is given by the same formula used in thin film regime. But, the shear stress factor is given by Patir and Cheng [22] for $h < 3\sigma$:

$$\phi_f = \frac{35}{32} z \left\{ (1 - z^2)^3 \ln(300(z + 1)) + \frac{1}{60} \left[-55 + z(132 + z(345 + z(-160 + z(-40 + z(60 + 147z)))) \right] \right\} \quad (3.39)$$

The shear factor expression for $h < 3\sigma$ is a very rough estimation as it was noted by Patir and Cheng [22]. Because, in the calculations of the shear factor, the integral grows unboundedly and infinite shear stresses are obtained at the contact points where film thicknesses are zero. In order to avoid this problem, a small film thickness is chosen, below which the hydrodynamic shear stress is assumed not to exist. In the boundary lubrication regime, the frictional stress is only contributed from adhesion and plowing components of friction. Then, Equation (3.36) yield

$$\tau_f = \tau_a A + \tau_p A \quad (3.40)$$

Coefficient of friction is found from Equation (3.41) at each node. Finally, the flow chart of the Wilson's friction model is shown in Figure 3.5.

$$f = \frac{\tau_f}{p} \quad (3.41)$$

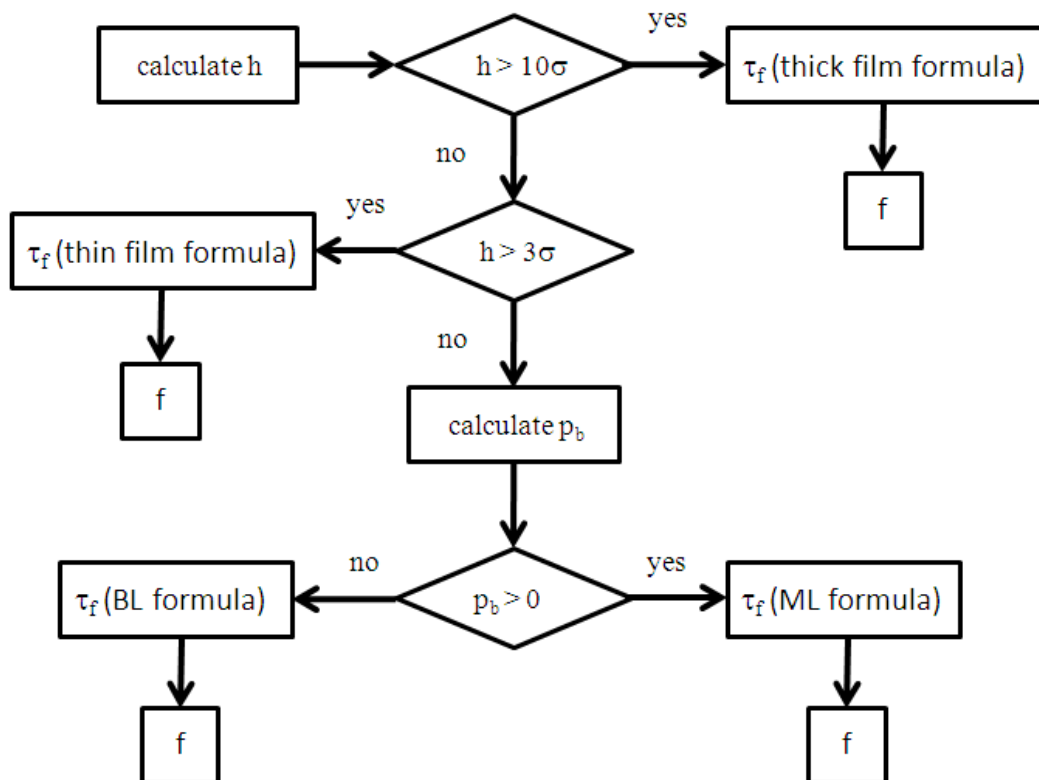


Figure 3.5 Flow chart of Wilson's friction model [1]

3.3.2 Khonsari's Friction Model

Khonsari [33] developed a realistic dynamic friction model for the lubricated sliding contact by decoupling the steady and unsteady terms in Reynolds equation. Friction model uses the load-sharing approach in steady term calculations. In this model, the problem of solving the HL contact is replaced by the problem of solving the dry line contact with deformation, the problem of solving lubricated line contact with deformation (without surface roughness) and the problem of squeeze action of the fluid film. This model also captures the characteristics of the dynamic friction.

In this model, the total applied load is a combination of the asperity contact, hydrodynamic and squeeze forces which is given by:

$$F_T = F_H + F_C + F_{sq} \quad (3.42)$$

The complete Reynolds equation for the time variable fluid film pressure, p_f , is given by:

$$\frac{\partial}{\partial x} \left(\frac{\rho h^3}{12\mu} \frac{\partial p_f}{\partial x} \right) = \frac{\partial \rho h}{\partial t} + u_s \frac{\partial (\rho h)}{\partial x} \quad (3.43)$$

In Hertzian line contact, the interacting surfaces undergo deformation within a rectangular contact area of the width $2a$. “ a ” is the half width of Hertzian contact. In an elastohydrodynamic line contact, the central film thickness is nearly uniform, its width and pressure are similar to Hertzian dry contact. Then, the deformation equation can be written as

$$h(x) = h_0 + \frac{x^2}{2R'} - \frac{4}{\pi E'} \int_{-\infty}^{+\infty} p_T(s) \ln(|x - s|^2) ds \quad (3.44)$$

where p_T is the sum of asperity and fluid pressure. Then, the change in the viscosity is given by Barus [26]:

$$\mu = \mu_0 e^{\alpha p_f} \quad (3.45)$$

where μ_0 is the dynamic viscosity at room temperature and zero pressure and α is the pressure viscosity index.

The Squeeze Term: Under light-load conditions, the surface deformation can be neglected and the squeeze force can be derived from the Reynolds equation. The squeeze term is more effective at higher contact velocities such as bearings and can be neglected for relatively smaller processes as reported by Khonsari. In the Reynolds equation, the fluid film pressure is replaced by squeeze pressure. It is assumed that the film thickness over the contact area is uniform and it is equal to the central film thickness h_c . After derivations the resulting squeeze force equation becomes [33]:

$$F_{sq} = \frac{4al}{\alpha} - \frac{l}{\alpha} \sqrt{\frac{1 + Ba^2}{B}} \ln\left(\left(\frac{\sqrt{B}a + \sqrt{1 + Ba^2}}{\sqrt{1 + Ba^2} - \sqrt{B}a}\right)^2\right) \quad (3.46)$$

where

$$B = 6 \frac{\mu_0}{h_c^3} \alpha \frac{\partial h_c}{\partial t} \quad (3.47)$$

In order to find the steady load, the damping load must be subtracted from the total load which is given by:

$$F_S = F_T - F_{sq} \quad (3.48)$$

where

$$F_S = F_C + F_H \quad (3.49)$$

Then, the steady load can be expressed for asperity contact and hydrodynamic terms by using scaling factors γ_1 and γ_2 :

$$F_S = \frac{F_S}{\gamma_1} + \frac{F_S}{\gamma_2} \quad (3.50)$$

Elastohydrodynamic Term: In the calculation of the elastohydrodynamic term, the unsteady term of the Reynolds Equation (3.43) can be dropped and the following equation is obtained:

$$\frac{\partial}{\partial x} \left(\frac{\rho h^3}{12\mu} \frac{\partial p_h}{\partial x} \right) = u_s \frac{\partial(\rho h)}{\partial x} \quad (3.51)$$

The deformation equation for the hydrodynamic term is the following:

$$h(x) = h_0 + \frac{x^2}{2R} - \frac{4\gamma_2}{\pi E'} \int_{-\infty}^{+\infty} p_h(s) \ln(|x - s|^2) ds \quad (3.52)$$

where p_h is the hydrodynamic pressure. Then, the steady load can be expressed as the following:

$$F_S = \gamma_2 l \int_{-\infty}^{+\infty} p_h(s) ds \quad (3.53)$$

As it was mentioned before, these formulations are for smooth surfaces which are also solved by Moes. Rearranging the Equations (3.51)-(3.53) and substituting into the central film thickness relation gives the following:

$$\begin{aligned} \bar{h}_c \bar{U}^{-0.5} = & \left[(\gamma_2)^{\frac{s}{2}} (H_{RI}^{\frac{7}{3}} + (\gamma_2)^{-\frac{14}{15}} H_{EI}^{\frac{7}{3}})^{\left(\frac{3}{7}\right)s} \right. \\ & \left. + (\gamma_2)^{-\frac{s}{2}} (H_{RP}^{-7/2} + H_{EP}^{-7/2})^{-(2/7)s} \right]^{s-1} (\gamma_2)^{1/2} \end{aligned} \quad (3.54)$$

where

$$s = \frac{1}{5} \left(7 + 8e^{\left[-2\gamma_2^{-\frac{2}{5}} (H_{EI}/H_{RI}) \right]} \right) \quad (3.55)$$

with the following non-dimensional parameters:

$$\begin{aligned}
H_{EI} &= 2.621M^{-1/5}, & H_{RI} &= 3M^{-1} \\
H_{EP} &= 1.311M^{-1/8}L^{3/4}, & H_{RP} &= 1.287L^{2/3} \\
\bar{h}_c &= h_c/R, & \bar{U} &= \frac{\mu_0 u_s}{E'R} \\
M &= W\bar{U}^{-1/2}, & L &= G\bar{U}^{1/4} \\
G &= \alpha E', & W &= \frac{F_s}{E'Rl}
\end{aligned} \tag{3.56}$$

Asperity Contact Term: The asperity contact of two rough surfaces is replaced by the contact between an equivalent rough surface with a flat surface. Then, the asperity contact pressure for spherical asperities is given by [33]:

$$p_a(x) = \frac{2}{3} n\beta\sigma_s \sqrt{\frac{\sigma_s}{\beta}} E' F_{3/2}\left(\frac{h(x)}{\sigma_s}\right) \tag{3.57}$$

where

$$F_{3/2}\left(\frac{h(x)}{\sigma_s}\right) = \frac{1}{\sqrt{2\pi}} \int_{h(x)/\sigma_s}^{\infty} \left(s - \frac{h(x)}{\sigma_s}\right)^{3/2} e^{-\frac{1}{2}s^2} ds \tag{3.58}$$

The deformation equation for the asperity contact term is the following:

$$h(x) = h_0 + \frac{x^2}{2R} - \frac{4\gamma_1}{\pi E'} \int_{-\infty}^{+\infty} p_a(s) \ln(|x - s|^2) ds \tag{3.59}$$

Then, the steady load can be expressed as the following;

$$F_s = \gamma_1 l \int_{-\infty}^{+\infty} p_a(s) ds \tag{3.60}$$

A relation to calculate the central asperity contact pressure, p_c , with the maximum Hertzian pressure at a line contact is derived by Gelinck and Schipper [27] as the following:

$$p_c = p_H [1 + (a_1 \bar{n}^{a_2} \bar{\sigma}_s^{a_3} W^{a_2 - a_3})^{a_4}]^{1/a_4} \quad (3.61)$$

where $a_1 = 1.558$, $a_2 = 0.0337$, $a_3 = -0.422$, $a_4 = -1.70$ and p_H represents the maximum Hertzian pressure which is given by:

$$p_H = \sqrt{\frac{F_S E'}{2\pi l R}} \quad (3.62)$$

Rearranging the terms and substituting into the central asperity contact pressure gives the following equation:

$$\frac{2}{3} \pi \bar{\sigma}_s^{3/2} \bar{F}_S F_{3/2} \left(\frac{\bar{h}_c - \bar{d}_d}{\bar{\sigma}_s} \right) = [1 + (a_1 \bar{n}^{a_2} \bar{\sigma}_s^{a_3} W^{a_2 - a_3} \gamma_2^{a_2})^{a_4}]^{1/a_4} \frac{1}{\gamma_1} \quad (3.63)$$

with the following non-dimensional parameters:

$$\begin{aligned} \bar{n} &= nR\sqrt{R\beta}, & \bar{h}_c &= \frac{h_c}{R} \\ \bar{d}_d &= \frac{d_d}{R}, & \bar{F}_S &= \sqrt{\frac{2\pi l R E'}{F_S}} \\ \bar{\sigma}_s &= \frac{\sigma_s}{R} \end{aligned} \quad (3.64)$$

Friction Coefficient: The total friction is the sum of asperity contact friction and fluid traction effect which is given by;

$$f = \frac{F_{f,H} + F_{f,C}}{F_T} \quad (3.65)$$

Similar to Coulomb's law, the asperity contact friction is the product of an average asperity friction coefficient f_c and the load carried by the asperities F_C which yield

$$F_{f,C} = f_c F_C \quad (3.66)$$

Assuming the separation of two rough surfaces to be constant and equal to the central film thickness h_c , the hydrodynamic friction force is calculated from [33]

$$F_{f,H} = \tau_L(1 - e^{-\mu(u_s/h_c)/\tau_L}) \times 2al \quad (3.67)$$

where τ_L is the limiting shear stress varying with pressure

$$\tau_L = \tau_{L0} + \beta_0 p_m \quad (3.68)$$

First of all, a film thickness is assumed and the squeeze force is calculated by Equations (3.46) and (3.47). Then, the steady load is found from Equation (3.49). Afterwards, an iterative solving step starts. γ_1 and h values are used to calculate γ_2 by using Equations (3.54) and (3.63). The validity of Equation (3.50) is checked until convergence is achieved. The flow chart of the Khonsari's friction model is shown in Figure 3.6.

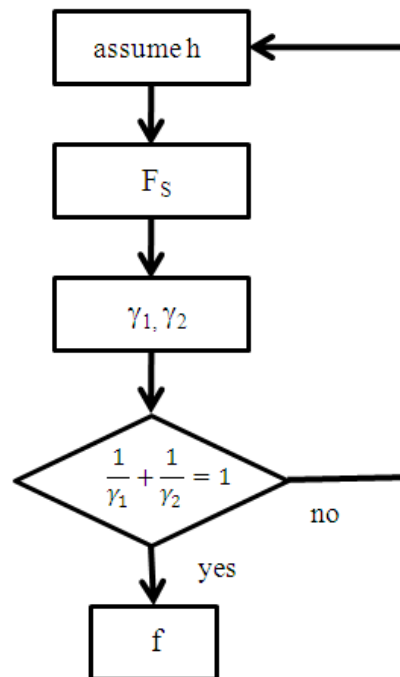


Figure 3.6 Flow chart of Khonsari's friction model [33]

CHAPTER 4

SIMULATION OF LUBRICATED ROUGH SURFACE FRICTION MODELS

In this chapter, first of all, in order to check the validity of the FEM model, the strain distributions obtained at different cup depths are compared with the data given in the literature. Then, in order to check the validity of the developed program codes for friction models, they are applied to the cases given in the literature. Wilson's and Khonsari's friction models are separately applied to axisymmetric deep drawing process. After comparing the results, characteristics of both models are discussed.

4.1 Deep Drawing Components

In this section, deep drawing parameters and components are explained for cylindrical cup drawing.

The Tool: Deep drawing process includes a punch, a die and a blank holder. The tools are made of steel and they are assumed to be rigid. The punch has a diameter of 45 mm and profile radius of 6mm at the tip. The forming die has an outer diameter of 100 mm and inner diameter of 48 mm. The die has a radius of 5 mm. The blank holder has an outer diameter of 100 mm and an inner diameter of 29 mm. Tool geometries and dimensions are in millimeters, which are shown in Figure 4.1 [4].

The hardness of the coating, applied on the tool, affects the Stribeck curve. As the hardness increases, the curve shifts to the right and vice versa. If the tool materials are softer compared to the blank, harder asperities on the blank penetrate into the

softer tooling material while in contact. In order to avoid penetration and micro-deformations on the tool surface, surface coating with a harder material is necessary. Surface roughness is an important parameter that affects the friction coefficient and directly related to the surface coating method and chemical composition of the coating layers.

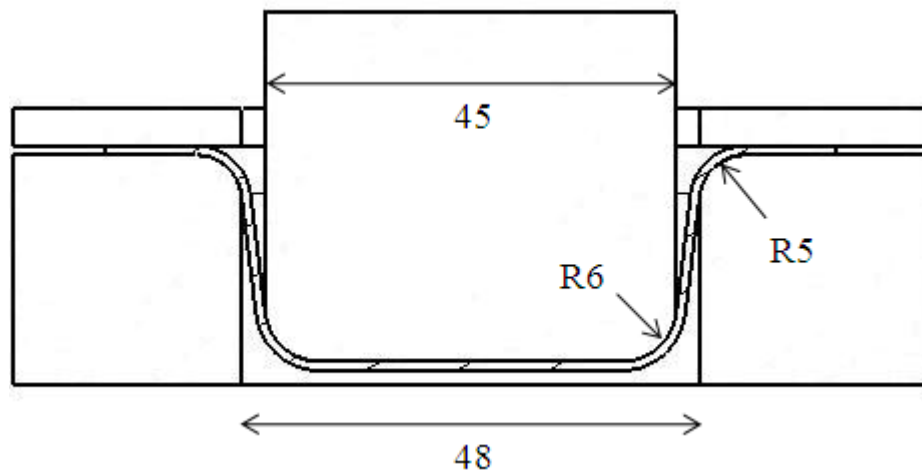


Figure 4.1 Tool geometry of cylindrical cup drawing

The Blank: The blank material, which is used in experiments, is a deep drawing quality steel sheet metal with a thickness of 0.66 mm and 100 mm in diameter. It has an elastic modulus of 210 GPa and yield strength of 256 MPa. Its behavior in plastic deformation zone is given by $\bar{\sigma} = 547\epsilon^{0.19}$ relation, which is obtained through simple tension test [4]. Surface roughness of the blank is defined for Wilson's and Khonsari's friction models separately. Roughness of the blank is determined by the manufacturing method of the rolls used in blank manufacturing.

Lubricant: The lubricant, which is used in the process, can operate at a wide temperature range. The dynamic viscosity at atmospheric pressure is taken as 0.025 Pa.s and pressure viscosity index is $2 \times 10^{-8} \text{ Pa}^{-1}$ for the lubricant.

4.2 FEM Model of Cylindrical Cup Drawing

The blank, punch, blank holder and die are modeled as surfaces by using a commercial CAD program. The FEM model is shown in Figure 4.2. Only a wedge-shaped sector of the blank is considered for decreasing simulation time since there is tangential symmetry. After a couple of runs it is observed that 10° of sector gives fairly good results. Then, they are imported to the preprocessor of FEM program. The maximum element size is set to 0.5 mm then, the surfaces are meshed by quadrilateral elements. The reason for choosing a small element size is to increase the number of nodes at radius contacts and consequently increase the accuracy of the FEM program results.

The punch, blank holder, blank and die are divided into 625, 1357, 845 and 793 elements respectively. Total of 4002 nodes are used in the FEM model. The blank material is chosen to be the Power Law Plasticity and the others are assumed to be rigid. Fully integrated shell element theory is chosen for contact calculations, which

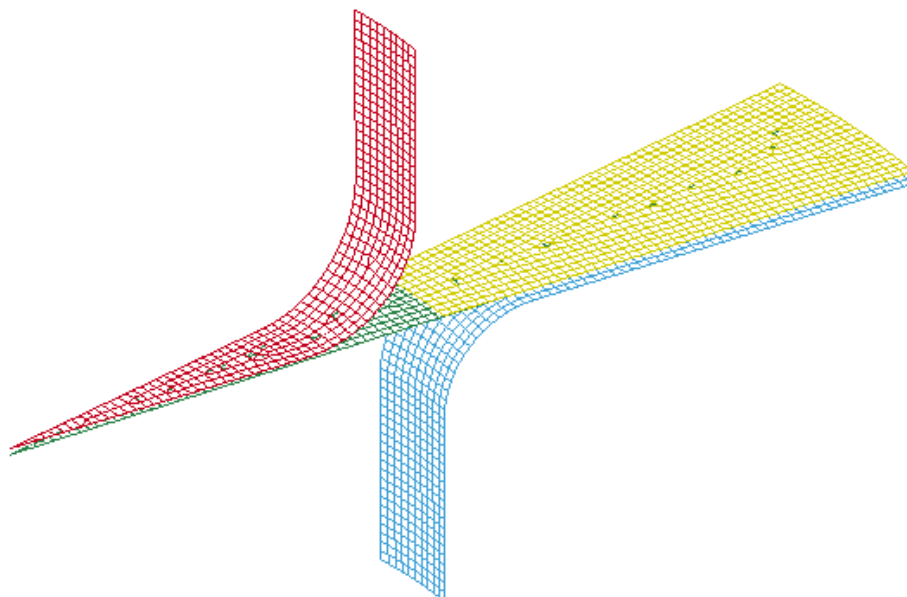


Figure 4.2 FEM model for cylindrical cup drawing

is relatively faster than other theories in LS-Dyna.

Coefficient of friction values at different contacts are input to LS-Dyna in a tabulated format. Then, the friction coefficients are determined automatically during the process with the contact pressure and local relative velocity of the contacting bodies. In every solution step, LS-Dyna uses the interpolated friction coefficient at the contact. Using tabulated data helps to reduce the computational. Sample coefficient of friction data for the punch radius contact is shown in Appendix C for cylindrical cup drawing.

First, the clamping force is increased to 0.85kN in 0.2 s. Then, the punch is forced to move in negative z direction at a constant velocity of 10 mm/s until the final cup depth of 23 mm is reached. Finally, both the pressure on the blank holder and the force on the punch are removed. Since the cup depth is smaller than the minimum dimension of the die opening, the process is classified as shallow drawing.

Boundary Conditions (BCs): Since only a wedge-shaped sector is modeled, boundary conditions are set at the boundaries of the wedge-shaped sector in order to include the effects of axisymmetry (tangential symmetry). Nodes at the edge, which are highlighted in Figure 4.3, are restricted to move in y direction. Also they are restricted to rotate about x and z axes. Since there is only cartesian coordinates available in the FEM program, the boundary conditions are specified different than cylindrical coordinates. A new local coordinate system is defined for the other edge because; it does not lie on one of the global axis like the other edge. Again similar boundary conditions are set. Additionally, the other tools are assumed to be rigid. There are some restrictions defined for their nodes. The nodes of the punch and blank holder are restricted to move in x and y axes. The nodes of the die are restricted to move in all directions.

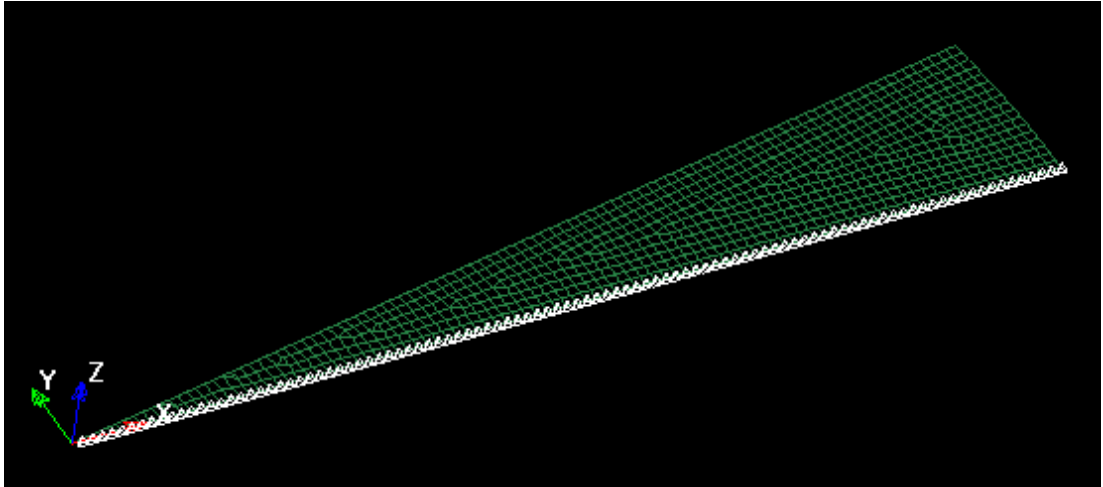


Figure 4.3 BC defined node set

4.3 FEM Program Validation

A commercial FEM program, LS-Dyna, is used to simulate the cylindrical cup drawing process. Radial, circumferential and thickness strain values are plotted with respect to their initial radial coordinates with the global origin located at the center of blank. In order to check the validity of the FEM program, two different depths are simulated for constant friction coefficient of 0.15 at the punch contact and 0.05 at the blank holder and die contacts. Then, the strain variations are compared to the results of cylindrical cup drawing of steel given in literature by Darendeliler et al. [4] for cup depths of 18 mm and 23 mm. Dynamic and static friction coefficients are assumed to be equal. Then; outputs for the nodes, which are located at the edge, are plotted and compared below.

As it was noted before, strain distribution has crucial importance in deep drawing and it must be controlled very carefully. It represents the characteristics of the drawn part and it is an easy way to check and compare the validity of the FEM model. In Figure 4.4, the radial strains are plotted with respect to their initial radial distances from the center of blank at 18 mm and 23 mm cup depths. It can be concluded that

the general characteristics of the two depths are similar to the study of Darendeliler et al. [4]. The maxima of the plots are located at the same radial distances with the same magnitudes. In spite of the similarities, there are minor differences originated from using different FEM programs and meshes with different sizes. In this study, much finer meshes are used which increases accuracy and represent changes more clearly. The radial strain distribution can be investigated region by region for better comparison.

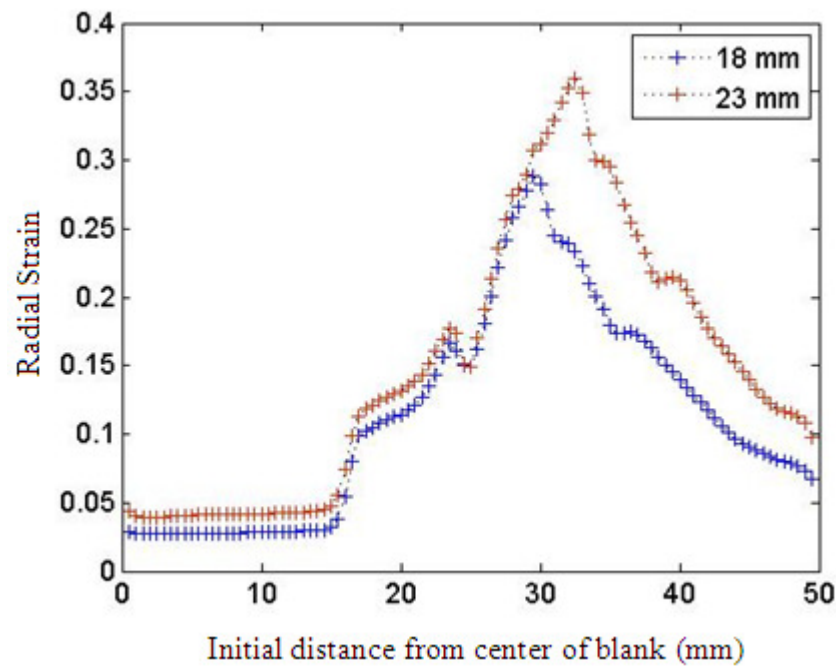


Figure 4.4 Radial strain distributions at 18 mm and 23 mm cup depths ($f_p=0.15$, $f_{die}=0.05$, $f_{bh}=0.05$)

As seen from the figure, up to the start of the punch radius contact about 16 mm, the radial strains are almost constant at 18 mm cup depth. There is only biaxial stretching until the end of the punch nose which is flat. Then, at the start of the punch radius contact there is a sharp increase in the strain. The punch radius can be referred as the

"deformation zone". There is bending and stretching in the punch radius contact which causes an increase in radial strain values. Then, about 24 mm from center, there is a small decrease in strain. The reason is that, the blank leaves the deformation zone and does not contact the punch anymore. The maximum tensile strain is obtained where the blank starts to contact with the die radius. Then, it decreases at the same rate until the end of the blank. There is a small shift (increase) about 36 mm due to transition from the die radius to the flat blank holder region. Although the general trends are similar, strain values are shifted (increased in magnitude) for 23 mm cup depth. The highest difference is observed at the beginning of the die radius contact.

The results of the circumferential strain distribution in Figure 4.5 are very similar to the study of Darendeliler et al. [4]. Again the maxima and their magnitudes are the same which also proves that the FEM model is correct. It is concluded that, using finer meshes does not significantly affect the results for circumferential strain. The reason is that, the geometry does not vary in the tangential direction as much as in radial direction. Up to the start of the die radius contact about 16 mm, the circumferential strains are almost constant and positive. Then, after a little increase, the strain values decrease almost at the same rate until blank contacts the die radius. Then, the negative strains are obtained which mean compression. As seen from the figure, the maximum compression is obtained at the start of the die radius and the maximum tension is obtained at the start of the punch radius contact in the tangential direction. The trends of the two plots are similar but, there are shifts in the plot. The magnitude of strains is higher in 23 mm cup depth. The highest shift is observed at the end of the die radius contact towards the flange region. Additionally, there is a very small waviness at the plot in flange region. The problem is originated from the thickening of the blank and free deformation which is described in previous chapters. Therefore, the blank and its characteristics are not uniform due to changing thickness in this zone. The strain magnitudes are relatively low in flange region because, the blank slides between the die and blank holder.

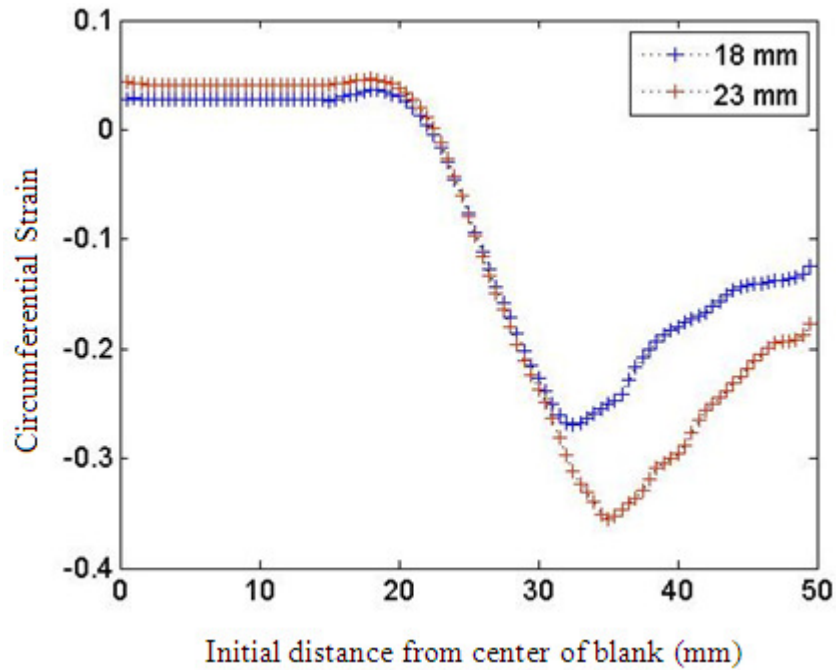


Figure 4.5 Circumferential strain distributions at 18 mm and 23 mm cup depths ($f_p=0.15$, $f_{die}=0.05$, $f_{bh}=0.05$)

In Figure 4.6, the thickness strains are plotted with respect to their initial radial distances from the center of blank at 18 mm and 23 mm cup depths. There are some major differences in the plot. Although the maxima at the plots are shifted, their magnitudes are the same. Up to the start of the die radius contact about 16 mm, the thickness strains are almost constant at each node. As the radius starts, the compressive strains increase dramatically. Then, the maximum compressive strain is obtained at the half (approximately 45°) of the punch radius contact. Since the number of nodes at the punch radius contact is high, more accurate strain distribution is obtained. It can be seen that the thickness strains are close to each other in the radius contact. The strain values change from negative to positive at the beginning of the die radius contact. The thickness strains are positive in the blank holder zone due to thickening of the blank which is described above. The trends are similar with shifts in magnitude of strains at both cup depths. Higher magnitudes of strains are obtained for 23 mm cup depth.

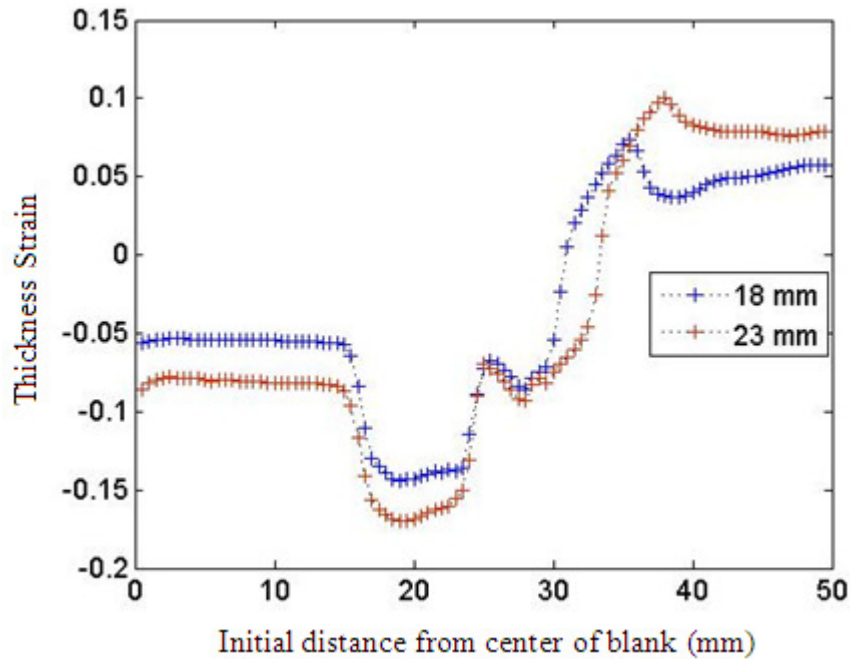


Figure 4.6 Thickness strain distributions at 18 mm and 23 mm cup depths ($f_p=0.15$, $f_{die}=0.05$, $f_{bh}=0.05$)

As a result, the strain distribution plots represent the characteristics of a deep drawing process which are also verified by the previous studies in literature [4]. Most of the differences are resulted from using different FEM programs. All the parameters and theories, which are input to the program, are also verified by comparison. The results are obtained with higher accuracy due to using finer meshes in FEM modeling.

4.4 Friction Models Code Validation

There are two different program codes written for two different friction models to be used in this study. They are based on two different approaches which are lubricant

flow and asperity contact. Before, applying program codes to the cylindrical cup drawing process and square cup drawing process, codes must be verified first. Therefore, program codes are applied to previous studies in literature [4,27].

4.4.1 Code of Khonsari's Friction Model

A program is developed for the Khonsari's friction model. The code is applied to the study of Gelinck & Schipper [27] for gear contact in spur gear transmission. The input parameters of the program are shown in Table 4.1.

Then, the code is run in MATLAB with the given parameters. The coefficient of frictions are calculated and then plotted with respect to a non-dimensional parameter, \mathcal{L} , which is shown in Figure 4.7. The plot can be called as the Stribeck curve of the spur gear contact with given parameters in Table 4.1. In order to obtain the plot, the relative velocity increased from 0.005 m/s to 5.2 m/s with 0.05 m/s increments. Since the horizontal axis is logarithmic scale, the data points get closer to each other as the relative velocity increases towards right. The friction coefficient starts from 0.13 at lower relative velocities and as the velocity increases friction coefficient decreases to 0.02. Afterwards, there is a little increase at the end of the plot where the velocity is the highest.

For the same inputs presented in the previous study of Gelinck & Schipper [27], the program code is validated by the same results and plots obtained.

Table 4.1 Spur gear contact parameters [27]

Parameter	Value	Parameter	Value
n	$1.0 \times 10^{11} \text{ mm}^{-2}$	f_c	0.13
β	10.0 μm	F	500 N
σ_s	0.05 μm	p_{av}	238 MPa
B	10 mm	W	1.08×10^{-5}
E'	231 GPa	G	4.62×10^3
R	20 mm	n'	8.94×10^5
d_a	0.058 μm	σ_s'	2.5×10^{-6}
μ_0	20 mPa.s	$n\beta\sigma_s$	0.05
α	$2.0 \times 10^{-8} \text{ Pa}^{-1}$	$4n'\sigma_s'$	8.94
τ_0	2.5 MPa		

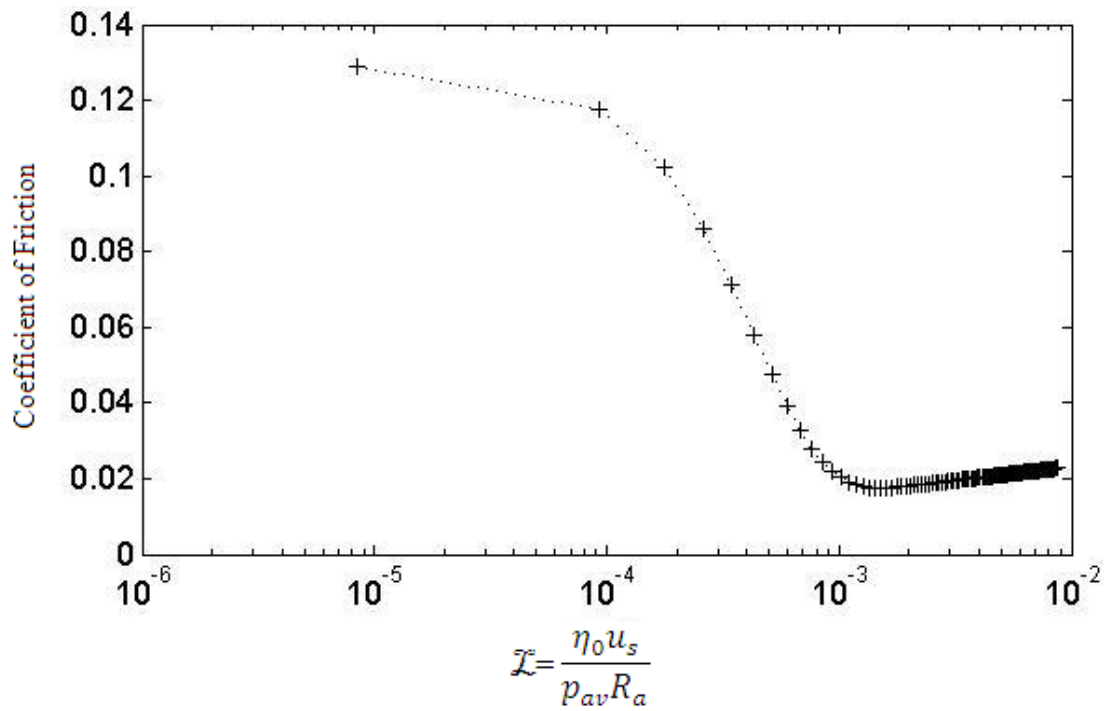


Figure 4.7 Stribeck curve for the data given in Table 4.1

4.4.2 Code of Wilson's Friction Model

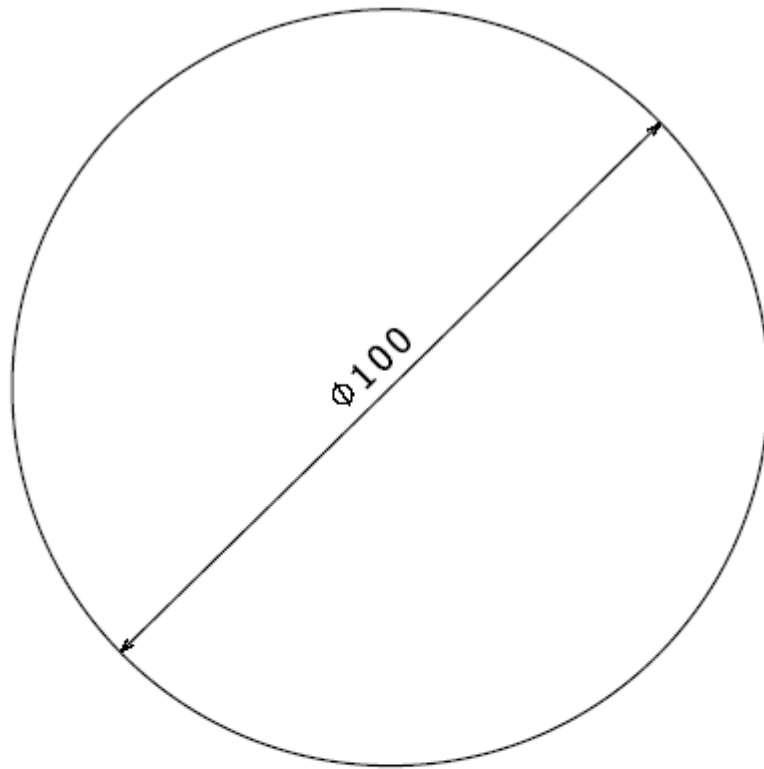
A program is developed for the Wilson's friction model. The code is applied to the study of Darendeliler et al. [4] for cylindrical cup drawing process. The input parameters of the program are shown in Table 4.2. Then, the code is run in MATLAB with the given parameters. The local friction coefficients are calculated and then plotted with respect to their initial radial distances from the center of blank. Since the same parameters of axisymmetric deep drawing are used in the literature in this study, the results are shown and compared in the results section.

Table 4.2 Axisymmetric deep drawing process parameters [4]

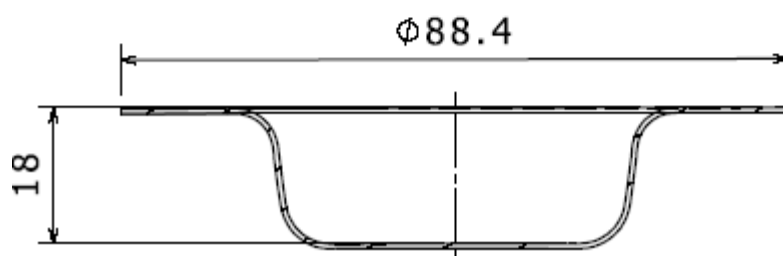
Parameter	Value	Parameter	Value
σ	0.206 μm	c	0.025
E_1	210 GPa	k	147 MPa
E_2	210 GPa	θ_t	5°
α	$2 \times 10^{-8} \text{ Pa}^{-1}$	ν_1	0.3
μ_0	0.025 Pa.s	ν_2	0.3
Yield Strength	256 MPa		

4.5 Simulation Results for Cylindrical Cup Drawing

The initial and final blank geometries of cylindrical cup drawing are shown in Figure 4.8. Two different program codes are written which read the outputs of the FEM program and calculates the friction coefficients by using Wilson's and Khonsari's friction models separately. After verification of the program codes, they are applied



(a)



(b)

Figure 4.8 (a) Initial and (b) final (18 mm cup depth) blank geometries of cylindrical cup drawing

to the outputs of the cylindrical cup drawing simulation. The calculations are performed at cup depths of 6 mm, 12 mm and 18 mm.

It is necessary to check the damping and inertial effects during the process. The main source of these effects is the punch velocity. If the velocity is too high, the punch hits the blank and the kinetic energy of the blank increases significantly. Therefore, the velocity of the punch must be carefully controlled in order to avoid damping and other inertial effects on the blank. For better comparison, kinetic and internal energies of the blank is plotted with respect to time as shown in Figure 4.9. In the figure, the internal energy of the blank increases as the process continues while the kinetic energy is almost zero during the whole process. As a result, it can be concluded that the process is not affected by unwanted inertial effects and the velocity of the punch is adjusted adequately.

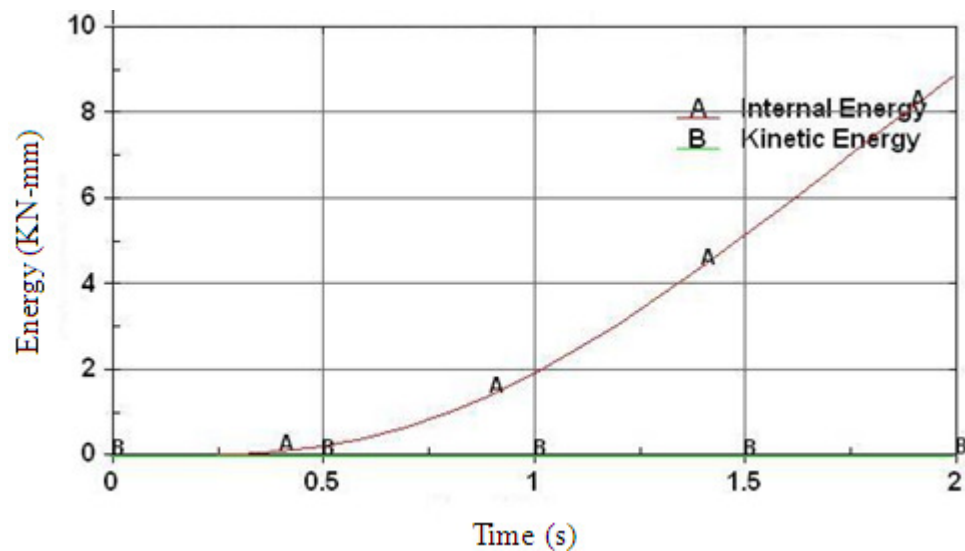


Figure 4.9 Kinetic and internal energy variation for cylindrical cup drawing

4.5.1 Von-Mises Stress Distribution

The Von-Mises stress is an index used to predict onset of yielding in ductile materials. It is a combination of principle stresses which is independent from the hydrostatic stress. It is an equivalent stress which is compared to the yield strength of the material. If its value exceeds the yielding stress then, there is yielding even though principal stresses are lower than yield stress. Therefore, instead of checking stresses in the principal axes, the Von-Mises stress is a better indicator of yielding in other words, plastic deformation. The fringe plot of Von-Mises stress distribution in the blank, for cylindrical cup drawing at 18 mm cup depth, is shown in Figure 4.10. It is seen that, the highest Von-Mises stress values are obtained at the radius of the die. The highest deformation and thinning is expected in this region. In most of the flange region, the average Von-Mises stress is higher than the punch nose region. Therefore, yielding is higher in flange region. In the wall of the drawn part, the Von-Mises stress has the lowest values just after the punch radius contact ends.

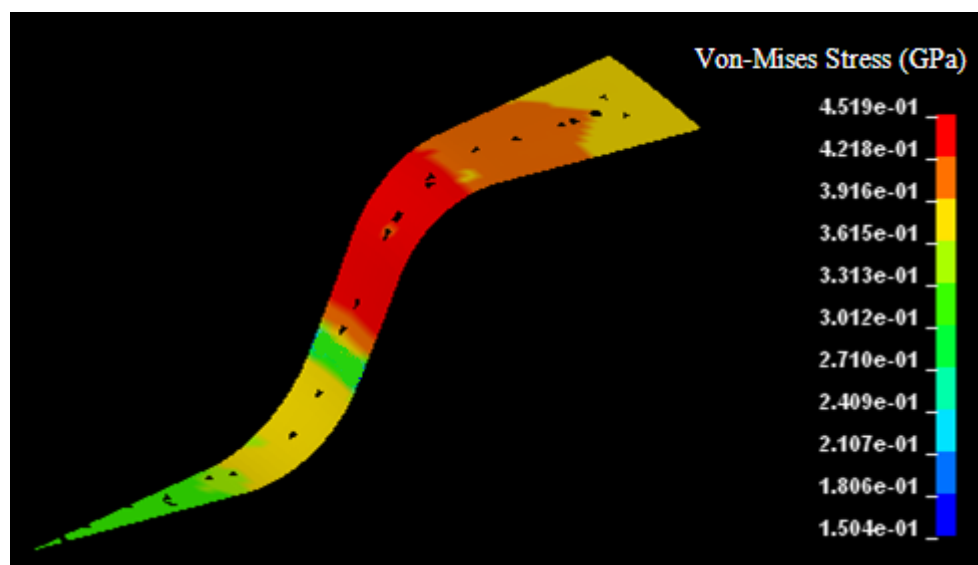


Figure 4.10 Von-Mises stress distribution for cylindrical cup drawing at 18 mm cup depth ($f_{die}=0.05$, $f_{bh}=0.05$)

Another aim of the Von-Mises stress distribution is to check whether the symmetry conditions at the boundaries are satisfied. In the figure, same colors are observed at the same radial distances as stripes. Then, the same Von-Mises stress values are obtained at both edges of the wedge-shaped sector. It can be concluded that the symmetry conditions are satisfied at the boundaries.

4.5.2 Strain Distribution

The strain distribution in the radial, tangential and thickness directions are given before in order to validate that the FEM model and simulation conditions give correct results. The effective strain distribution of the blank is shown in Figure 4.11 at 18 mm cup depth, which is useful to observe the deformation zones. The fringe plot of the upper surface of blank is shown because; it is the main deformation surface. The effective strain has the smallest values, close to zero, under the punch nose. Then, the

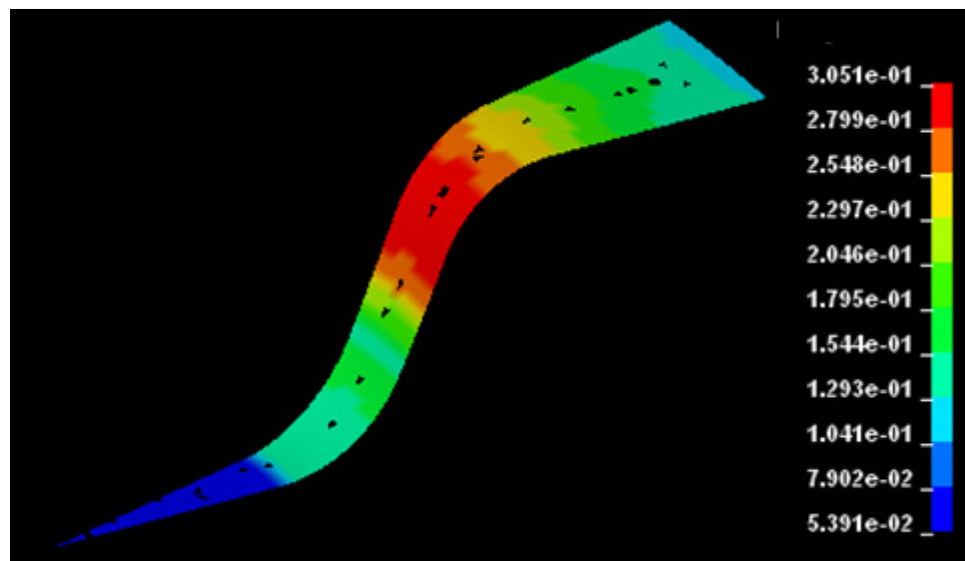


Figure 4.11 Effective strain distribution for cylindrical cup drawing at 18 mm cup depth ($f_{die}=0.05$, $f_{bh}=0.05$)

effective strain starts to increase at the beginning of the punch radius contact which is followed by a gradual increase in the wall and die radius contact respectively. The highest deformation is observed in the die radius contact for cylindrical cup drawing. In the flange region, the effective strain starts to decrease by the end of die radius and reaches almost zero at the end of the blank.

4.5.3 Thickness Distribution

Thickness distribution of the blank with respect to the initial radial distances is shown in Figure 4.12 at 18 mm cup depth. The thickness decreases from 0.6 mm at the center of the blank until the punch radius contact begins. The thickness has the smallest value (0.54 mm) at start of the punch radius contact about 19 mm from the center of the blank. Then, there is an increase, where the punch contact ends and free deformation zone starts.

Again there is a decrease in the thickness where the blank starts to contact the die radius. Afterwards, the thickness increases up to 0.69 mm which is larger than the original thickness of the blank. This is due to thickening of the blank in the flange region which is described in previous chapters. In the figure, it is seen that the critical zone is the punch nose and radius contact where there is thinning. It is concluded that the thickness reduction is small in the punch nose, within 12%, which is acceptable for steel materials. The thinnest section at the start of punch radius contact is very small but, it is the determining and most critical zone. Thinning is smaller than 14% of the original thickness of the blank so, it is also in the acceptable range.

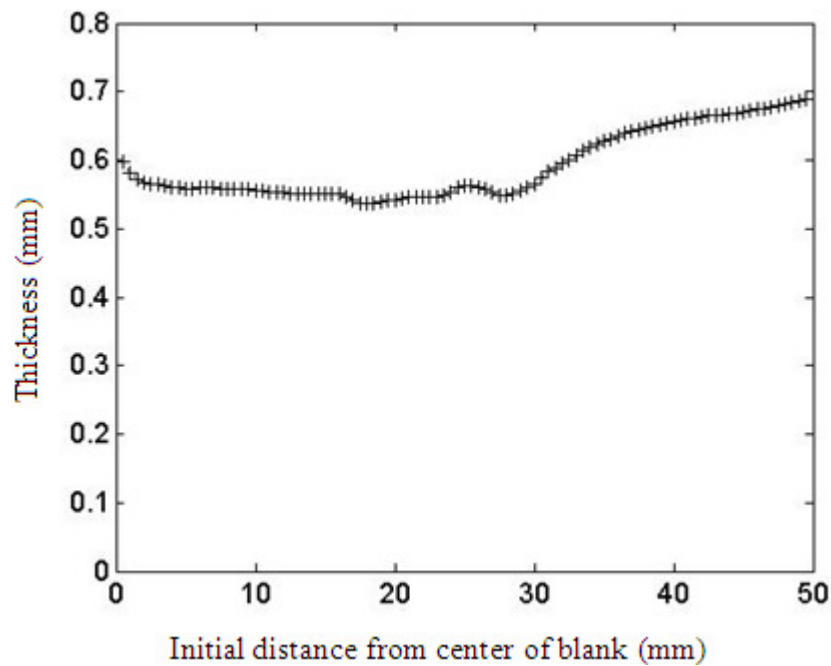


Figure 4.12 Thickness variations in the radial direction for cylindrical cup drawing at 18 mm cup depth ($f_{die}=0.05$, $f_{bh}=0.05$)

4.5.4 Punch Force Variation

The punch force is an important parameter for deep drawing process. If it is not carefully controlled, relatively higher or lower velocities are obtained in the punch which affects the strain distribution and local friction coefficients. The punch force variation with respect to cup depth is shown in Figure 4.13. In order to keep the punch velocity constant at 10 mm/s throughout the process, the punch force must be adjusted accordingly. As the cup depth increases, the punch load increases almost linearly up to 12 mm depth. Then, the punch force becomes almost constant at 26 kN, after 16 mm cup depth.

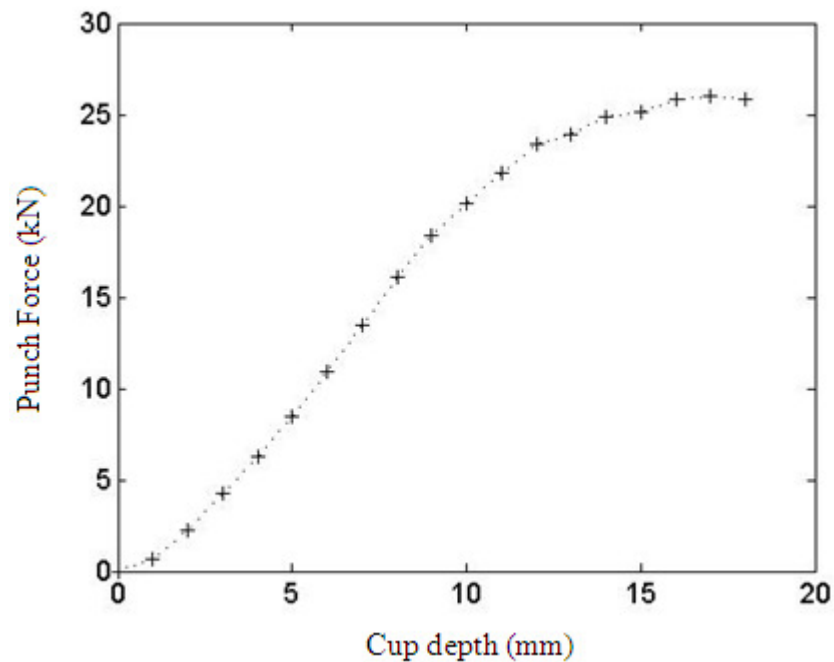


Figure 4.13 Variation of punch force in cylindrical cup drawing ($f_{die}=0.05$, $f_{bh}=0.05$)

4.5.5 Variation of Coefficient of Friction

The contact pressure is the most effective parameter in friction calculations as explained in Chapter 2. Thus, friction coefficient is highly dependent on the pressure distribution. Therefore, the trends in pressure change show similarities with the friction coefficient variation. The pressure distribution with respect to their initial radial distances from the center of blank is shown in Figure 4.14. The contact pressure is zero until the contact between the punch and blank starts at the radius of the punch. The pressure is higher at the beginning of the punch radius contact about 40 MPa. Then, there is a drop in pressure followed by a gradual increase up to 65 MPa. There is no contact in the wall part of the drawn part and the pressure is zero between 24-31 mm. The second contact starts at the beginning of the die radius about 50 MPa, which decreases gradually to 35 MPa at the end of contact. There are free zones of deformation in the flange region where there is no contact. The reason is that, thickening of the outer flange causes the blank holder to separate. In the

simulation results, high pressure values are obtained, up to 200 MPa, in the flange region because of the non-uniformity.

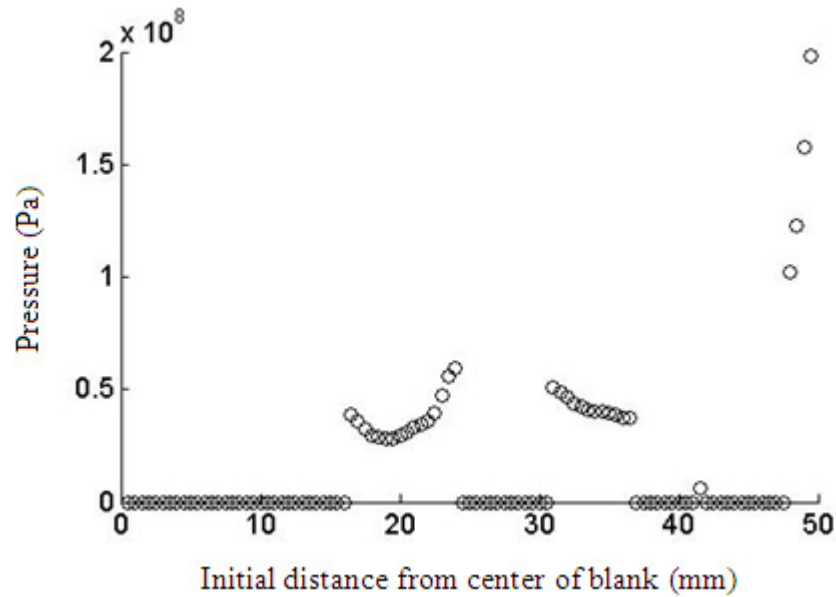


Figure 4.14 Pressure distribution for cylindrical cup drawing at 18 mm cup depth ($f_{die}=0.05$, $f_{bh}=0.05$)

The average and relative velocity variations with respect to their initial radial distances from the center of blank are shown in Figure 4.15. At the punch nose region, velocities are relatively smaller. Then, the average and relative velocities increase dramatically at the end of the punch radius contact since, the contact finishes at the end. Velocities are smaller at the die radius contact than the punch radius contact. Similarly, velocities increases close to the wall where there is stretching of the blank. At flat contacts, the average velocity is half of the relative velocity since; there is no relative movement of the punch and die with respect to the blank surface. Since, nodes at the wall do not have contacts, the average and relative velocities are zero.

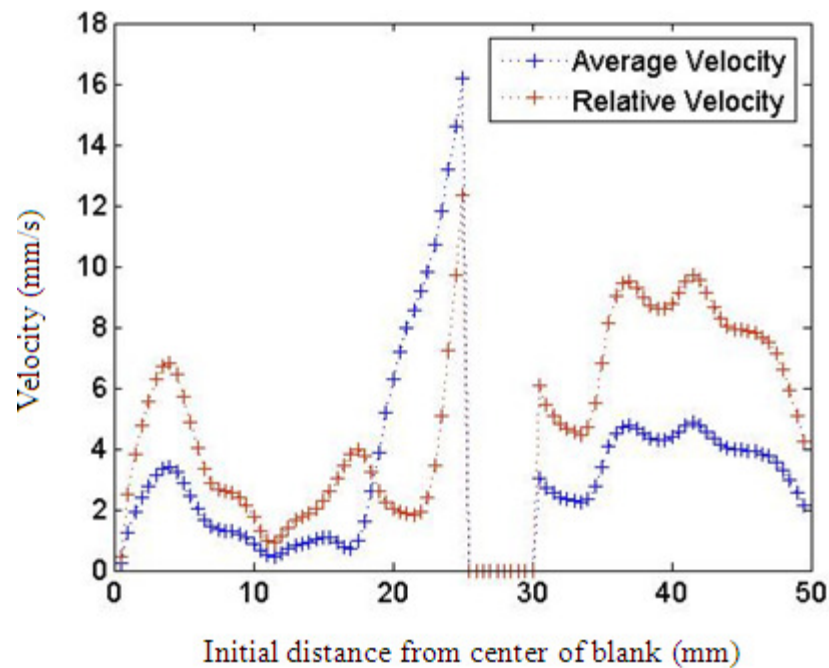


Figure 4.15 Average and relative velocity variations for cylindrical cup drawing at 18 mm cup depth ($f_{die}=0.05$, $f_{bh}=0.05$)

Film thickness is an important parameter which can be used to differentiate lubrication regimes and it is determined by the pressure and local average velocity of the contacting bodies. The film thickness variation with respect to their initial radial distances from the center of blank is shown in Figure 4.16. If the film thickness increases, surface separation increases and asperity interaction decreases. At higher contact pressures, the film thickness is expected to be lower and vice versa. As seen from the figures, it is not the case. The local average velocity is dominant in the film thickness variation. Especially at the end of the punch radius contact, the film thickness increases due to higher average velocity of the punch and blank. Similar effect is observed at the end of the die radius contact where, the film thickness increases dramatically while contact pressure is decreasing at a small rate.

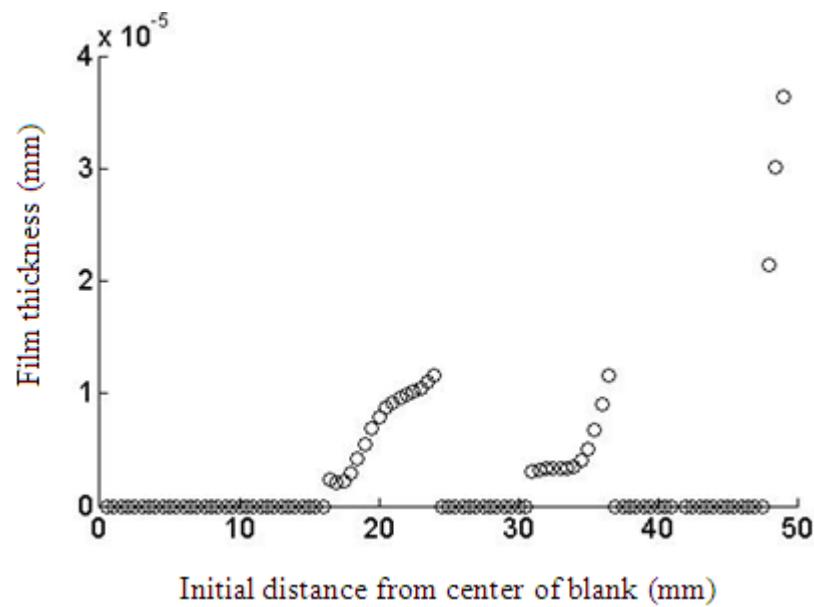


Figure 4.16 Film thickness variation for cylindrical cup drawing at 18 mm cup depth ($f_{die}=0.05$, $f_{bh}=0.05$)

The film thickness ratio variation with respect to their initial radial distances from the center of blank is shown in Figure 4.17. The film thickness ratio is used to determine the load shared by the asperities and lubricant. Also, it is used by the Wilson's friction model, in order to differentiate between lubrication regimes. The film thickness ratios which are lower than 3, are either in the BL regime or ML regime according to the friction model. Therefore, there is not a clear differentiation of the regimes where the lubricant or asperities is dominant in friction.

It is seen from the figure that, the ratios obtained at different contacts in cylindrical cup drawing, are smaller than 0.1 which is a relatively small ratio. Different film thickness ratios are tested to find an optimum ratio, which can be used to divide the boundary and mixed lubrication regimes, in order to determine whether Khonsari's or Wilson's friction model is more suitable. Khonsari's friction model is applied below the selected ratio and Wilson's friction model is applied at higher ratios. It is found that, below the ratio of 0.035 Wilson's model gives very high and unrealistic friction coefficient results, especially at lower contact pressures. Therefore, at film

thickness ratios lower than 0.035, it is assumed that the asperities are more effective in friction and Khonsari's friction model is more suitable and at higher ratios, lubricant is more effective and Wilson's friction model is more suitable.

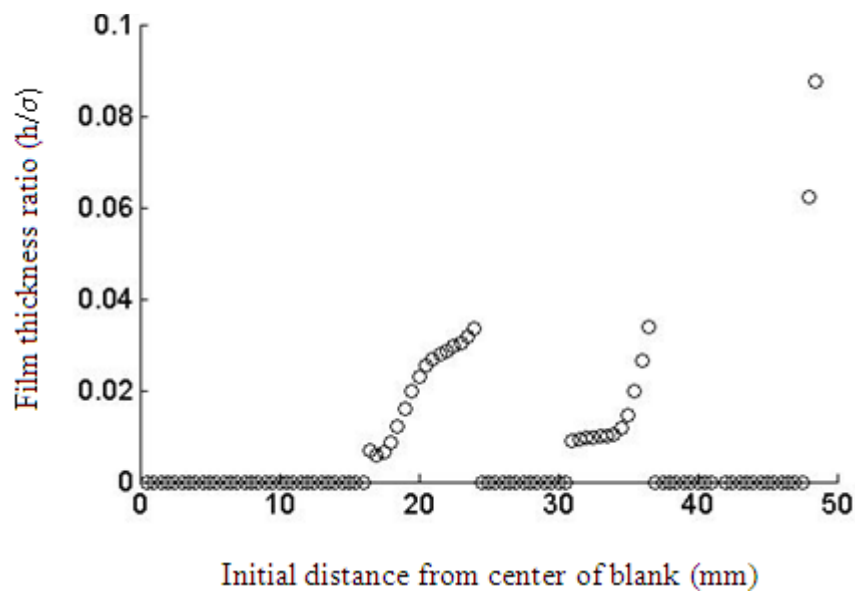


Figure 4.17 Film thickness ratio (h/σ) variation for cylindrical cup drawing at 18 mm cup depth ($f_{die}=0.05$, $f_{bh}=0.05$)

Scaling factor is an important parameter in friction calculations which shows how the load is shared by the asperities and lubricant. γ_1 is related to the load carried by the asperities and γ_2 is related to the load carried by the lubricant. Scaling factor variations with respect to their initial radial distances from the center of blank are shown in Figure 4.18. Since γ_1 and γ_2 values vary in a wide range, $1/\gamma_1$ and $1/\gamma_2$ are plotted in the figure for better comparison. The summation of the $1/\gamma_1$ and $1/\gamma_2$ values are equal to 1, which is obtained from Equation (3.49). The trends are determined by the film thickness distribution and relative velocity at the interface.

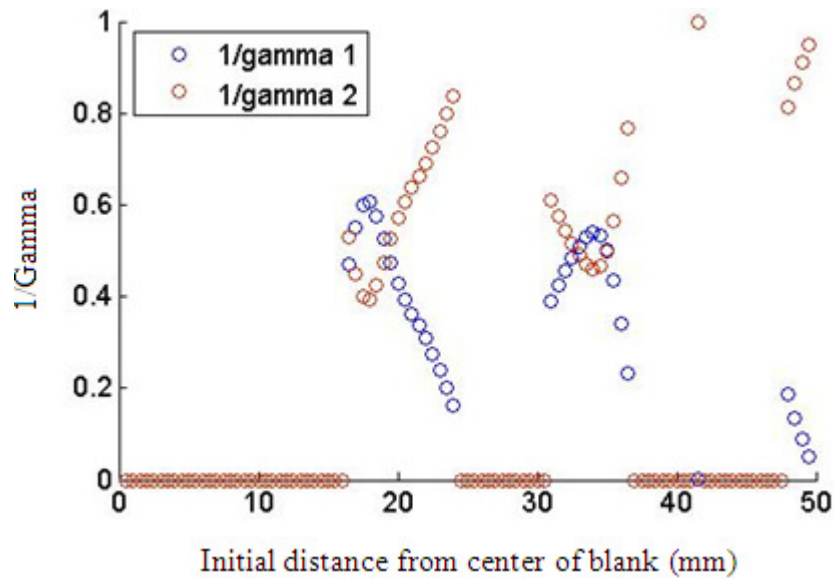


Figure 4.18 Scaling factor variations for cylindrical cup drawing at 18 mm cup depth ($f_{die}=0.05$, $f_{bh}=0.05$)

At the punch radius contact, the load carried by the lubricant decreases at the beginning which is followed by a sharp increase as the film thickness increases through the end of contact. The reason is that, separation of the surfaces causes less interaction of the asperities. At the beginning of the punch radius contact, the load carried by the lubricant is higher due to high relative velocity although, the contact pressure is higher and film thickness is lower in this region. At the die radius contact, similar trend is observed where the load carried by the lubricant is high especially, at higher film thickness values. At both contacts, the lubricant is dominant in load carrying. In the flange region, the lubricant is dominant while the load carried by the asperities is almost negligible.

In Figure 4.19, the local friction coefficients are plotted with respect to their initial radial distances from the center of blank which are calculated by Wilson's and Khonsari's friction models [1,33]. In Wilson solution, the results and general trends are similar to the studies in literature. The friction coefficient varies with similar trends. It is important to note that, the friction is more effective and meaningful in the radius regions of the punch and die since, large deformations are observed in these

regions. As seen from the figure, there is no friction within 16 mm, since there is no contact between the punch nose and the blank. As it was noted before, the punch nose is not effective in deep drawing process and this region is not worth investigation. After 16 mm, the contact starts at the beginning of the punch radius. Then, the friction coefficient starts about 0.08 at first nodes in Wilson solution which is a little bit lower than Khonsari solution. Then, the friction coefficient increases a little bit and decreases gradually to 0.05 at the end of the radius contact in Wilson solution. The trend is a little different for Khonsari solution in which the friction coefficient starts about 0.09 and then, drops to 0.03 at the end of radius contact which is lower than Wilson solution. It is concluded that Wilson's friction model is highly dependent on the film thickness variation at the punch radius contact since friction coefficient decreases with increasing film thickness. Khonsari solution shows similar trends with the pressure distribution therefore, it is concluded that Khonsari's friction model is highly dependent on the pressure distribution.

Between the die and punch, called as wall of the drawn part, the blank material deforms freely where there is no physical contact. As a result, there is no friction in this region. After the wall, the die radius contact starts and the friction coefficient starts with 0.06 and increases to 0.09 in Wilson solution. In Khonsari solution, friction coefficient starts a little bit higher. Then; instead of increasing like Wilson's solution, the trend changes and friction decreases to 0.06. The reason is that, Wilson's friction model is concentrated at the flow and increasing film thickness causes the friction coefficient to increase. Khonsari's friction model is concentrated on the asperities then, decreasing contact pressure also decreases friction coefficient. Also, Khonsari's friction model is more sensitive to changes in the die radius contact than Wilson's friction model. Most of the flange region is classified as free deformation zones and only there is contact at the outer part of the flange. Then, the coefficient of friction has values lower than 0.03 in this region.

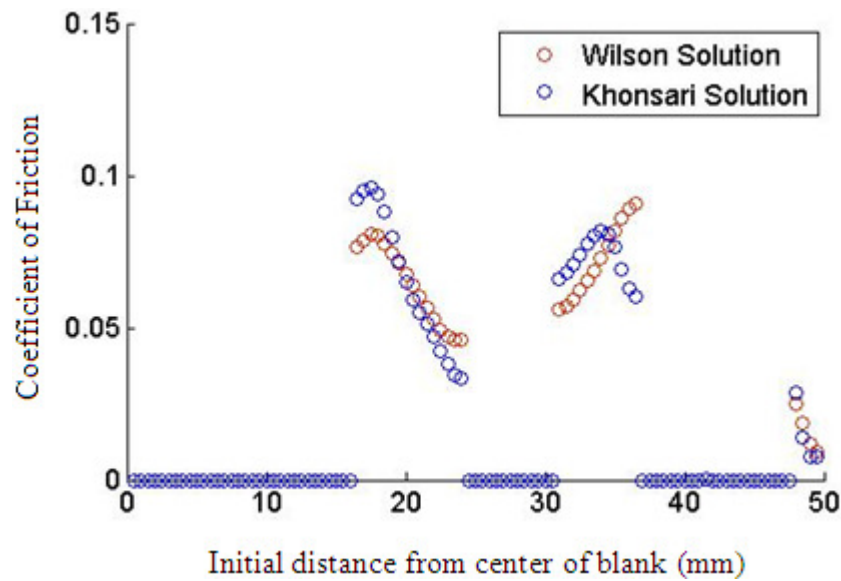


Figure 4.19 Variation of local friction coefficient for cylindrical cup drawing at 18 mm cup depth ($f_{die}=0.05$, $f_{bh}=0.05$)

4.5 The Combined Friction Model

There are two different friction models and approaches explained in Chapter 3 by Wilson and Khonsari. Although some of the parameters are similar, formulations and solving methods are totally different from each other. Khonsari's friction model requires iterative solving of nonlinear equations which takes a lot of computational time. Initial guesses and tolerances affect the calculations and the accuracy of the results. The main purpose of this study is to use Wilson's model as the main friction model because, it is easier and faster to apply. Then, employ the Khonsari's friction model at the BL regime and at some portion of the ML regime (close to the BL regime) where Wilson's model is not accurate enough. As it was mentioned before, formulations of boundary lubrication are very rough in Wilson's model [1]. In literature, film thickness ratios (h/σ) are commonly used to differentiate between lubrication regimes. Then, after a number of runs and comparing the results, a film thickness ratio of 0.035 is taken below which, Khonsari's model is suitable for

application. Since, pressures are very high in deep drawing processes; the film thickness ratios are relatively smaller. The determining parameter in the film thickness ratio for which Khonsari's model can be applied is the combined surface roughness of both surfaces. By changing its value, even if the film thickness does not change significantly, the film thickness ratio changes accordingly.

First of all, Wilson's friction model is used to calculate the film thickness. Then, film thickness ratio is calculated. Below the film thickness ratio of 0.035, Khonsari's model is applied. The reason is that, as the ratio decreases more asperities contact and load is transferred within the asperities. Khonsari's model gives better results because; its theory is based on asperity contact. Wilson's model is used for the rest of the ratios which are higher than 0.035. At higher ratios, lubricant becomes more effective at load transfer and Wilson's model is based on lubricant flow. As a result, combining two models results in a wider solution domain with higher accuracy. Also, the computational time is decreased significantly. A program code is developed for the combined friction model. The program code in MATLAB, is given in Appendix D. The flowchart of the combined friction model is shown in Figure 4.20.

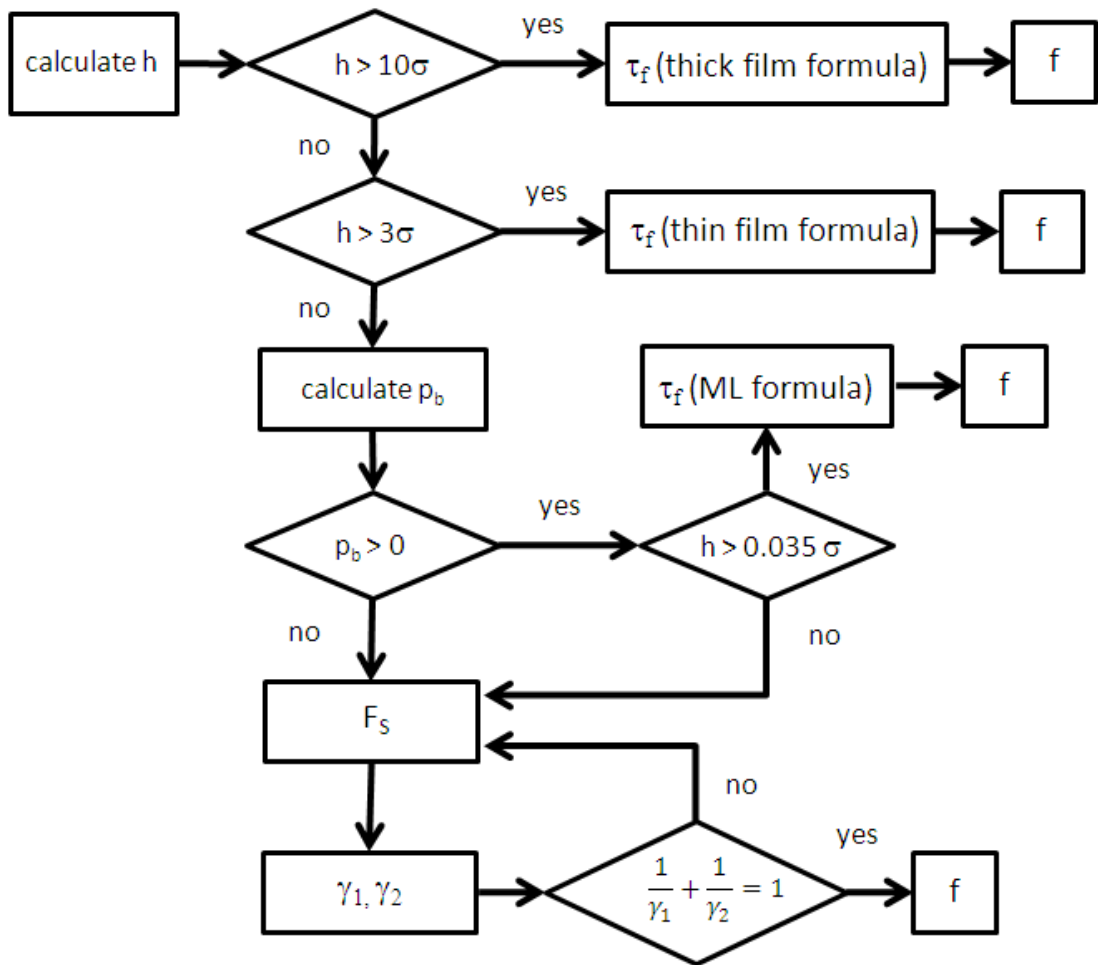


Figure 4.20 Flow chart of the combined friction model

4.7 Parameters for Cylindrical Cup Drawing

A program code is developed in order to combine the friction models of Wilson and Khonsari. Input parameters of the combined friction model are shown in Table 4.3 for cylindrical cup drawing. Then, the code is run in MATLAB with the given parameters. Finally, friction coefficients are calculated and then plotted with respect to their initial radial distances from the center of blank.

Table 4.3 Cylindrical cup drawing process parameters

Parameter	Value	Parameter	Value
σ	0.206 μm	σ_s	0.15 μm
E_1	210 GPa	k	147 MPa
E_2	210 GPa	θ_t	5°
α	$2 \times 10^{-8} \text{ Pa}^{-1}$	ν_1	0.3
μ_0	0.025 Pa.s	ν_2	0.3
f_c	0.15	Yield Strength	256 MPa
n	$1.9 \times 10^{10} \text{ m}^{-2}$	c	0.025
β	13 μm	τ_0	2.5 MPa

4.8 Results of the Combined Friction Model

The local friction coefficient variation, with respect to the initial radial distances from the center of blank, is shown in Figure 4.21. In order to see the variation of the friction throughout the process, different cup depths are plotted, which are 6 mm, 12 mm and 18 mm. First of all, it is concluded that the friction coefficients show similar

trends at all cup depths. At the punch and die radius contacts, the highest friction coefficients are obtained at 18 mm cup depth and lowest coefficients are obtained at 12 mm cup depth. At the punch radius contact, 12 mm and 18 mm cup depths show similar trends. Coefficient of friction varies between 0.1 and 0.04 and almost the same nodes are in contact with the punch radius. At both cup depths, the friction decreases in the radial direction which is different than 6 mm depth. At 6 mm cup depth, less number of nodes is in contact with the punch radius since, blank just starts to conform the punch profile and the friction coefficient varies between 0.06 and 0.07.

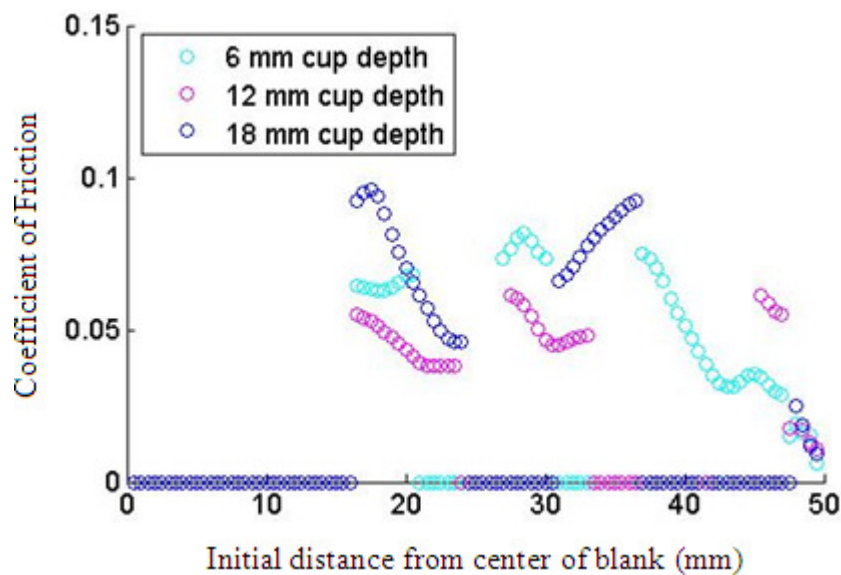


Figure 4.21 Variation of local friction coefficient for cylindrical cup drawing at cup depths of 6 mm, 12 mm and 18 mm ($f_{die}=0.05$, $f_{bh}=0.05$)

At the die radius contact, all the cup depths show different trends. Since there is more sliding of nodes in the die radius contact, there are differences at initial distances from center. The highest variation in the coefficient of friction is obtained at 18 mm cup depth which is changing between 0.07 and 0.09. Unlike other depths, the friction

coefficient has a decreasing trend at 12 mm cup depth. The friction coefficient increases a little bit which is followed by a decrease at 6 mm cup depth.

In the flange region, the contact area changes due to thickening and consequently, the number of nodes. Trends of the friction variation at all cup depths are similar. At 6 mm cup depth, almost all of the nodes are in contact and the friction coefficient decreases from 0.07 to 0.01 at the end of the blank. There is a jump in friction variation as the thickening effect starts at 6 mm cup depth. The number of nodes is less for 12 mm cup depth where the friction varies about 0.06. At 18 mm cup depth, the contact area becomes very small and it is located at the outer edge of the blank. Due to very high pressures, friction coefficients are smaller than 0.03 in the flange region at 18 mm cup depth.

CHAPTER 5

CASE STUDY: SQUARE CUP DRAWING

Program codes of the two different friction models are verified separately in the previous chapter. Then, a new combined friction model is introduced in order to increase efficiency and reduce computational time in a larger domain. In this chapter, combined model is applied to a square cup deep drawing process as a case study. Process parameters such as geometries, velocities are chosen arbitrarily from the previous studies in literature.

5.1 Deep Drawing Components

In this section, deep drawing parameters and components are explained for square cup drawing.

The Tool: The punch, die and blank holder materials are assumed to be rigid. The punch has a profile and edge radius of 6 mm. There is 48.35 mm length between the faces of the square punch. Clearance between the punch and die is set to be 1.05 mm. The die has a profile radius of 8 mm. The die and blank holder both has an outer diameter of 130 mm. Tool geometries and dimensions, in millimeters, are shown in Figure 5.1.

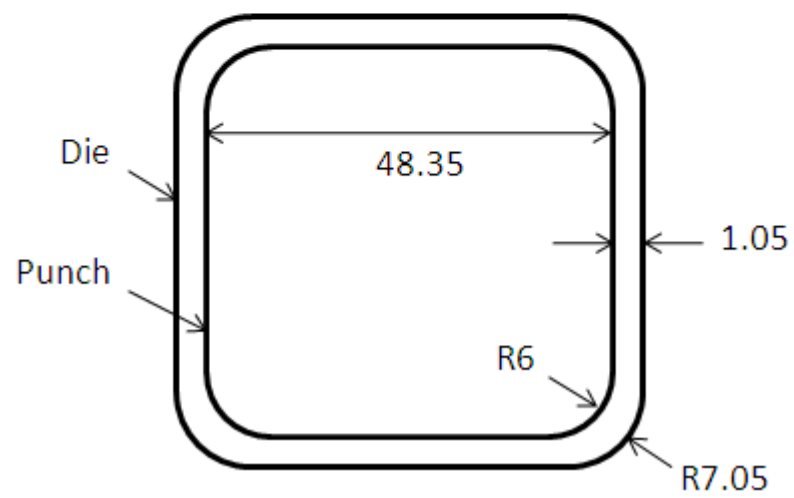
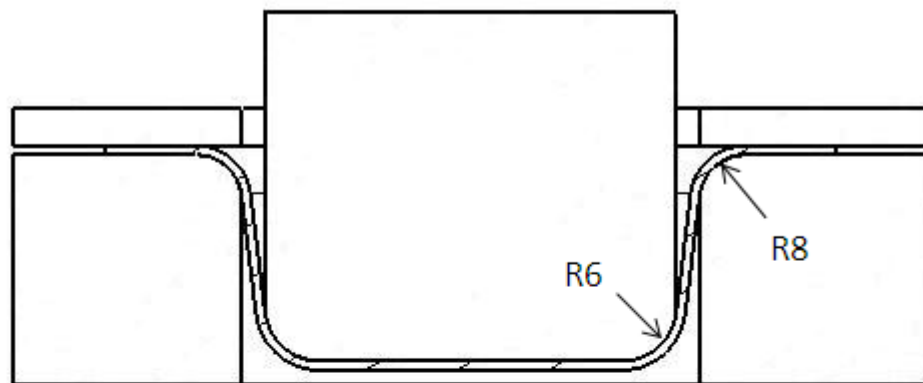


Figure 5.1 Tool geometry of square cup drawing

The Blank: The blank material is same as the one used in cylindrical cup drawing process except its thickness. It is a steel sheet with a diameter of 130 mm. The thickness is increased to 0.8 mm. The reason is that, while drawing to the same depth, the blank deforms more in square cup drawing than cylindrical cup drawing especially at the corners. The failure risk of blank is reduced by this way. Instead of a square shaped blank a circular blank is used, which is more common in square cup drawing.

Lubricant: The same lubricant in cylindrical cup drawing, is used which can operate at a wide temperature range. The dynamic viscosity at atmospheric pressure is taken as 0.025 Pa.s and pressure viscosity index is $2 \times 10^{-8} \text{ Pa}^{-1}$.

5.2 FEM Model of Square Cup Drawing

The blank, punch, blank holder and die are modeled as surfaces by using a commercial CAD program. The FEM model is shown in Figure 5.2. Only 1/8 portion of the blank is investigated for decreasing simulation time since there are symmetry conditions. Then, they are imported to the preprocessor of FEM program. The maximum element size is set to 0.5 mm then, the surfaces are meshed by quadrilateral elements. The reason for choosing a small element size is to increase the number of nodes at radius contacts and consequently increase the accuracy. The element size is chosen to be the same size with cylindrical cup drawing because; radius lengths of the tooling are similar. Then, the number of nodes at radiuses is close to each other and sufficient accuracy is achieved.

The punch, blank holder, blank and die are divided into 2260, 5164, 6821 and 6572 elements respectively. Total of 21378 nodes are used in the FEM model. The blank material property is chosen to be Power Law Plasticity and others are assumed to be rigid. Fully integrated shell element theory is chosen for contact calculations, which is relatively faster than other theories.

First, the clamping force is increased to 3.7 kN in 0.2 s. Then, the punch is forced to move in negative z direction at a constant velocity of 10 mm/s until the final cup depth of 18 mm is reached. Finally, both the pressure on the blank holder and the force on the punch are removed. Since the cup depth is smaller than the minimum dimension of the die opening, the process is classified as shallow drawing.

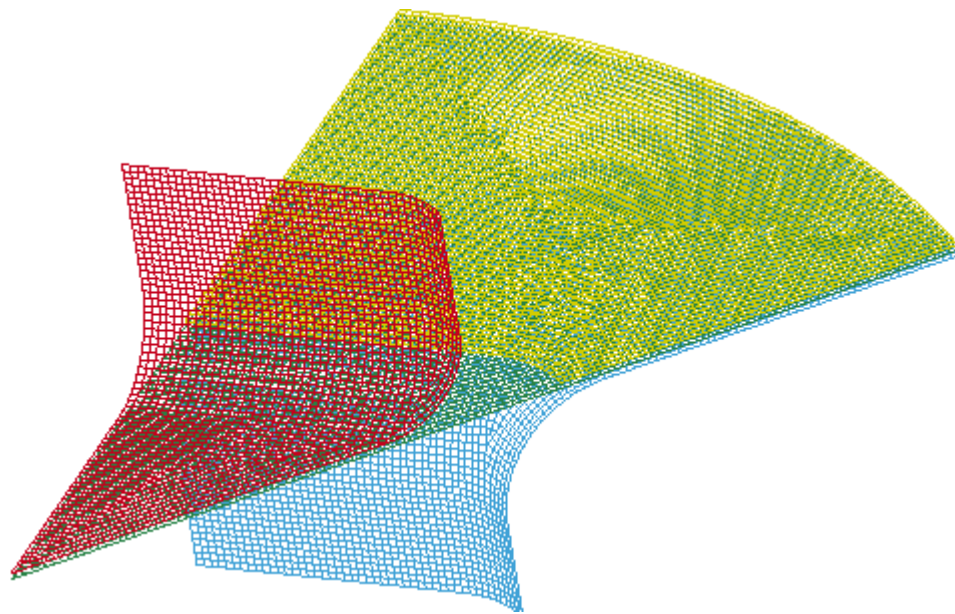


Figure 5.2 FEM model for square cup drawing

Boundary Conditions (BCs): Since only 1/8 portion of the system is modeled, boundary conditions are set at the boundaries of the meshes in order to include the effects of symmetry. Nodes at the edge, which are highlighted in Figure 5.3, are restricted to move in y direction. Also they are restricted to rotate about x and z axes. Two different local coordinate systems are defined for both edges because; they do not lie on one of the global axes. Again, similar boundary conditions are set for the second node set. Additionally, other tools are assumed to be rigid. There are some restrictions defined for their nodes. Nodes of the punch and blank holder are

restricted to move in x and y axes. Nodes of the die are restricted to move in all directions.

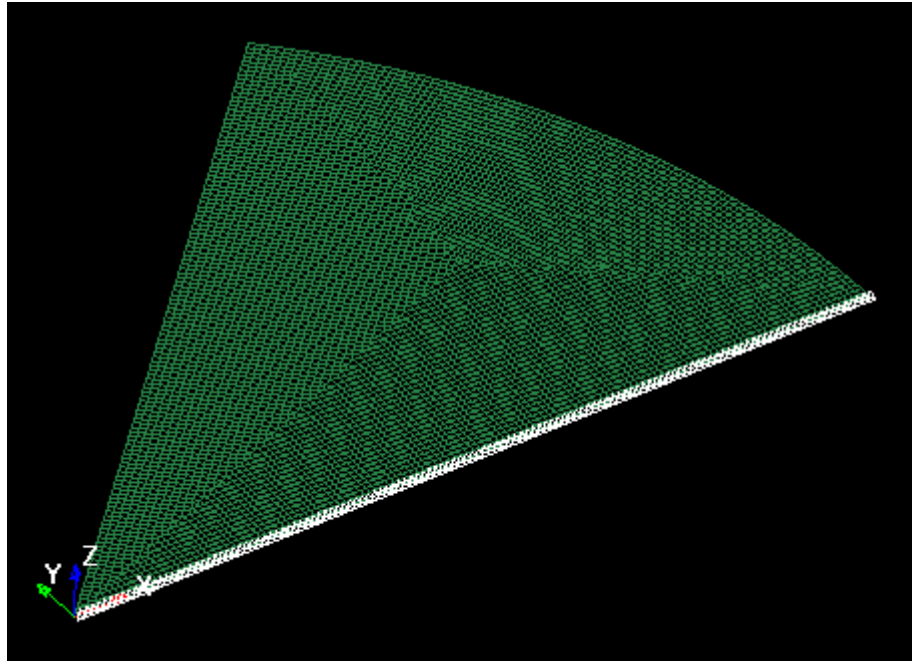


Figure 5.3 BC defined node set for square cup drawing

5.3 Parameters for Square Cup Drawing

Input parameters of the combined friction model are shown in Table 5.1 for square cup drawing. Then, the code is run in MATLAB with the given parameters. Finally, friction coefficients are calculated and then plotted with respect to their initial radial distances from the center of blank.

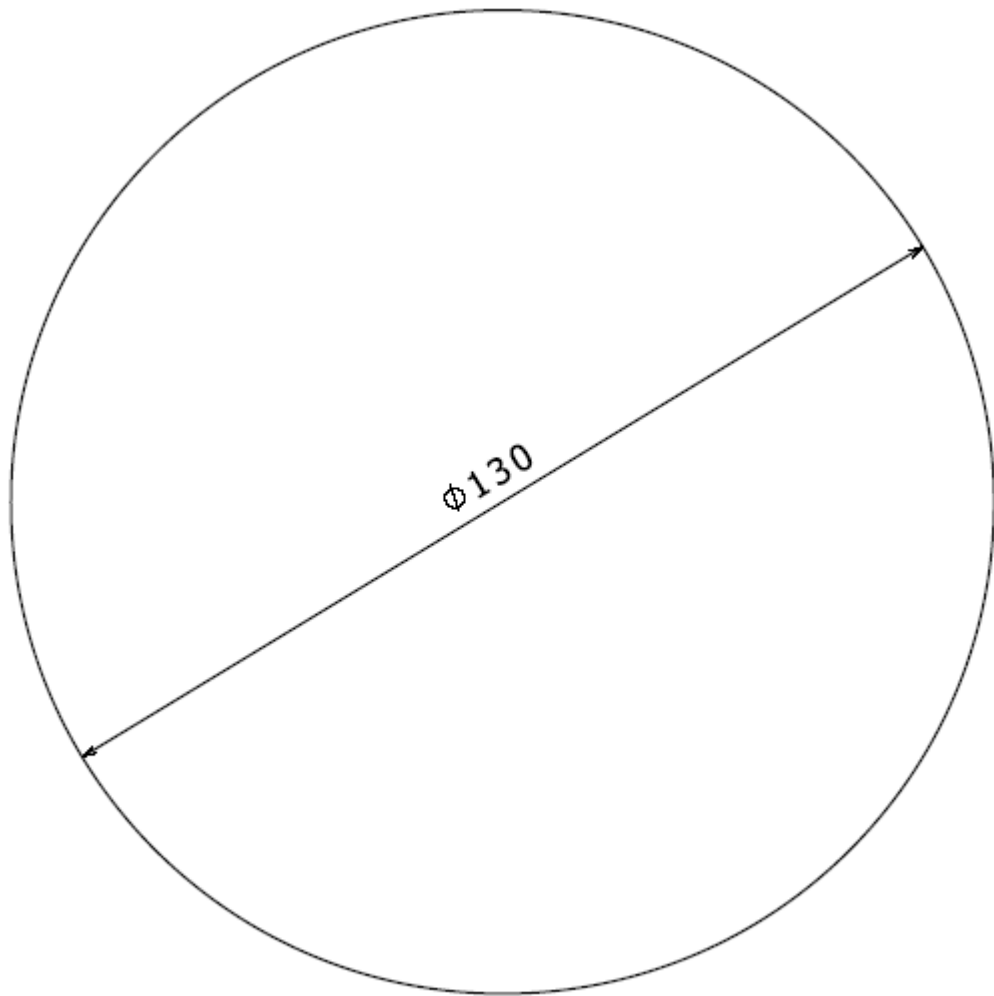
Table 5.1 Square cup drawing process parameters

Parameter	Value	Parameter	Value
σ	0.206 μm	σ_s	0.15 μm
E_1	210 GPa	k	147 MPa
E_2	210 GPa	θ_t	5°
α	$2 \times 10^{-8} \text{ Pa}^{-1}$	ν_1	0.3
μ_0	0.025 Pa.s	ν_2	0.3
f_c	0.15	Yield Strength	256 MPa
n	$1.9 \times 10^{10} \text{ m}^{-2}$	c	0.025
β	13 μm	τ_0	2.5 MPa

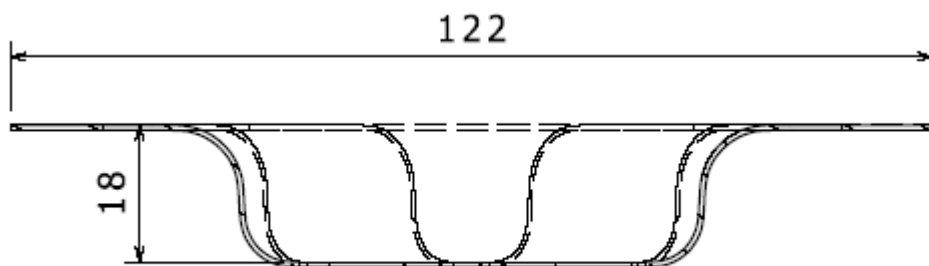
5.4 Simulation Results for Square Cup Drawing

The initial and final blank geometries of square cup drawing are shown in Figure 5.4. The combined friction model is applied to the outputs of square cup drawing simulation obtained from LS-Dyna. Then, the strain distribution and the local friction coefficients are calculated along 0° and 45° directions as shown in Figure 5.5.

Similar to cylindrical cup drawing, damping and inertial effects must be checked for the exactness of the process. Kinetic and internal energies of the blank are plotted with respect to time as shown in Figure 5.6. In the figure, the internal energy of the blank increases as the process continues while kinetic energy is almost zero during the whole process. As a result, it is concluded that the process is not affected by unwanted inertial effects and the velocity of the punch is selected correctly. It is important to note that; the internal energy is much higher square cup drawing than cylindrical cup drawing, which is approximately 7.5 times larger. More internal energy increase is needed for the blank in order to deform to the same cup depth.



(a)



(b)

Figure 5.4 (a) Initial and (b) final (18 mm cup depth) blank geometries of square cup drawing

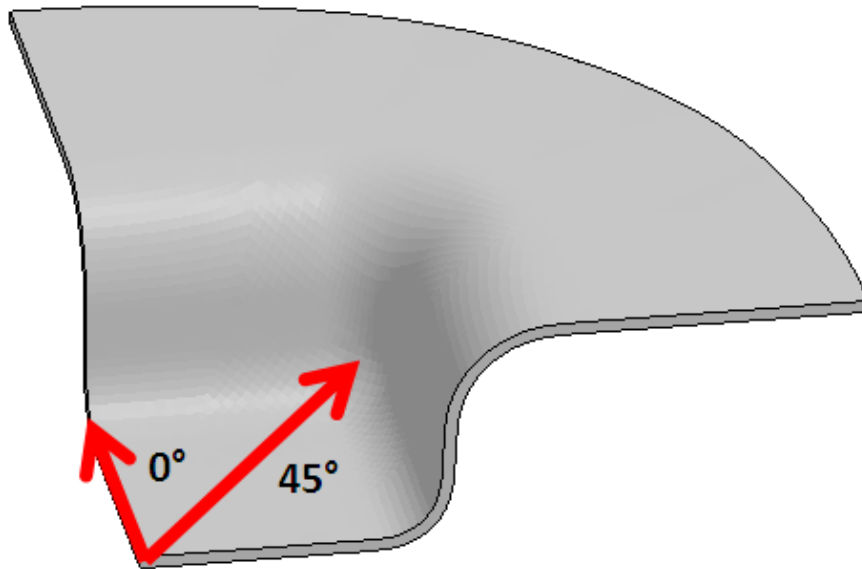


Figure 5.5 0° and 45° directions of blank in square cup drawing

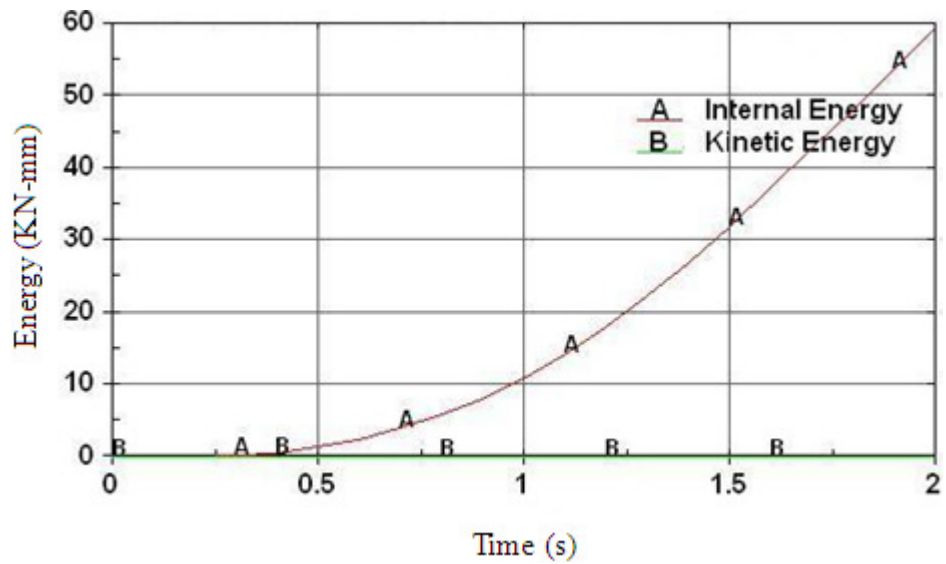


Figure 5.6 Kinetic and internal energy variation for square cup drawing

5.4.1 Von-Mises Stress Distribution

The Von-Mises stress distribution for square cup drawing at 18 mm cup depth is shown in Figure 5.7. It is seen that, Von-Mises stresses are higher along 45° direction at the radius regions of the punch and die. The highest values are obtained in the punch radius contacts in both directions. The highest deformation and thinning are expected in the radius regions of punch along 45° direction. In most of the flange region, the average Von-Mises stress is higher than the punch nose region. Therefore, yielding is higher in the flange region. At the end of the blank, there is no yielding along 45° direction while, along 0° direction yielding occurs at higher Von-Mises stress values.

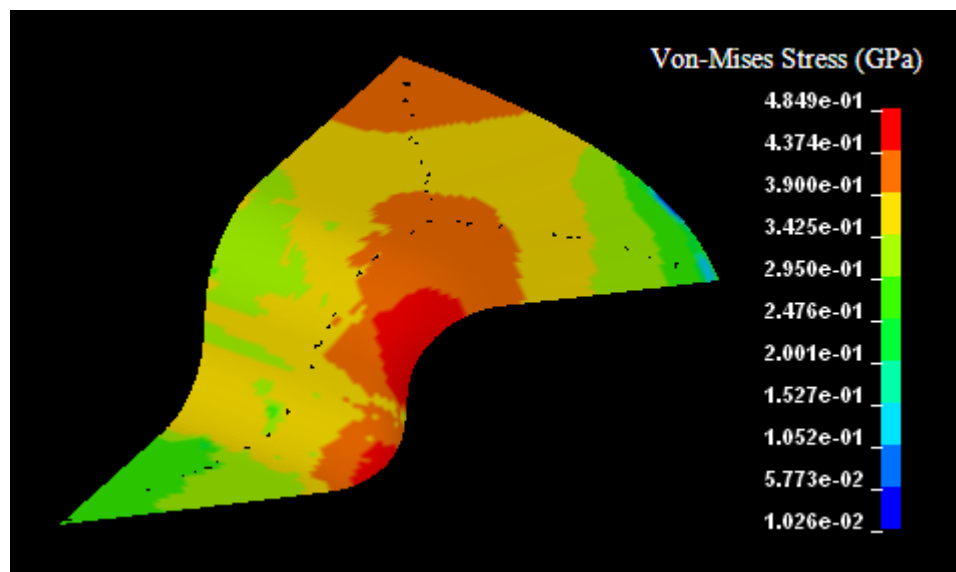


Figure 5.7 Von-Mises stress distribution for square cup drawing at 18 mm cup depth ($f_{die}=0.05$, $f_{bh}=0.05$)

5.4.2 Strain Distribution

The strain distribution is investigated for two different node sets. The first node set is located along 0° direction. The second node set is located along 45° direction, which is on the diagonal of the square. Nodes which are located at the diagonal of square cup are more important. The reason is that, the deformation is higher and more critical in this cross-section. The drawability and quality of the square cup mainly depends on the strain distribution along 45° direction.

Square cup drawing process is simulated with the given parameters up to 18 mm cup depth. Strain values are obtained and plotted with respect to their initial distances from the center of blank. The results of the thickness strain distribution along 0° and 45° directions are shown in Figure 5.8. Along 0° direction, the strain distribution is

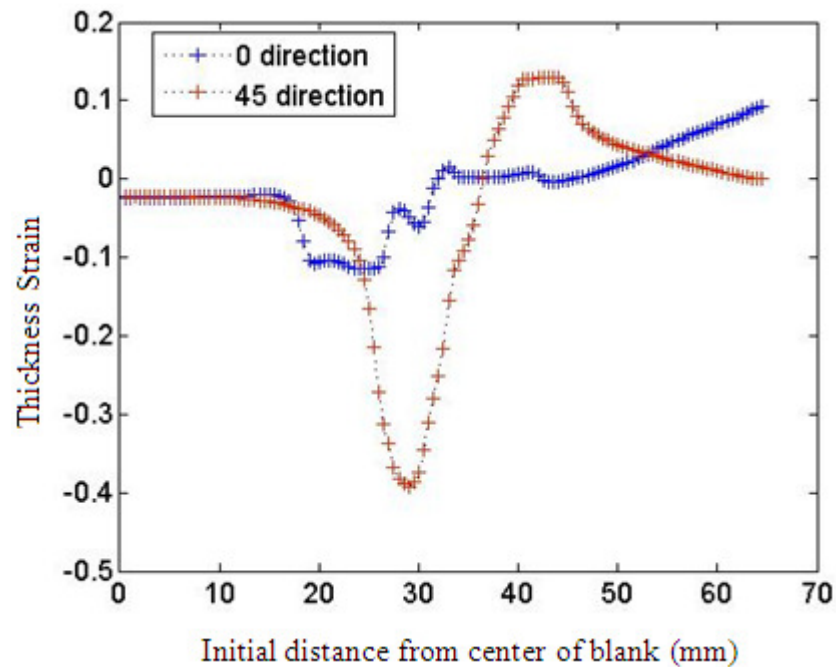


Figure 5.8 Thickness strain distributions for square cup drawing along 0° and 45° directions at 18 mm cup depth ($f_{die}=0.05$, $f_{bh}=0.05$)

not uniform as 45° direction. There are sudden jumps and discontinuities in the strain values. There is thickening of the blank along 0° direction. Thickness strain values are positive but small in magnitude within 19 mm. At the beginning of the punch radius contact, there is a jump and strain values continue to increase until the contact ends. The highest thickness strain is obtained at the end of the punch radius contact about 24 mm from the center. The thickness strain starts to decrease at the die radius contact. As the die radius contact ends, strain values start to increase and become constant for the rest of the flange region.

Along 45° direction, the strains are negative and small in magnitude at nodes which are in the punch nose region. Therefore, there is thinning due to stretching. As the punch radius contact starts about 20 mm, the negative strains increase in magnitude and the thickness strain reaches the minimum at the end of the radius contact about 30 mm. The thickness strain changes its sign in the wall of the drawn part and becomes positive. The highest positive strain is obtained at the beginning of the die radius contact about 40 mm. Then, the strains start to decrease after the die radius contact, under the squeezing force of the blank holder in the flange region.

The results of the strain distribution in rolling direction along 0° and 45° directions are shown in Figure 5.9. Along 0° direction, strains in rolling direction are negative and small in magnitude within 19 mm. At the beginning of the punch radius contact, negative strains increase in magnitude suddenly and the highest compression is obtained. At the punch radius contact, strain values are almost constant. Then, negative strains start to decrease in magnitude at the beginning of the die radius contact and become positive at the end of die radius. Strains in rolling direction, is constant at some portion of the flange region which is followed by an increase in magnitude until the end of blank. Along 45° direction, strains in rolling direction are positive and almost constant at the punch nose contact within 24 mm. There is a sudden increase in strain values at the beginning of the die radius contact about 25 mm. A local maximum strain is observed at the center of the die radius contact along 45° direction. After a minimum at the end of the die radius contact, the maximum strain is observed at the start of the flange region. Strain values in rolling direction; start to decrease after the maximum and reaches to zero at the end of the blank. It is

seen that; strain values are not uniform in the flange region as it is in cylindrical cup drawing. There is waviness and a sudden trend change in strain values.

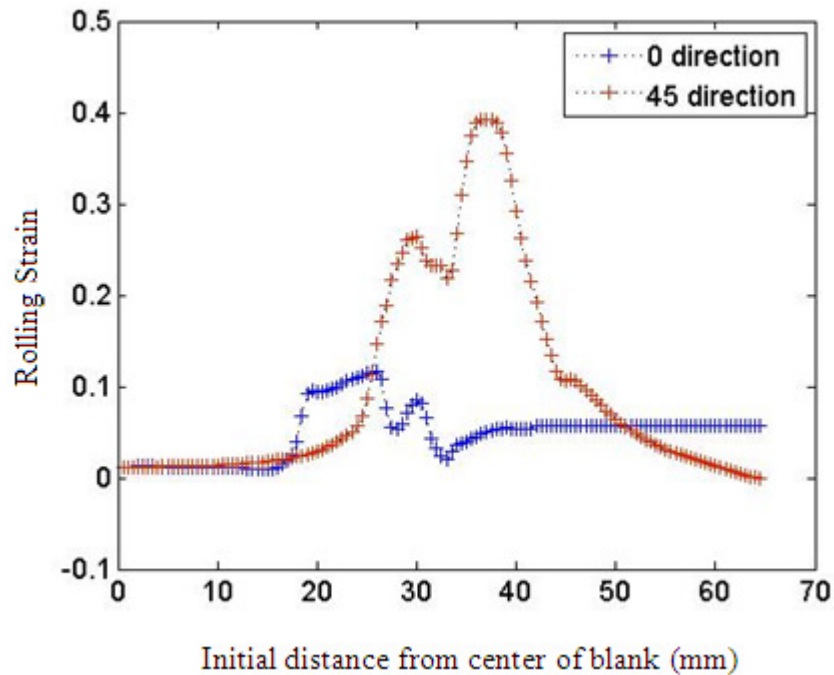


Figure 5.9 Strain distributions in rolling direction for square cup drawing along 0° and 45° directions at 18 mm cup depth ($f_{die}=0.05$, $f_{bh}=0.05$)

The effective strain variation is shown in Figure 5.10 at 18 mm cup depth, which is useful to observe the deformation zones in square cup drawing. Fringe plot of the upper surface of the blank is shown because; it is the main deformation surface. First of all, the effective strain has higher values in square cup drawing than cylindrical cup drawing therefore, square cup drawing is more critical. 45° direction shows similarities with cylindrical cup drawing but, 0° direction shows different characteristics than others. The deformation is very low in the punch nose region, since the effective strain is close to zero. Then, the effective strain increases suddenly in the punch radius contact along 45° direction, while along 0° direction, it does not

increase that much. The highest strain is observed in the die radius contact along 45° direction which is followed by a decrease until the end of the blank. It is interesting to note that, strain values are almost zero in the die radius contact along 0° direction which means the deformation is very low.

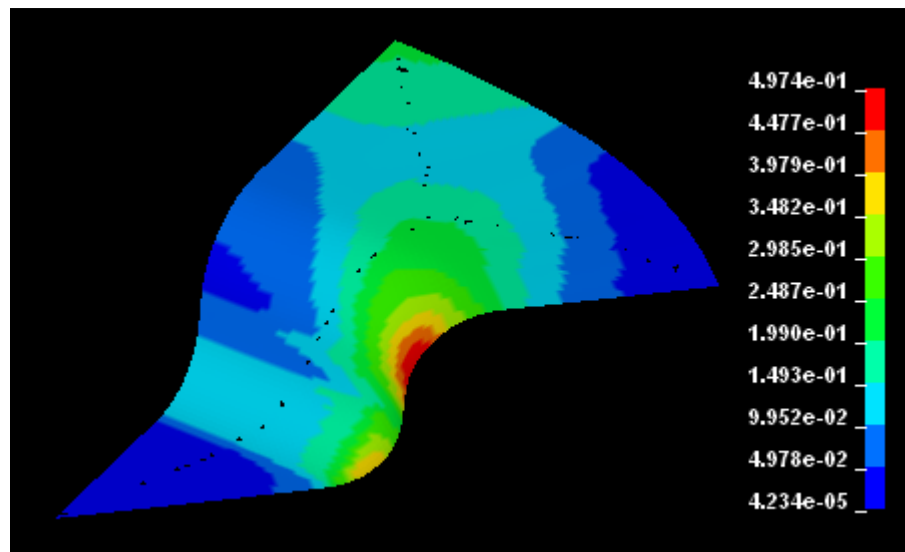


Figure 5.10 Effective strain distribution for square cup drawing at 18 mm cup depth ($f_{die}=0.05$, $f_{bh}=0.05$)

5.4.3 Thickness Distribution

Since the deformation concentrates more in square cup drawing, thickness changes are more critical and must be controlled carefully. Otherwise, risks of failure or crack initiations may increase. Thickness variations of the blank along 0° and 45° directions are shown in Figure 5.11. As seen from the figure, there is excessive thinning at the corners of the square cup.

Along 0° direction, the thickness is a little bit decreased and almost constant from center to the end of the die radius contact. The blank material thickness is larger than the original thickness in the flange region. So, there is thickening of the blank in this region. This trend continues until the end of the blank. Along 45° direction, the thickness is decreased by a very small amount and almost constant in the punch nose region. Then, there is a sharp decrease to 0.58 mm at the beginning of the punch radius contact. After the minimum, thickness continues to increase in the radial direction. After the die radius contact, thickness of the blank is larger than the original thickness even though thickness decreases in the radial direction until the flange ends. Therefore, there is thickening in the flange region.

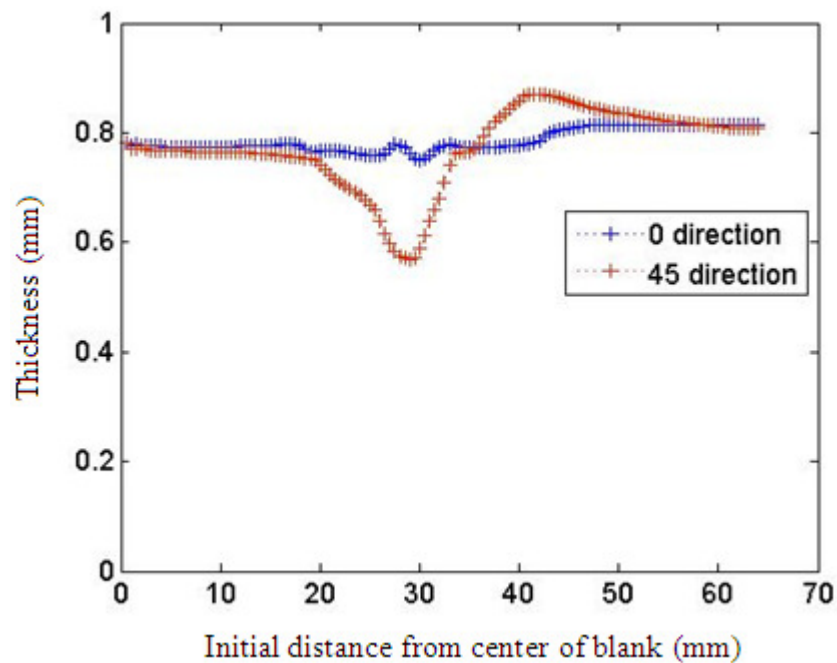


Figure 5.11 Thickness change along 0° and 45° directions for square cup drawing at 18 mm cup depth ($f_{die}=0.05$, $f_{bh}=0.05$)

5.4.4 Punch Force Variation

The punch force variation shows similar trends with cylindrical cup drawing results, which are represented in Chapter 4. The punch force variation is shown in Figure 5.12 with respect to the cup depth. The punch force increases linearly as the cup depth increases. Force increases linearly until 14 mm depth is reached and afterwards, it does not increase at the same rate. Then, the punch force becomes almost constant and reaches 51 kN at 18 mm depth.

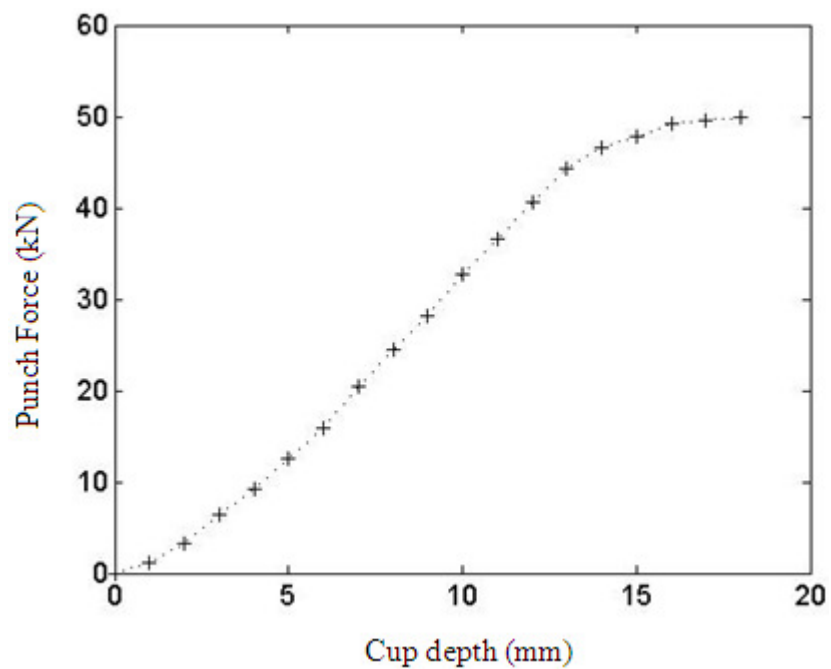


Figure 5.12 Variation of punch force in square cup drawing ($f_{die}=0.05$, $f_{bh}=0.05$)

5.4.5 Variation of Coefficient of Friction

Friction calculations are based on two different directions which are 0° and 45° directions for square cup drawing. Both directions have totally different characteristics such as the contact pressure distribution, strain rate and local velocities. Similar to cylindrical cup drawing, the friction variation is highly affected by the pressure distribution. First of all, the pressure distribution in two directions must be investigated in order to relate to the friction variations. Pressure distributions for square cup drawing along 0° and 45° directions are shown in Figure 5.13. Along 0° direction, the contact pressure is zero until the contact between the punch and blank starts at the radius of the punch. At the beginning of the punch radius contact, the pressure is about 50 MPa about 19 mm which increases to 70 MPa at the end of the contact. Then, the contact between the punch and blank ends and the pressure is zero at the wall of the drawn part where there is no contact. At the die radius contact, the pressure varies between 30-40 MPa. At the flange region, only the outer part of

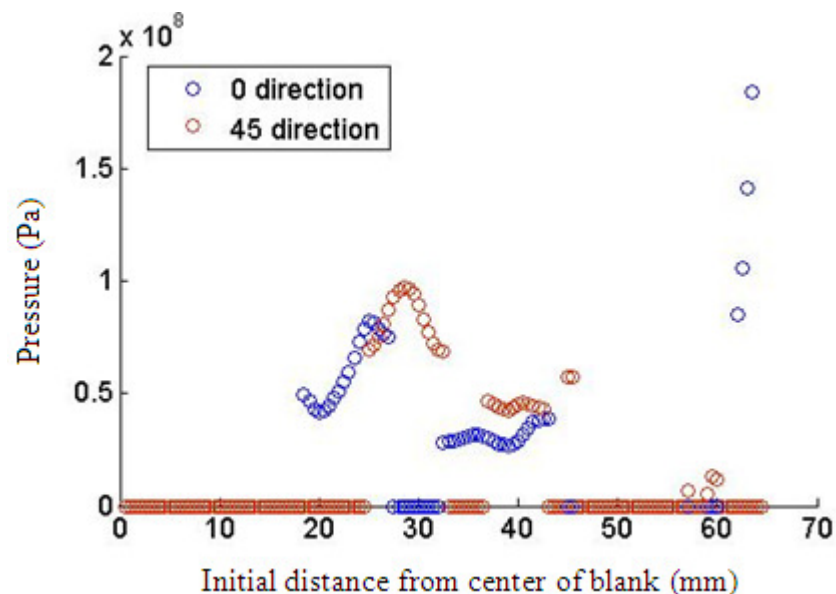
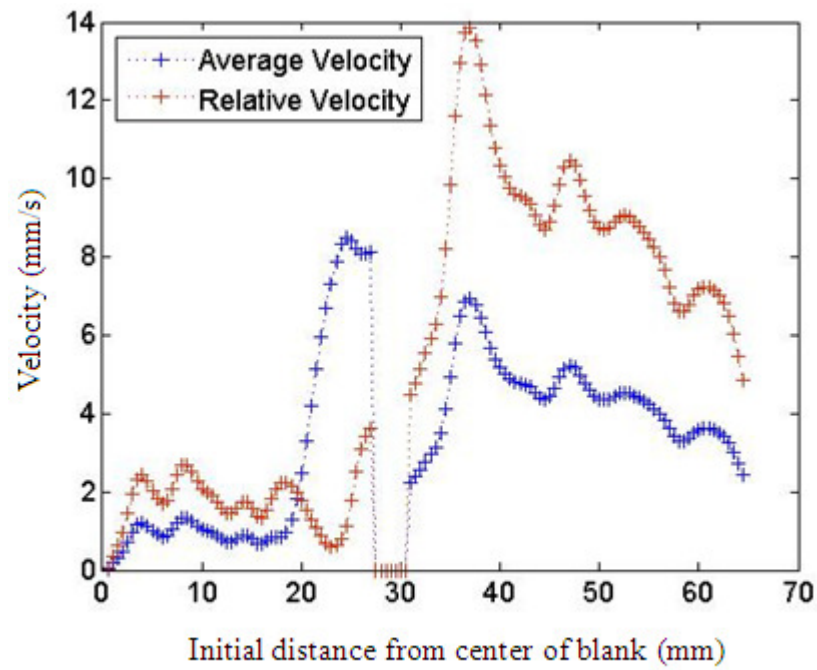


Figure 5.13 Pressure distributions for square cup drawing along 0° and 45° directions ($f_{die}=0.05$, $f_{bh}=0.05$)

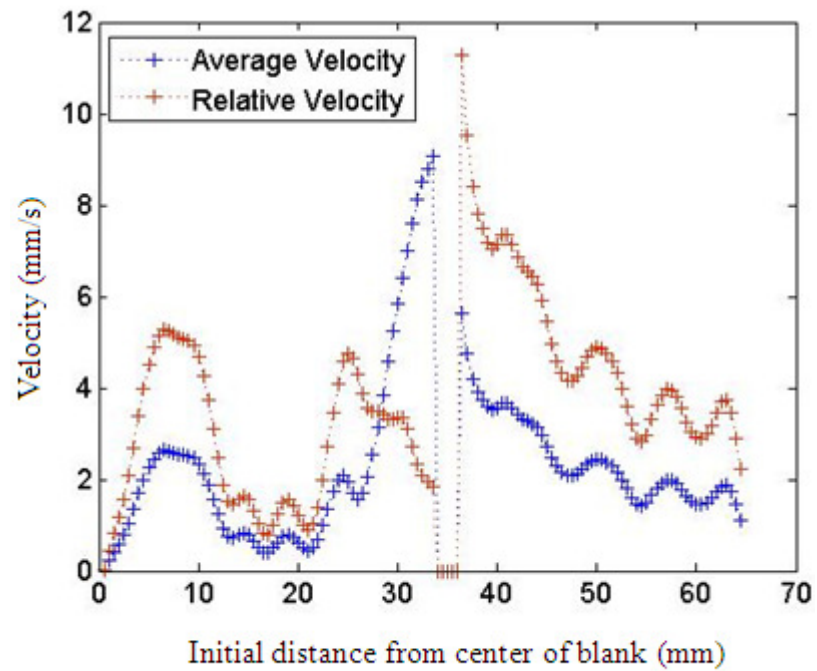
the blank contacts with the tooling due to thickening of the blank. Inner flange is called as the free deformation zone without contact. Along 45° direction, the pressure is zero until the contact between the punch and blank starts at the radius of the punch, which is similar to 0° direction. At the punch radius contact, the pressure is about 70 MPa at the start and end of the contact. Then, the pressure reaches the maximum at the center of the punch radius contact about 100 MPa. In the wall part there is no contact and pressure. The pressure is almost constant in the die radius contact about 45 MPa. Due to thickening in 0° direction, the blank holder separates and the pressure is very low in a small portion of the flange region.

The average and relative velocity variations are shown in Figure 5.14, along 0° and 45° directions. Along 45° direction, the trends in velocity changes are similar to cylindrical cup drawing. Velocities are increases close to the wall in radius contacts. In the flange region, velocities are smaller than the die radius contact while in cylindrical cup drawing the trend is opposite. Along 0° direction, velocities decrease at the die radius contact close to the wall which is different than other directions. Velocities are relatively higher in the flange region. It was noted before that, effective strain is almost zero at the wall along 0° direction. Therefore; stretching is lower than the other directions, which causes the velocities to decrease. In both directions, the average and relative velocities are zero at the nodes, which are in the wall of the drawn part, since there is no contact.

Film thickness variations are shown in Figure 5.15, along 0° and 45° directions. At the punch radius contact, the average velocity of the contacting bodies is dominant since, the film thickness increases while the contact pressure is increasing along 0° direction. Especially, the average velocity is higher through the end of the punch radius contact. The trend is opposite along 45° direction. The film thickness increases at a smaller rate while the contact pressure is also decreasing. Therefore, the contact pressure is dominant in this direction. At the die radius contact, the film thickness variation is determined by the pressure distribution in both directions. But, there is a small drop at the beginning of the die radius contact, due to decreasing average velocity. There are a few data points in the flange region which makes it hard to observe the trends.



(a)



(b)

Figure 5.14 Average and relative velocity variations for square cup drawing (a) along 0° direction (b) along 45° direction at 18 mm cup depth ($f_{die}=0.05$, $f_{bh}=0.05$)

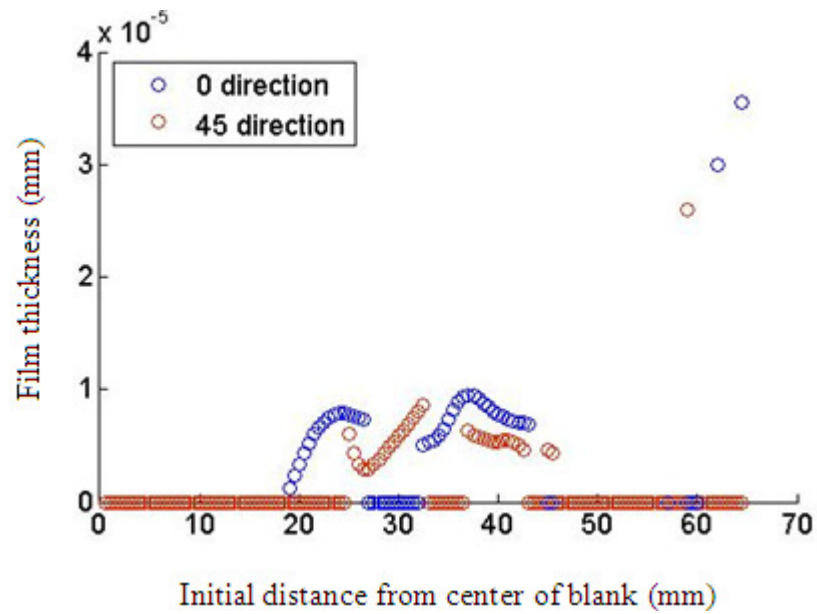


Figure 5.15 Film thickness variation along 0° and 45° directions for square cup drawing at 18 mm cup depth ($f_{die}=0.05$, $f_{bh}=0.05$)

The film thickness ratio variations with respect to their initial radial distances from the center of blank are shown in Figure 5.16. The ratios are similar to the ones calculated for cylindrical cup drawing in Chapter 4. Since, the order of the ratios are similar, film thickness ratio of 0.035 can also be used in square deep drawing which was obtained to determine the friction model for cylindrical cup drawing. Good results are also obtained for square cup drawing with the same film thickness ratio criteria. Combined surface roughness is assumed to be constant at each contact therefore; the variation of film thickness ratio is same as the variation of film thickness. Only difference is in the magnitudes.

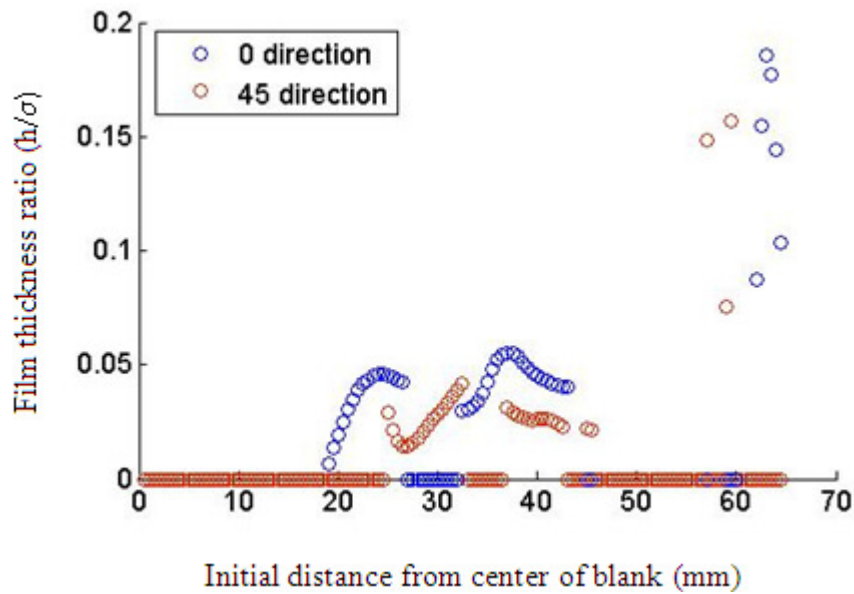
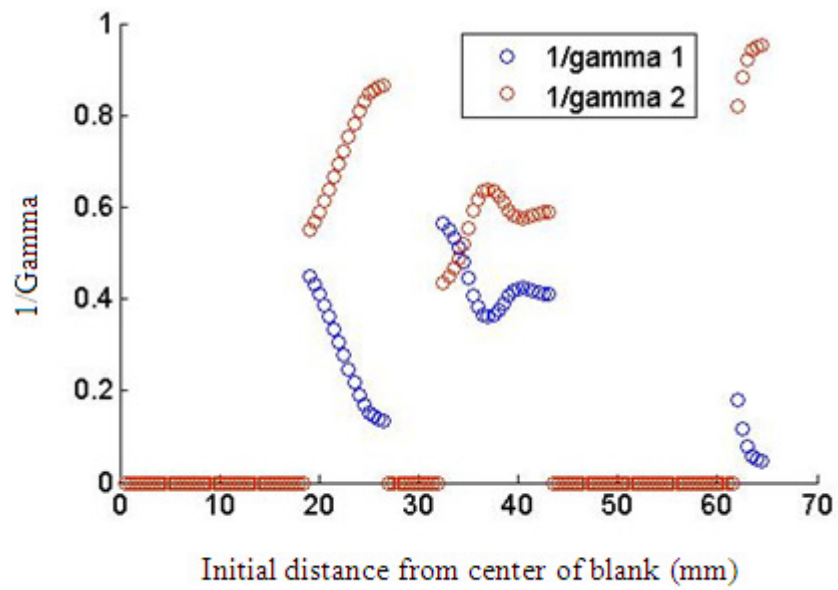
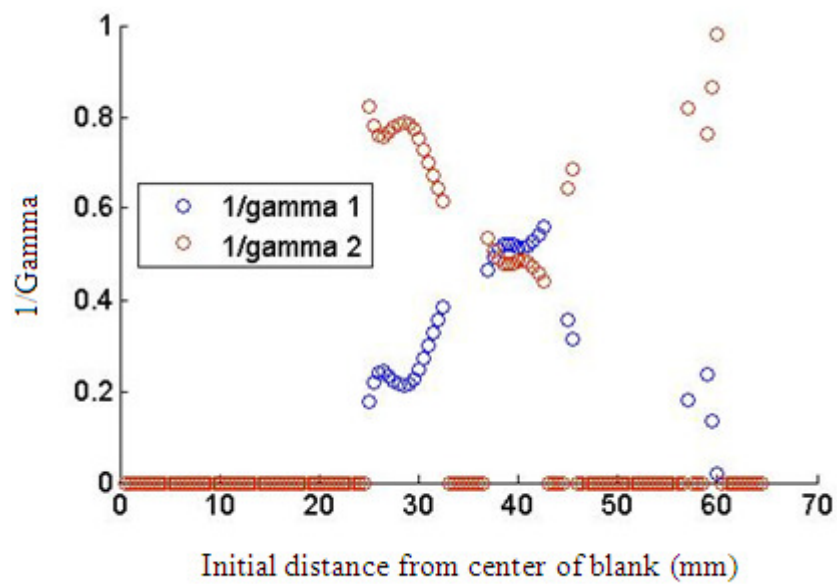


Figure 5.16 Film thickness ratio (h/σ) variation for square cup drawing at 18 mm cup depth ($f_{die}=0.05$, $f_{bh}=0.05$)

Scaling factor variations are shown in Figure 5.17, along 0° and 45° directions. $1/\gamma_1$ and $1/\gamma_2$ ratios are plotted in the figures for better comparison. At the punch radius contact, the load carried by the lubricant increases dramatically in the radial direction due to increasing values of the film thickness and relative velocity along 0° direction. Then, the load carried by the asperities decreases as expected. The trend is opposite along 45° direction where the load carried by the asperities increases at a high rate. The relative velocity is dominant since the load carried by the asperities increases at nodes with lower pressure, while the film thickness increases along 45° direction. At the die radius contact, the load carried by the lubricant almost has the same trend with the film thickness variation along 0° direction. The reason is that, the relative velocity and contact pressure show similar trends and compensate each other. The load carried by the asperities and lubricant are almost equal at the die radius contact along 45° direction. Then, the hydrodynamic force component decreases while asperities contribute more to load transfer. The driving force is the decreasing relative velocity at the end of the die radius contact. There are a few data points in the flange region, where the load is mostly transferred by the lubricant.



(a)



(b)

Figure 5.17 Scaling factor variation for square cup drawing (a) along 0° direction (b) along 45° direction at 18 mm cup depth ($f_{die}=0.05$, $f_{bh}=0.05$)

The coefficient of friction varies locally throughout the contact zones. A new combined friction model is introduced in Chapter 4, which is the combination of Wilson's friction model and Khonsari's friction model, in order to calculate the local friction coefficients. Friction models are based on the asperity contact and hydrodynamic flow respectively. Then, the combined model is applied to the outputs of square cup drawing simulation. Then, the local friction coefficient variations are shown in Figure 5.18, along 0° and 45° directions. In order to see the variation of the friction throughout the process, different cup depths are plotted, which are 6 mm, 12 mm and 18 mm.

Along 0° direction, the coefficient of friction variations are close to each other and trends are almost the same except the die radius contact. At the punch radius contact, the friction variation is the highest at 18 mm cup depth which varies between 0.06 and 0.03. The number of nodes which are in contact with the punch radius is very small at 6 mm cup depth. And the coefficient of friction varies between 0.04 and 0.05. At the die radius contact, 6 mm and 12 mm cup depths are almost identical while 18 mm cup depth is quite different. At 18 mm cup depth, the coefficient of friction has an increasing trend which reaches to 0.11 at the end of the radius contact. The friction coefficient has a decreasing trend at other depths.

Along 45° direction, the coefficient of friction variations are close to each other and trends are almost the same. At the punch radius contact, all cup depths show similar trends. The friction coefficient varies between 0.05 and 0.02 in which, the highest friction values are obtained at 18 mm cup depth and smallest at 6 mm cup depth. There is a shift between 12 mm and 18 mm cup depths, the number of nodes, which are in contact, are the same. At the die radius contact, friction coefficients differ in magnitude but, they all have an increasing tendency. The highest variation is observed at 12 mm cup depth where the friction coefficient increases from 0.06 up to 0.13. The friction coefficient variation is very small at 18 mm cup depth which varies around 0.09. Due to thickening in the flange region, the blank holder separates and only a small area contacts after the die radius contact. The results are non-uniform and do not tell much about the characteristics in the flange region.

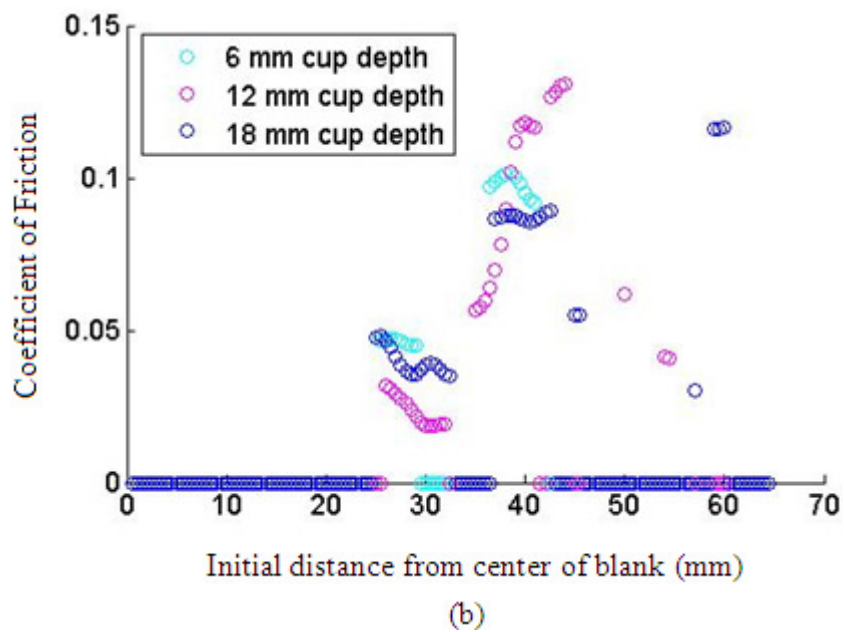
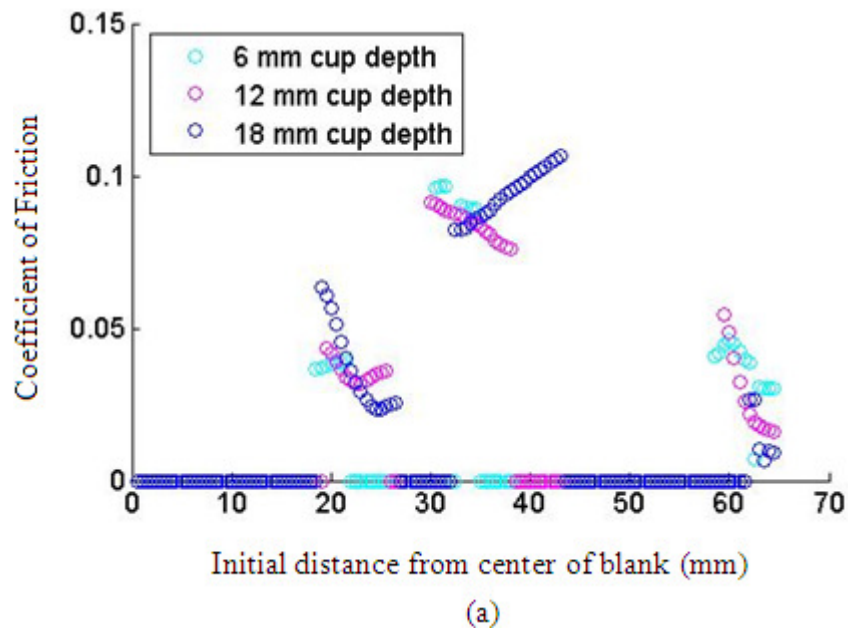


Figure 5.18 Variation of local friction coefficient for square cup drawing (a) along 0° direction (b) along 45° direction at cup depths of 6 mm, 12 mm and 18 mm ($f_{die}=0.05$, $f_{bh}=0.05$)

In the flange region, the number of nodes, which are in contact with the blank holder, is close to each other at 6 mm and 12 mm cup depths along 0° direction. The trends and magnitudes of friction coefficients are almost the same although there is a little difference through the end of flange. Along 45° direction, there are a few nodes in contact due to more thickening along 0° direction.

CHAPTER 6

PARAMETERS AFFECTING DEEP DRAWING PROCESS

In this chapter, after running a large number of simulations with different parameters, the effects of the parameters on the drawing process are investigated. Since the number of parameters are too large, only the most important and significant parameters are considered. In simulations, only one parameter changed and others are kept constant in order to see the effect on deep drawing.

6.1 Deep Drawing Parameters

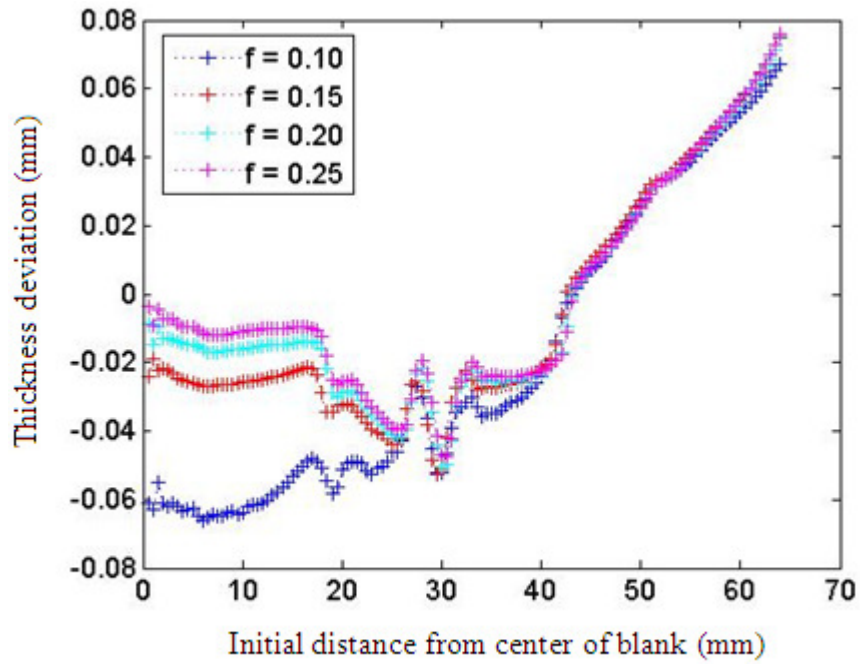
After a number of runs, optimum parameters are obtained for two types of deep drawing process with specified cup depths. The parameters are changed incrementally and differences are observed in plots. The parameters and their influences are different for square cup drawing and cylindrical cup drawing. Thickness variations are larger and deformations are more critical in square cup drawing. Therefore, parameters must be handled very carefully in square cup drawing. Unless otherwise stated; static and dynamic friction coefficients are taken as 0.15 at the punch contact, 0.05 at the blank holder and die contacts. Some of the major parameters and their effects are summarized as the following:

6.1.1 The Effect of Coefficient of Friction on Deep Drawing

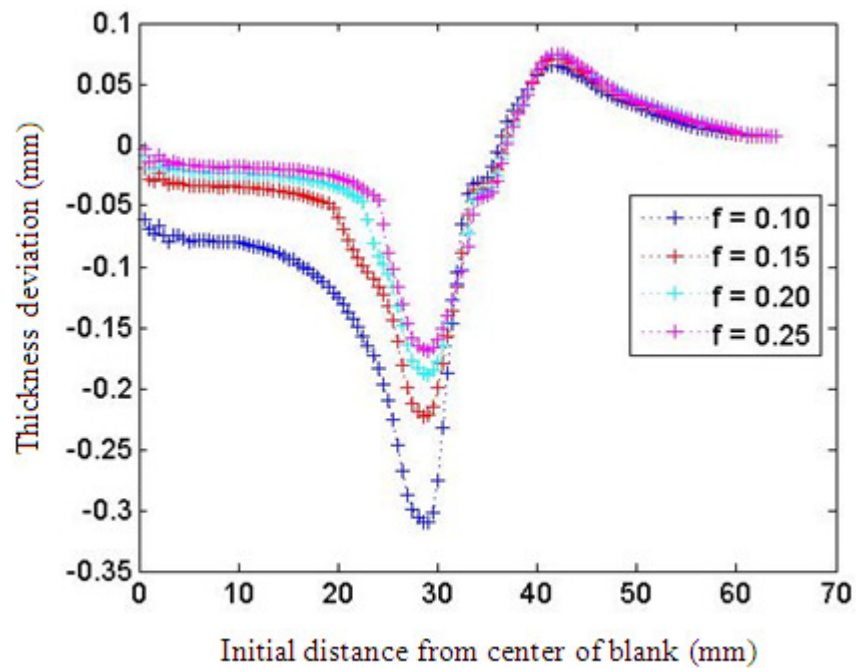
Friction at Punch Interface: The coefficient of friction at the punch and blank interface is the determining parameter for the thickness variation and consequently drawability of the blank. Changing the friction coefficient changes the thickness of the blank significantly, especially in the punch radius contact. The effects of the friction coefficient on the blank thickness variation are shown in Figure 6.1 for square cup drawing at 0° and 45° directions. Four different friction coefficients are simulated changing from 0.10 to 0.25.

Along 0° direction; it is seen that, there is thickness reduction at nodes within 19 mm, which are in the punch nose region. Then, the thickness reduction increases in the radial direction until the punch radius contact ends about 26 mm. It is seen that, there is excessive thinning of the blank, at the wall of the blank, due to stretching of the blank. The minimum thickness is observed in the wall and this is the most critical section along 0° direction. The thickness difference is not significant at high friction coefficients and thickness deviations are close to each other. At the lowest friction coefficient, the thickness is reduced dramatically, which is more than 3 times the other friction coefficients. At the die radius contact, the effect of the friction on the thickness variation is reduced but, trends of the curves are similar. The rest of the blank is not affected significantly from the changes in the friction coefficient between the punch and blank. The thickness deviation starts to decrease at the beginning of the die radius contact about 30 mm. There is thickening of the blank in the flange region, which continues until the end of the blank. As a result, friction coefficient is not a parameter that must be minimized instead; it is an important tool that is used to control material flow and deformation.

Along 45° direction, the thickness reduction is more critical than 0° direction. The thickness decreases more and more in the radial direction. Thickness values do not vary significantly at nodes within 25 mm, which are in the punch nose region except for friction coefficient of 0.1. Thickness reduction rate increases dramatically at the beginning of the punch radius. The minimum thickness is observed at the end of the



(a)



(b)

Figure 6.1 Blank thickness deviations at different punch surface friction coefficients for square cup drawing (a) along 0° direction (b) along 45° direction at 18 mm cup depth ($f_{dic}=0.05$, $f_{bh}=0.05$)

punch radius contact about 29 mm. As the friction coefficient decreases, the minimum drops to lower values due to scraping of the blank by the punch. Then, the thickness starts to increase after the end of the punch radius contact. Thickness values are larger than the original thickness in the whole flange region. Unlike 0° direction, after a rise in the flange region, the thickness variation changes its trend and decreases until the end of the blank. The maximum thickening is observed at the end of the die radius about 42 mm from the center.

The effects of the friction coefficient on the blank thickness variation are shown in Figure 6.2 for cylindrical cup drawing. Four different friction coefficients are simulated changing from 0.10 to 0.25. It is seen that, the friction coefficient between the blank holder and punch has crucial importance in the blank thickness. As the friction coefficient decreases, the thickness reduction increases at the nodes which are in contact with the punch. The rest of the blank, which is in contact with the die, is not significantly affected since the curves are similar for different coefficients. The results of 0.20 and 0.25 coefficients are close to each other and deviations are small. The minimum thickness for high friction coefficients are observed at the end of the punch radius contact about 24 mm from center. The minimum thickness for friction coefficient of 0.1 is observed close to the center of the punch radius contact. There is less stretching of the blank because of high friction at the interface and as a result, thickness reduction is smaller. As the friction coefficient decreases, it becomes easy to stretch the blank material under the punch and the thickness reduction is lower in this region. It is important to note that, the thickness is not affected significantly as lower friction coefficients from transition to the punch radius region at high friction coefficients.

The effects of the friction coefficient on the punch force variation are shown in Figure 6.3 for square cup drawing. Four different friction coefficients are simulated changing from 0.10 to 0.25. It is seen that, the punch force and cup depth are proportional and curves are almost linear up to 14 mm cup depth. All the curves in the plot are almost identical and there is little difference after 16 mm depth. The punch force becomes nearly constant around 51 kN at 18 mm cup depth.

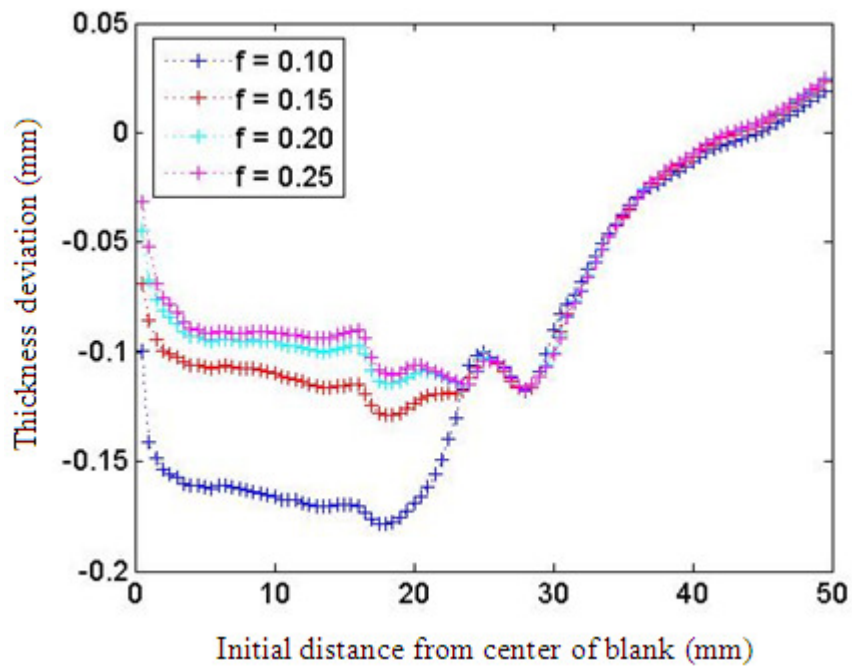


Figure 6.2 Blank thickness deviations at different punch surface friction coefficients for cylindrical cup drawing at 18 mm cup depth ($f_{die}=0.05$, $f_{bh}=0.05$)

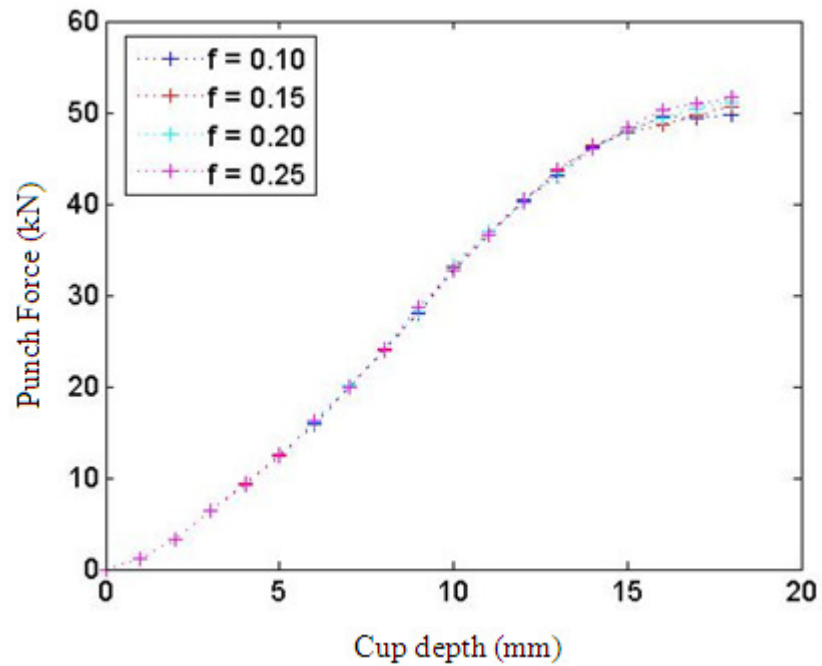


Figure 6.3 Punch force variations at different punch surface friction coefficients for square cup drawing ($f_{die}=0.05$, $f_{bh}=0.05$)

The effects of the friction coefficient on the punch force variation are shown in Figure 6.4 for cylindrical cup drawing. Four different friction coefficients are simulated changing from 0.10 to 0.25. It is seen that, changing the friction coefficient does not affect the punch force significantly. All the curves are almost identical. They all reach 26 kN at 18 mm cup depth. It is concluded that, the friction has almost no effect on the punch force magnitude and variation.

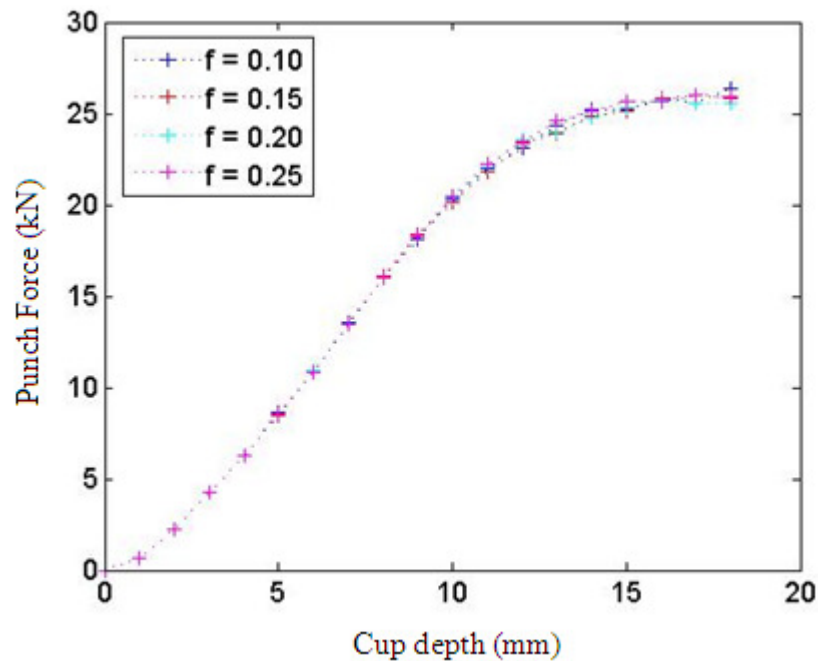
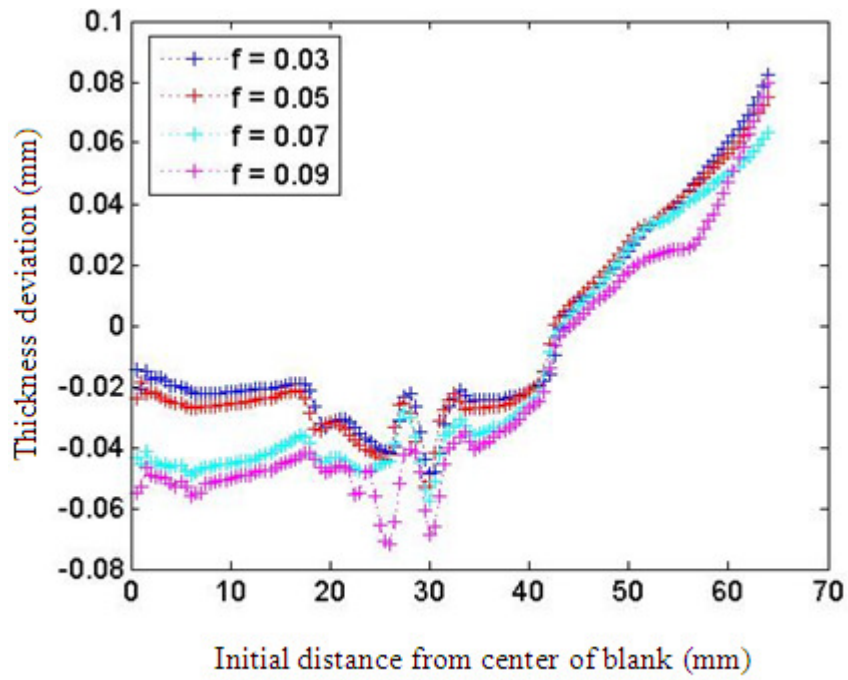
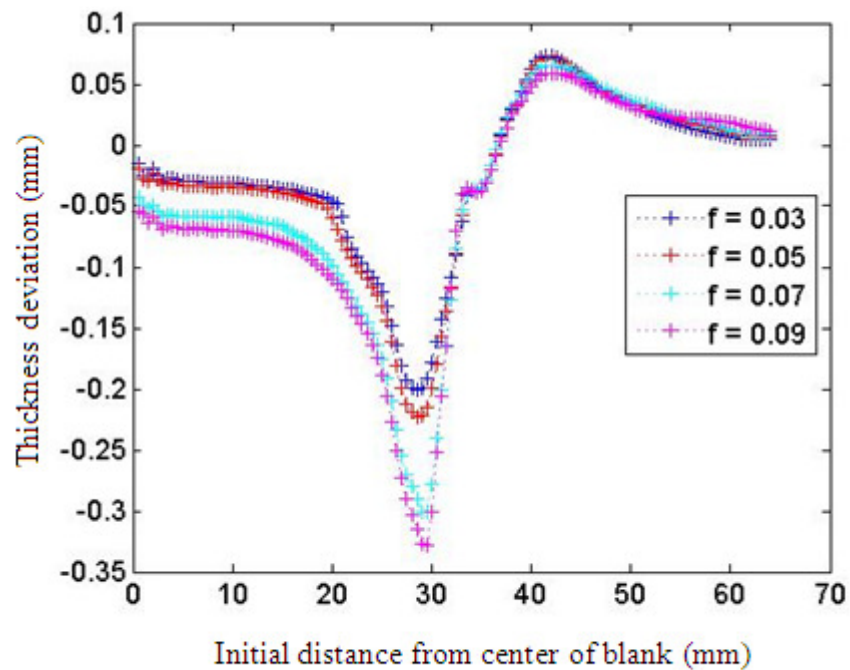


Figure 6.4 Punch force variations at different punch surface friction coefficients for cylindrical cup drawing ($f_{die}=0.05$, $f_{bh}=0.05$)

Friction at Blank Holder & Die Interfaces: The coefficient of friction at the tooling and blank interface is one of the major parameters which affects sliding of the blank in the flange region. The effects of the friction coefficient on the blank thickness variation are shown in Figure 6.5 for square cup drawing at 0° and 45°



(a)



(b)

Figure 6.5 Blank thickness deviations at different blank holder and die interface friction coefficients for square cup drawing (a) along 0° direction (b) along 45° direction at 18 mm cup depth ($f_p=0.15$)

directions. Four different friction coefficients are simulated changing from 0.03 to 0.09. Along 0° direction, the thickness reduction is smaller for lower friction coefficients of 0.03 and 0.05. Thickness reductions at the nodes, which are in the punch nose region, are smaller than the radius contact for lower friction coefficients, while the thickness is almost constant at higher coefficients. Although the increments are same, the difference is high between the coefficients of 0.05 and 0.07. There is a sudden and sharp decrease for the coefficient of 0.09 at the beginning of the punch radius about 25 mm from center which is not observed for other friction coefficients.

All the curves have similar trends and magnitudes, after the wall, except for coefficient of 0.09. Excessive deformations in the punch contact area and non-uniformity in the flange region means that 0.09 is not suitable for square cup drawing with the given parameters. There is thickening of the blank in the flange region which increases linearly until the end of the blank. Along 45° direction, thickness variations can be coupled together because, the trends and magnitudes of the curves are similar two by two. Curves obtained for lower friction coefficients of 0.03 and 0.05 are almost identical also; curves obtained for high friction coefficients of 0.07 and 0.09 are similar to each other. The difference between coefficients of 0.05 and 0.07 is high similar to 0° direction. The highest thickness reduction is observed at the end of the punch radius contact about 29 mm from center, which is 1.5 times larger for higher friction coefficients of 0.07 and 0.09. There is thickening of the blank in the flange region but, the thickness drops after the end of the die radius contact while it is still larger than the original thickness.

The effects of the friction coefficient on the punch force variation are shown in Figure 6.6 for cylindrical cup drawing. Four different friction coefficients are simulated changing between 0.03 and 0.09. The friction domain covers restricted movement of the blank at high friction in the flange region. It is seen that, the thickness reduction increases at nodes, which are in contact with the punch, with higher friction at the tooling interface. If the value is too high, excessive yielding (failure) of the blank is possible which is observed for the coefficient of 0.09. There is a sudden and catastrophic thickness reduction at two nodes, which means failure of the blank about 22 mm from center. Therefore, failure of the blank has the tendency

to occur at the punch radius contact region; in this case, it is closer to the end of the radius contact. Trends of all curves are similar after the punch contact. The thickness increases and the deviations become positive in the flange region which means thickening of the blank.

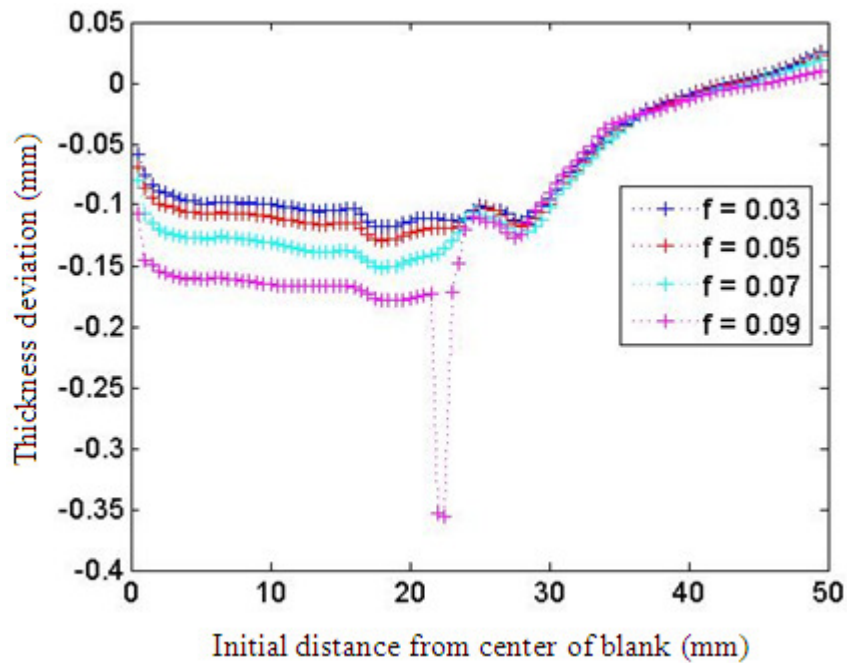


Figure 6.6 Blank thickness deviations at different blank holder and die interface friction coefficients for cylindrical cup drawing at 18 mm cup depth ($f_p=0.15$)

The effects of the friction coefficient on the punch force variation are shown in Figure 6.7 for square cup drawing. Four different friction coefficients are simulated changing from 0.03 to 0.09. It is seen that, the punch force and cup depth are proportional up to 12 mm cup depth. Then, the effect of the friction change becomes significant and difference between punch forces increases. As the friction coefficient increases, the punch force increases but, the rate decreases after 14 mm depth.

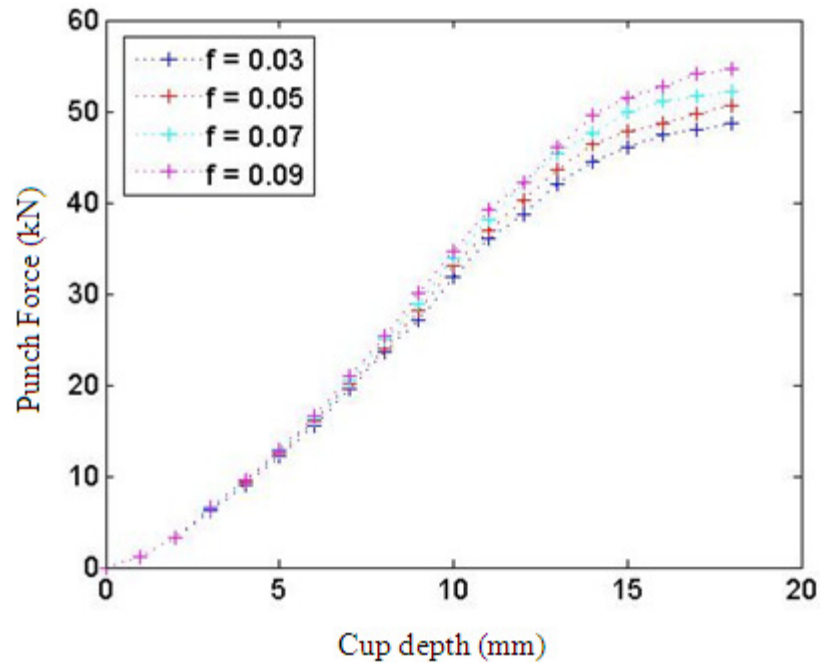


Figure 6.7 Punch force variations at different blank holder and die interface friction coefficients for square cup drawing ($f_p=0.15$)

The effects of the friction coefficient on the punch force variation are shown in Figure 6.8 for cylindrical cup drawing. Four different friction coefficients are simulated changing from 0.03 to 0.09. It is seen that, the punch force and cup depth are proportional and curves are almost identical up to 12 mm cup depth. Then, the effect of the friction change becomes significant and difference between punch forces increases. As the friction coefficient increases, the punch force increases especially, after 12 mm cup depth. It was noted before that there is failure of the blank for friction coefficient of 0.09 after 16 mm cup depth.

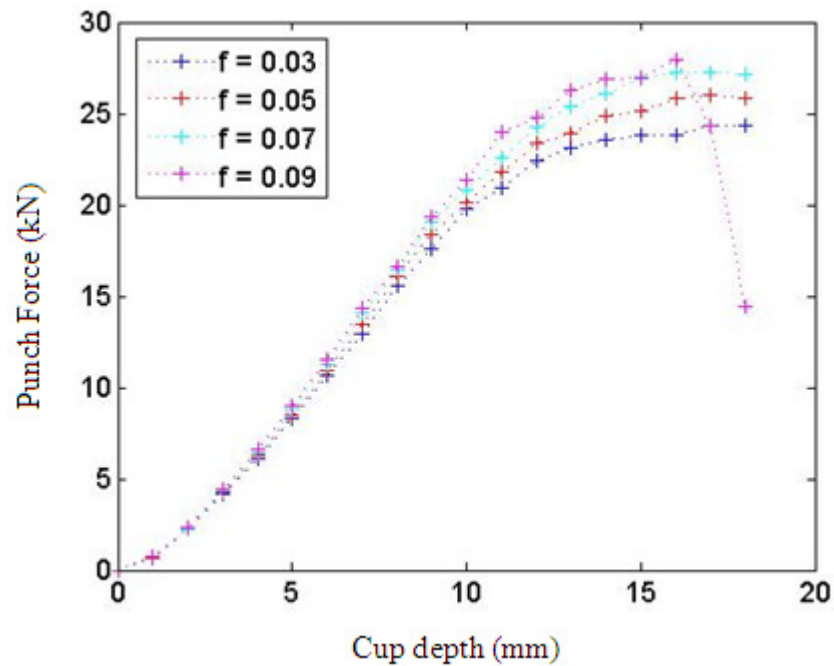
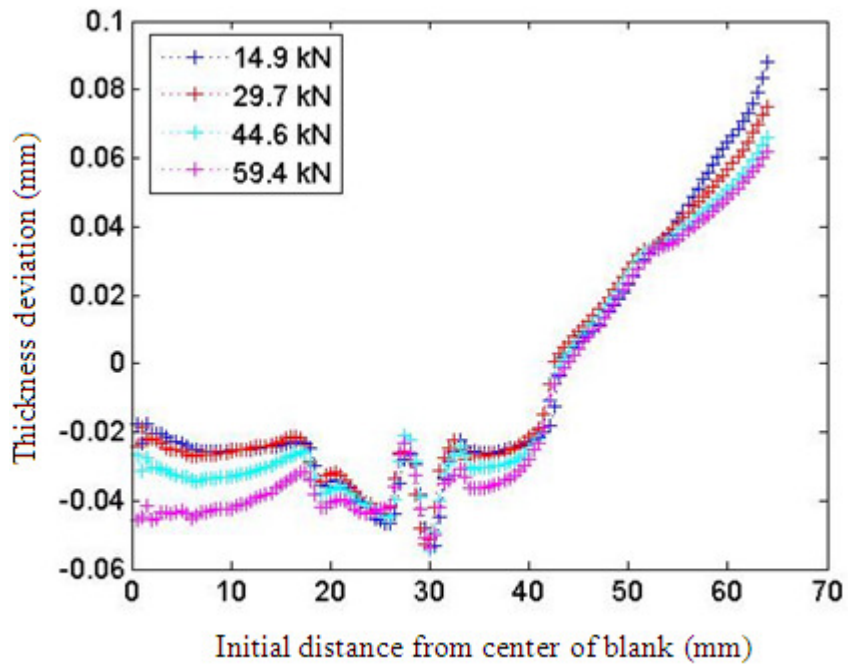


Figure 6.8 Punch force variations at different blank holder and die interface friction coefficients for cylindrical cup drawing ($f_p=0.15$)

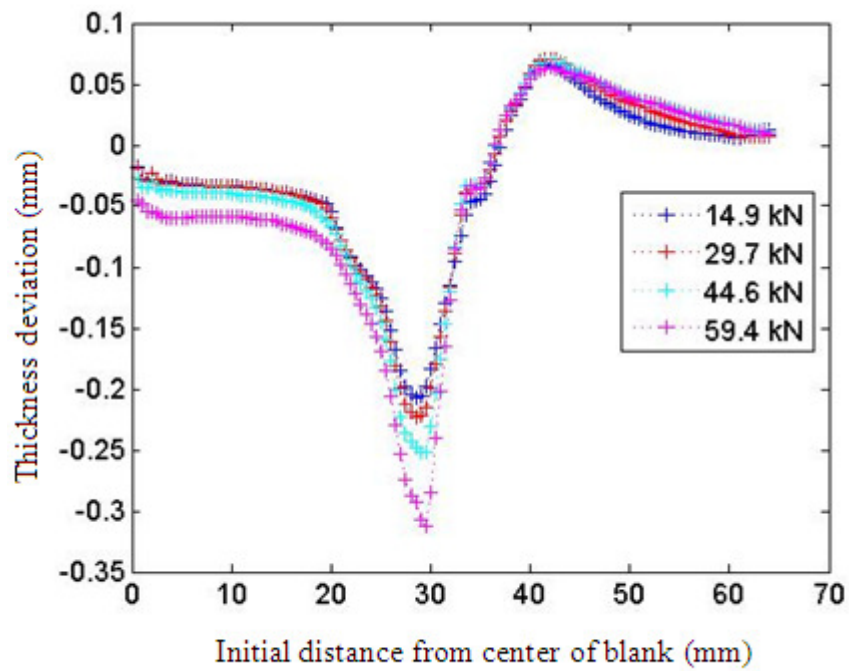
6.1.2 The Effect of Clamping Force on Deep Drawing

The clamping force is another major parameter in deep drawing. Its value must be high enough to avoid wrinkling in the flange region but, small enough to let the material slide between the die and blank holder. If sliding of the blank is restricted then, there will be excessive thinning. The reason is that, material is not fed into the deformation zone. Its magnitude is highly dependent on the friction at the tooling and blank interface in the flange region. Therefore, both need to be adjusted accordingly. In this thesis, for simplicity, clamping forces are kept constant during the whole process.

The effects of the clamping force on thickness variation are shown in Figure 6.9 for square cup drawing along 0° and 45° directions. Four different clamping forces are simulated changing from 14.9 kN to 59.4 kN. Along 0° direction, the thickness



(a)



(b)

Figure 6.9 Blank thickness deviations at different clamping forces for square cup drawing (a) along 0° direction (b) along 45° direction at 18 mm cup depth ($f_p=0.15$, $f_{die}=0.05$, $f_{bh}=0.05$)

decreases as the clamping force increases at the nodes within 19 mm, which are in the punch nose region. The magnitude of changes is higher at high blank forces. Thickness changes in the blank are not significant in the punch radius contact. The minimum thickness is observed at the beginning of the die radius contact which is almost same for all clamping forces. Then, the thickness increases in the wall of the blank. The minimum thickness is observed at the beginning of the die radius contact about 30 mm from the center. Then, the thinning effect diminishes in the die radius contact and flange region. There is thickening of the blank in the flange region. Trends are similar for all clamping forces but, the highest thickness is observed by using lower forces at the end of the flange. As a result, the clamping force is more effective at the punch contact along 0° direction.

Along 45° direction, there is thickness reduction at nodes within 25 mm, which are in the punch nose region. The thickness decreases more and more in the radial direction. The thickness reduction rate starts to increase dramatically at the beginning of the punch radius contact. The minimum is observed at the end of the punch radius contact about 29 mm. Therefore, the most critical and determining section of the blank is observed at the transition to the wall of the drawn part. There is excessive thinning at the highest clamping force of 59.4 kN, which may cause failure of the blank. Then, thicknesses are close to each other for the rest of the blank. As a result, changing the clamping force is more effective in the punch radius contact along 45° direction which is similar to the characteristics of 0° direction.

The effects of the clamping force on the thickness variation are shown in Figure 6.10 for cylindrical cup drawing. Four different clamping forces are simulated changing from 11.5 kN to 33.2 kN. It is seen that, increasing the clamping force increases the deviation from original blank thickness. At lower forces, the deviation is not high and very close to each other. More thickness change is observed at high clamping forces. The thickness reduction is higher at nodes which are in contact with the punch. The minimum thickness is observed at the beginning of the punch radius contact about 19 mm from center. The rest of the blank, which is in contact with the die, is not affected significantly from the changes in the clamping force. All the

curves in the figure show the same trend, their maxima locations are similar and they are located at the same radial distances.

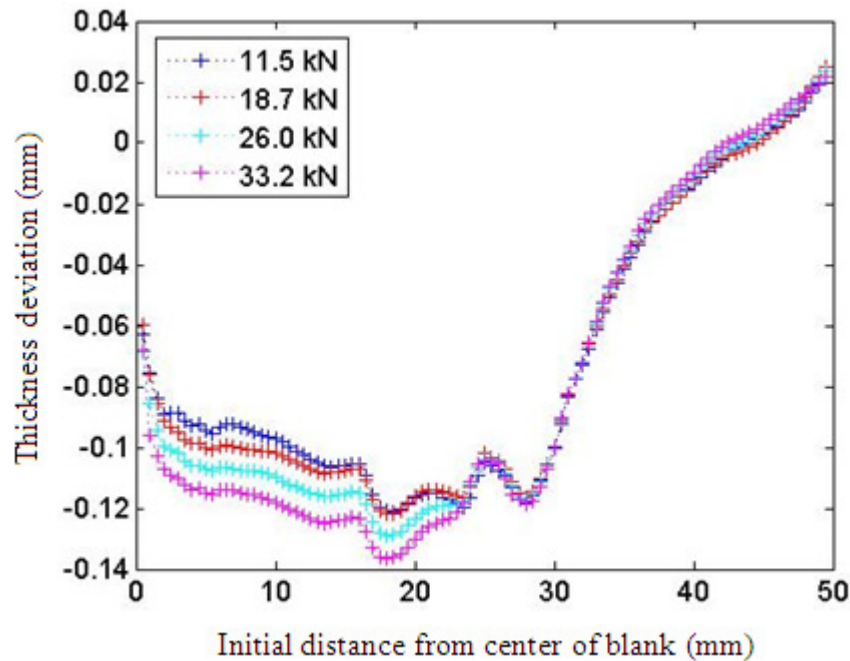


Figure 6.10 Blank thickness deviations at different clamping forces for cylindrical cup drawing at 18 mm cup depth ($f_p=0.15$, $f_{die}=0.05$, $f_{bh}=0.05$)

The effects of the clamping force on the punch force variation are shown in Figure 6.11 for square cup drawing. Four different clamping forces are simulated changing from 14.9 kN to 59.4 kN. The punch force variation shows similar trends with cylindrical cup drawing. Up to 13 mm cup depth, curves are linear and the punch force is proportional to the clamping force. Then, the rates decrease after 13 mm depth. Differences in the punch force become more significant at higher depths. Increasing the clamping force causes an increase in the punch force.

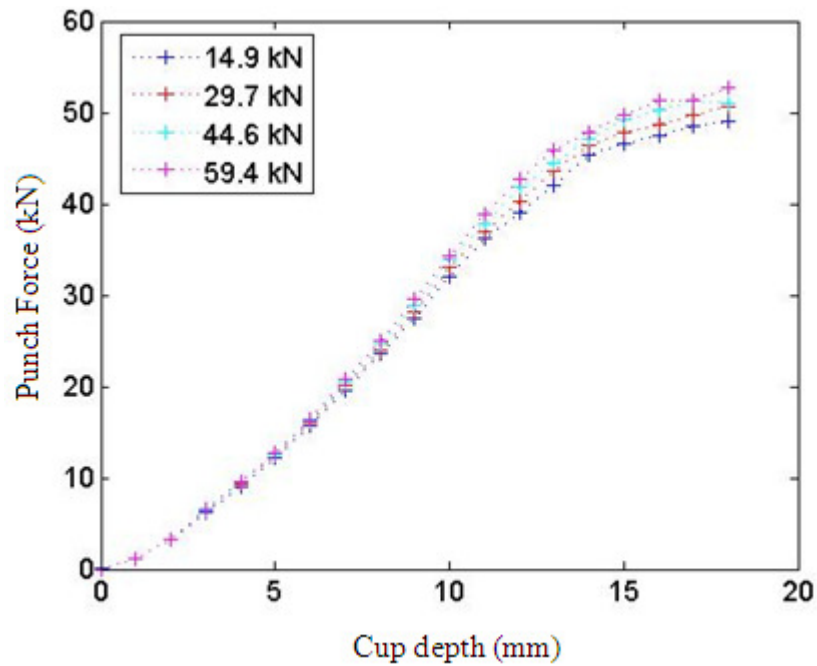


Figure 6.11 Punch force variations at different clamping forces for square cup drawing ($f_p=0.15$, $f_{die}=0.05$, $f_{bh}=0.05$)

The effects of the clamping force on the punch force are shown in Figure 6.12 for cylindrical cup drawing. Four different clamping forces are simulated changing from 11.5 kN to 33.2 kN. Up to 12 mm cup depth, punch forces are almost proportional to the cup depth. Then, the rates decrease after 12 mm depth. Differences in the punch force become more significant at higher depths. Increasing the clamping force causes an increase in the punch force.

The effects of the clamping force on the local friction coefficient variation are shown in Figure 6.13 for square cup drawing. Four different clamping forces are simulated changing from 14.9 kN to 59.4 kN. At the punch radius contact, friction coefficients have different trends at 18 mm cup depth varying between 0.03 and 0.05. At the die radius contact, friction coefficients have similar trends and differences are more significant. The highest friction coefficient is obtained at clamping force of 14.9 kN and lowest at 59.4 kN. Friction coefficient values are very close to each other at

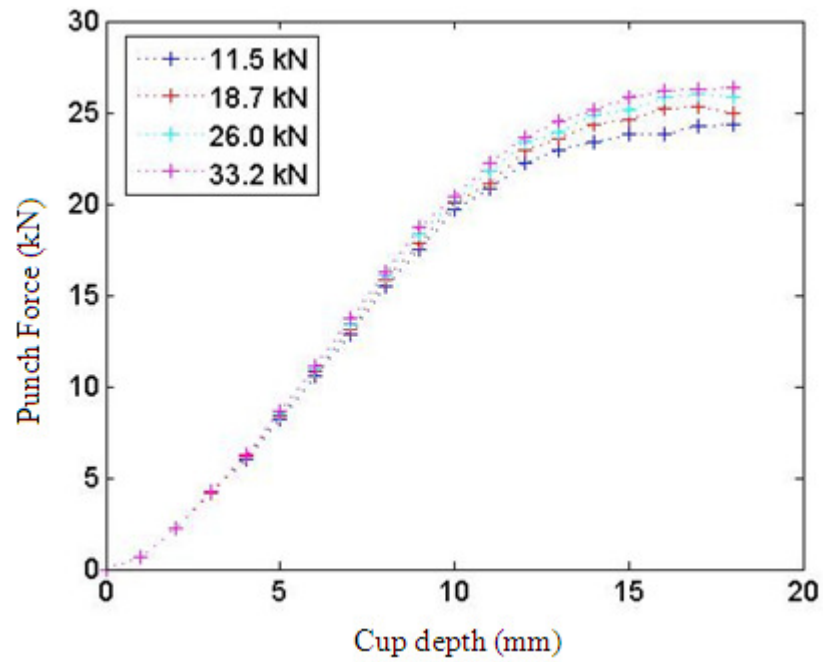


Figure 6.12 Punch force variations at different clamping forces for cylindrical cup drawing ($f_p=0.15$, $f_{die}=0.05$, $f_{bh}=0.05$)

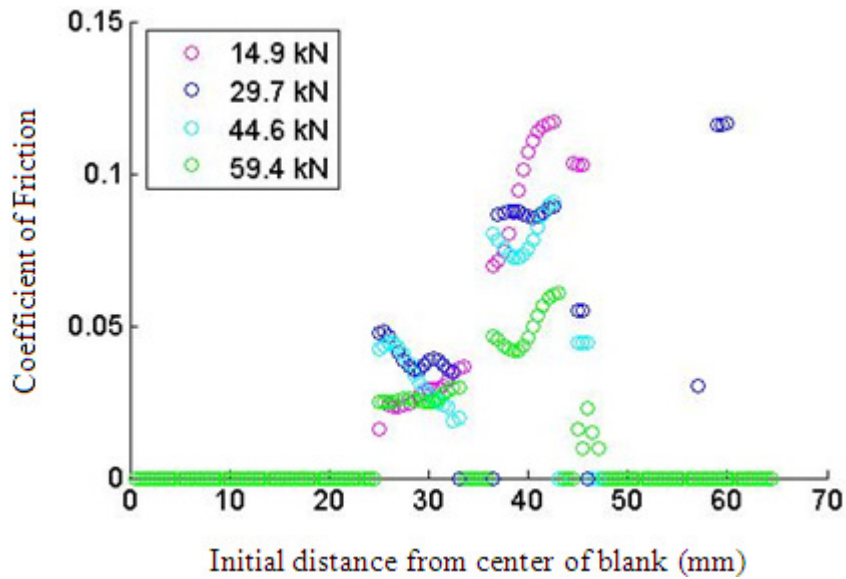


Figure 6.13 Local friction coefficient variations at different clamping forces for square cup drawing along 45° direction ($f_{die}=0.05$, $f_{bh}=0.05$)

clamping forces of 29.7 kN and 44.6 kN but, the trends are a little bit different. Therefore, increasing the clamping force does not affect the friction coefficient variation at the punch radius contact as much as the die radius contact. Due to thickening of the blank in the flange region, the blank holder is separated and only a small area is in contact. At the start of the flange region, a couple of nodes are in contact about 45 mm as shown in figure. Friction coefficients decrease as the clamping force decreases in this contact area. It is concluded that, the clamping force is quite effective in the friction coefficient calculations for square cup drawing.

The effects of the clamping force on the local friction coefficient variation are shown in Figure 6.14 for cylindrical cup drawing. Four different clamping forces are simulated changing from 11.5 kN to 33.2 kN. The number of nodes, which are in contact with the punch radius, is almost same for all different clamping forces. At the punch radius contact, friction coefficients do not differ significantly from each other as seen from the figure and the values vary between 0.10 and 0.03. At the die radius contact, friction coefficient variations are a little bit more significant. The highest

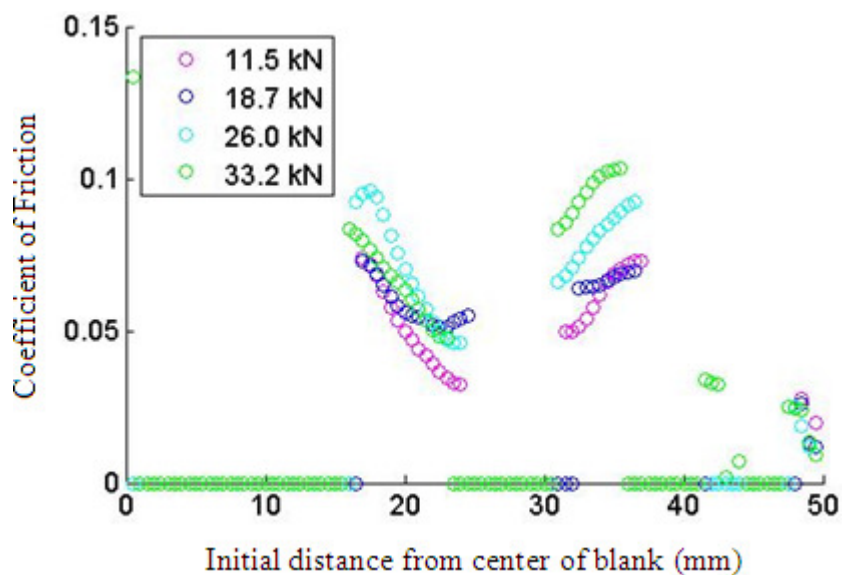


Figure 6.14 Local friction coefficient variations at different clamping forces for cylindrical cup drawing ($f_{die}=0.05$, $f_{bh}=0.05$)

friction coefficient is obtained at clamping force of 26.0 kN at the punch radius contact and clamping force of 33.2 kN at the die radius contact. Due to thickening, a small contact area occurs at the outer flange and a small portion at the beginning of the flange. Contact pressure values are so high that the friction coefficients are very low, which are smaller than 0.03. It is concluded that, changing the clamping force does not affect the friction coefficients significantly at the punch radius contact.

6.2 Discussion of Results

Cylindrical and square cup drawing operations are simulated at different clamping forces and friction coefficients at the tooling interface. The effects of these changes on the thickness deviation and punch force are observed in the plots. Then, the effects of these parameters can be summarized as the following.

Changing the coefficient of friction at the punch contact has a significant effect on the thickness deviation at nodes which are contacting the punch radius and at the nodes which are under the punch nose. The rest of the blank is not affected by the change although; a small area close to the end of die radius is slightly affected. This effect of friction change is the highest at the center of the blank which is followed by a decrease until the end of the radius contact. It is a surprising fact that the punch force is not affected by the change of friction coefficient in both deep drawing operations. It is important to note that, friction is not a parameter that must be minimized as it was mentioned above. Low friction coefficients at the punch contact, result in higher thickness reductions, especially in the corner of the square cup.

Changing the coefficient of friction at the blank holder and die contacts has a similar influence area similar to friction coefficient change at the punch contact. Only the nodes between the center of the blank and wall are affected. Even though friction coefficient increments are smaller, the effects on thickness deviations are more significant. As opposed to the friction coefficient change at the punch contact, lower

friction coefficients result in lower thickness deviations. Therefore, friction coefficients must be minimized and controlled very carefully in the flange region. Especially, cylindrical cup drawing is more sensitive to changes and more likely to fail. The punch force is also affected by the friction change in both drawing types. As the friction coefficient increases, higher punch forces are required to move the punch at a constant velocity.

The influence area does not change in case of applying different clamping forces. Therefore, the same effects are observed with changing the friction at the die & blank holder interfaces. Using higher clamping forces, increases the friction in the flange region directly. The friction coefficient variation in square cup drawing is more sensitive to the changes in clamping force especially, in the die radius contact. It is interesting to note that, increasing clamping force does not affect thickening of the blank in the flange region significantly.

CHAPTER 7

CONCLUSIONS AND RECOMMENDATIONS

7.1 Conclusions

A single friction model is not sufficient to cover wide range of internal and external conditions existing on the contact between bodies. All the friction models developed have their own pitfalls and limitations. Therefore, friction models can be combined to increase accuracy, enlarge domain and reduce computational time. In this study, Wilson's and Khonsari's friction models are combined for this purpose.

The effect of coefficient of friction on deep drawing process parameters are investigated for two different types of deep drawing which are cylindrical and square cup drawing. For $\varnothing 48$ mm cylindrical cup drawing, a steel blank with thickness of 0.66 mm and diameter of 100 mm was simulated up to 18 mm cup depth in single stage. For 50.5×50.5 mm square cup drawing, a steel blank with thickness of 0.8 mm and diameter of 130 mm was simulated up to 18 mm cup depth in single stage. Simulations were performed in LS-Dyna at a constant punch velocity of 10 mm/s until the final depth is reached. Both cup drawing operations are classified as shallow drawing since the final cup depths are smaller than the minimum dimension of the die openings. Then, the combined friction model developed in MATLAB is applied to the outputs of the simulations and friction coefficient variations were obtained at the critical sections. Then, the local coefficients of friction along the radial directions were plotted.

The results obtained in the previous chapters show that the effect of friction on the deep drawing process cannot be disregarded and the following conclusions are made:

- There are critical regions observed during the process, where friction variations are the determining factor for the quality of the deep drawing products.
- It was observed that the square cup drawing is more sensitive to changes in the friction coefficient, especially at the corners of the drawn product.
- Combined surface roughness is the determining parameter for the range of film thickness ratio where Khonsari's model can be applied. A film thickness ratio of 0.035 is selected as criteria for $\sigma_s = 0.15 \mu\text{m}$. After comparing the results of Wilson's and Khonsari's friction models, it is determined that Khonsari's friction model gives more accurate results in the BL and some portion of the ML regime (close to the BL regime) while Wilson's friction model gives more accurate results for the rest of the regimes. It is concluded that Khonsari's model must be applied at the BL regime and for the film thickness ratios lower than 0.035 while Wilson's friction model must be applied for higher ratios.
- It was observed that neglecting the squeeze force of the lubricant film in Khonsari's friction model does not affect the calculations at the BL regime and some portion of the ML regime which is close to the BL regime. The reason is that the squeeze force is very small when the load is mostly transferred through the asperities.
- The punch force is not affected by the friction coefficient at the punch radius contact while friction at the bank holder and die interfaces are quite effective especially at higher cup depths.

7.2 Recommendations for Future Work

The friction model can be improved by considering the following features:

- Thermal effects should be included in the friction calculations due to variation of lubricant parameters at the contact regions.

- Wear and lubricant starvation effects should be included in the friction calculations since wear cannot be avoided and it is impossible to supply fully-flooded conditions at all contact areas throughout the drawing process.
- During deep drawing process, flattening of the asperities should be included in the friction models because, shape of the surface asperities changes throughout the process.

REFERENCES

- [1] Wilson WRD, Hsu TC, Huang XB. A realistic friction model for computer simulation of sheet metal forming processes. *ASME Journal of Engineering for Industry* 1995;117:202–9.
- [2] Westeneng JD. Modelling of contact and friction in deep drawing processes. Ph.D. Thesis. University of Twente. Enschede, 2001.
- [3] Emmens WC. Tribology of flat contacts and its application in deep drawing. PhD Thesis. University of Twente. Enschede, 1997.
- [4] Darendeliler H, Akkök M, Yücesoy CA. Effect of variable friction coefficient on sheet metal drawing. *Tribology International* 2002;35(2):97-104.
- [5] Kotwal CA, Bhushan B. (). Contact analysis of non-gaussian surfaces for minimum static and kinetic friction and wear. *Tribology Transactions* 1996;39:890-898.
- [6] Bhushan B. *Modern Tribology Handbook*. New York: CRC Press, 2001.
- [7] Schey JA. *Tribology in metalworking: friction, lubrication and wear*. ASM, Metals Park, 1983.
- [8] de Rooij MB. Tribological aspects of unlubricated deepdrawing processe. Ph.D. Thesis. University of Twente. Enschede, 1998.
- [9] Greenwood JA, Williamson JBP. Contact of nominally flat surfaces. *Proc R Soc London* 1966;295:300-319.
- [10] Greenwood JA, Tripp JH. Contact of two nominally flat rough surfaces. *Proc Inst Mech Eng* 1970;185:625-633.
- [11] Onions RA, Archard JF. The contact of surfaces having a random structure. *Journal of Physics D: Applied Physics* 1973;6(3):289-304.
- [12] Chang WR, Etsion I, Bogy DB. An elastic-plastic model for the contact of rough surfaces. *ASME Journal of Tribology* 1987;109:257-263.
- [13] Halling J, Arnell RD, Nuri KA. The elastic-plastic contact of rough surfaces and its relevance in the study of wear. *Proc Inst Mech Eng* 1988;202:269-274.
- [14] Liu G, Wang Q, Lin C. A survey of current models for simulating the contact between rough surfaces. *Tribology Transactions* 1999;42(3):581-591.
- [15] Webster MN, Sayles RS. Numerical model for the elastic frictionless contact of real rough surfaces. *Journal of Tribology* 1986;108(3):314-320.

- [16] Pullen J, Williamson JPB. On the plastic contact of rough surfaces. Proc. R. Soc. London, Series A 1972;327:159-173.
- [17] Sutcliffe MPF. Surface asperity deformation in metal forming processes. International Journal of Mechanical Sciences 1988;30(11):847-868.
- [18] Wilson WRD, Sheu S. Real area of contact and boundary friction in metal forming. International Journal of Mechanical Sciences 1988;30(7):475-489.
- [19] Kimura Y, Childs THC. Surface asperity deformation under bulk plastic straining conditions. International Journal of Mechanical Sciences 1999;41(3):283-307.
- [20] Pan P, Hamrock BJ. Simple Formulae for performance of parameters used in elastohydrodynamically lubricated line contacts. ASME Journal of Tribology 1989;112(2):26-304.
- [21] Patir N, Cheng HS. Average flow model for determining effects of three-dimensional roughness on partial hydrodynamic lubrication. ASME Journal of Lubrication Technology 1978;100(1):12-17.
- [22] Patir N, Cheng HS. Application of average flow model to lubrication between rough sliding surfaces. ASME Journal of Lubrication Technology 1979;101(2):220-230.
- [23] Tripp H. Surface roughness effects in hydrodynamic lubrication: the flow factor method. ASME Journal of Lubrication Technology 1983;105:459-65.
- [24] Hess DP, Soom A. Friction at a lubricated line contact operating at oscillating sliding velocities. Journal of Tribology 1990;112(1):147-152.
- [25] Polycarpou AA, Soom A. Two-dimensional models of boundary and mixed friction at a line contact. Journal of Tribology 1995;117(1):178-184.
- [26] Barus C. Isotherms, isopeistics and isometrics relative to viscosity. American Journal of Science 1893;45:87-96.
- [27] Gelinck ERM, Schipper DJ. Calculation of stribeck curves for line contacts. Tribology International 2000;33(3-4):175-181.
- [28] Lu X, Khonsari MM, Gelinck ERM. The stribeck curve: Experimental results and theoretical prediction. Journal of Tribology 2006;128(4):789-794.
- [29] Akbarzadeh S, Khonsari MM. Performance of spur gears considering surface roughness and shear thinning lubricant. Journal of Tribology 2008;130(2):1-8.
- [30] Zhai X, Needham G, Chang L. On the mechanism of multi-valued friction in unsteady sliding line contacts operating in the regime of mixed-film lubrication. Journal of Tribology 1997;119(1):149-155.

- [31] Dawson D, Higginson GR. Elastohydrodynamic lubrication. 2nd ed. Oxford: Pergamon Press, 1977.
- [32] Christensen H. Stochastic Models for Hydrodynamic Lubrication of Rough Surfaces. Proc Inst Mech Eng 1970;104(1):1013-1022.
- [33] Sojoudi H, Khonsari MM. On the modeling of quasi-steady and unsteady dynamic friction in sliding lubricated line contact. Journal of Tribology 2010;132(1):1-9.

APPENDIX A

RADIUS OF CURVATURE CALCULATION STEPS

The following steps are followed in calculations;

- 1) Mean, or average, of x and z coordinates are calculated separately by using 3 nodes. “mean()” command is used in calculations.
$$mx = \text{mean}(\text{ThriceX});$$
$$mz = \text{mean}(\text{ThriceZ});$$
- 2) The difference from the mean in x and z axes are calculated for the nodes.
$$X = \text{ThriceX} - mx;$$
$$Z = \text{ThriceZ} - mz;$$
- 3) Then, the variances are found by calculating the squares of the mean X and Z.
$$dx2 = \text{mean}(X.^2);$$
$$dz2 = \text{mean}(Z.^2);$$
- 4) Then, the following least mean squares problem is solved.
$$t = [X, Z] \setminus (X.^2 - dx2 + Z.^2 - dz2) / 2;$$
- 5) “t” is found as a 2 x 1 dimensional solution array. a0 and b0 are the first and second elements of the array.
$$a0 = t(1);$$
$$b0 = t(2);$$
- 6) Finally, equivalent radius of the center node “R1” is found from the following formula by substituting the previously calculated parameters.
$$R1(i,1) = \text{sqrt}(dx2 + dz2 + a0^2 + b0^2);$$

APPENDIX B

CALCULATION OF THE LOCAL VELOCITIES

At the flat contacts, the following equations are used to calculate the local average velocity, V , and local relative velocity, V_r :

$$V = (V_{x,node})/2 \quad (B.1)$$

$$V_r = V_{x,node} \quad (B.2)$$

At the punch radius contact, which is shown in Figure B.1, the following equations are used to calculate the local average velocity, V , and local relative velocity, V_r :

$$V = (V_{x,node} \times \cos \theta + (V_{z,node} + V_{z,punch}) \times \sin \theta)/2 \quad (B.3)$$

$$V_r = V_{x,node} \times \cos \theta + (V_{z,node} - V_{z,punch}) \times \sin \theta \quad (B.4)$$

where $\sin \theta$ and $\cos \theta$ are the following:

$$\sin \theta = \frac{d_2 - d_1}{R + (t/2)} \quad (B.5)$$

$$\cos \theta = \frac{R - d_3}{R + (t/2)} \quad (B.6)$$

where t is the deformed thickness of the blank.

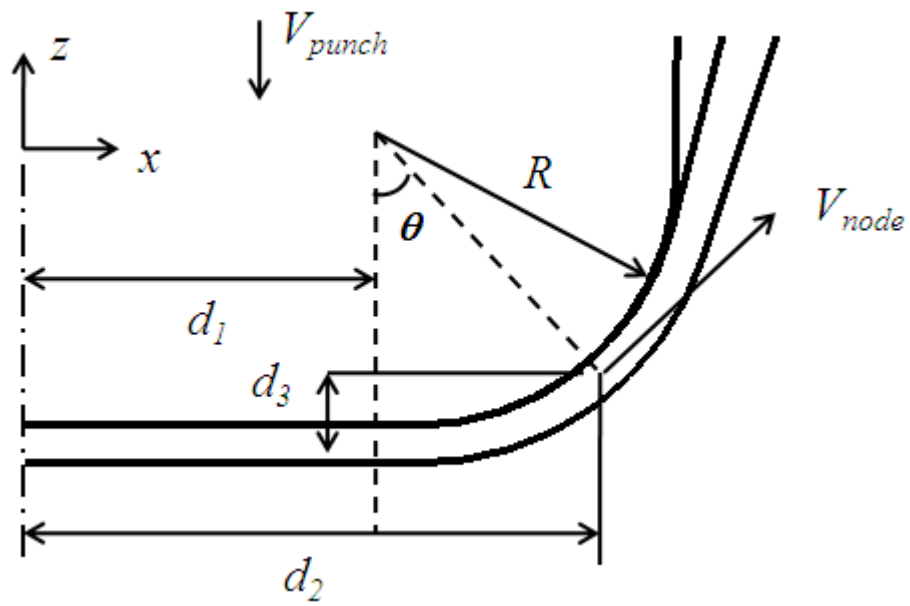


Figure B.1 Local velocities at the punch radius contact

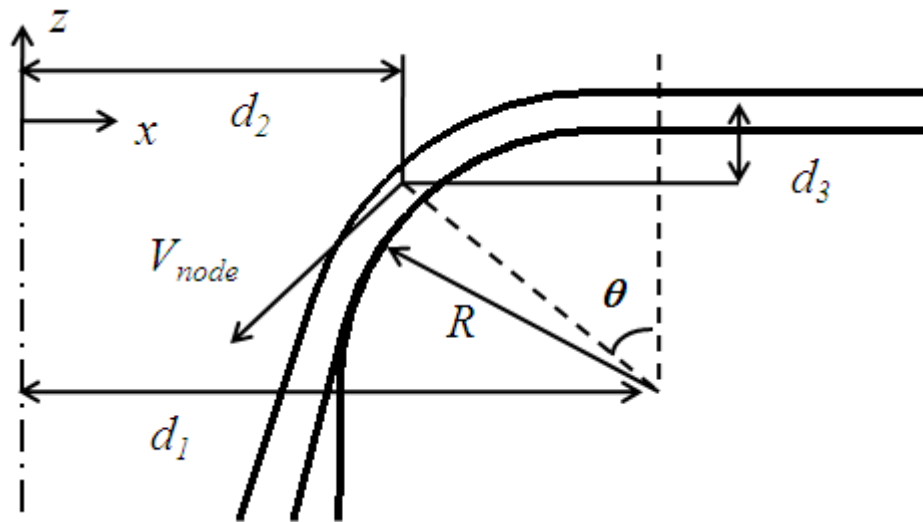


Figure B.2 Local velocities at the die radius contact

At the die radius contact, which is shown in Figure B.2, the following equations are used to calculate the local average velocity, V , and local relative velocity, V_r :

$$V = (V_{x,node} \times \cos \theta + V_{z,node} \times \sin \theta) / 2 \quad (\text{B.7})$$

$$V_r = V_{x,node} \times \cos \theta + V_{z,node} \times \sin \theta \quad (\text{B.8})$$

where $\sin \theta$ and $\cos \theta$ are the following:

$$\sin \theta = \frac{d_1 - d_2}{R + (t/2)} \quad (\text{B.9})$$

$$\cos \theta = \frac{R + (t/2) - d_3}{R + (t/2)} \quad (\text{B.10})$$

where t is the deformed thickness of the blank.

APPENDIX C

SAMPLE COEFFICIENT OF FRICTION INPUT FOR LS-DYNA

In order to input variable friction data to LS-Dyna, curves in Figure C.1 are input in a tabulated format for cylindrical cup drawing which are obtained for the parameters given in Table 4.3. 7 different pressure curves are obtained changing between 20 MPa and 80 MPa. The data are obtained by applying the Khonsari's friction model to the results obtained by simulations with constant coefficient of frictions.

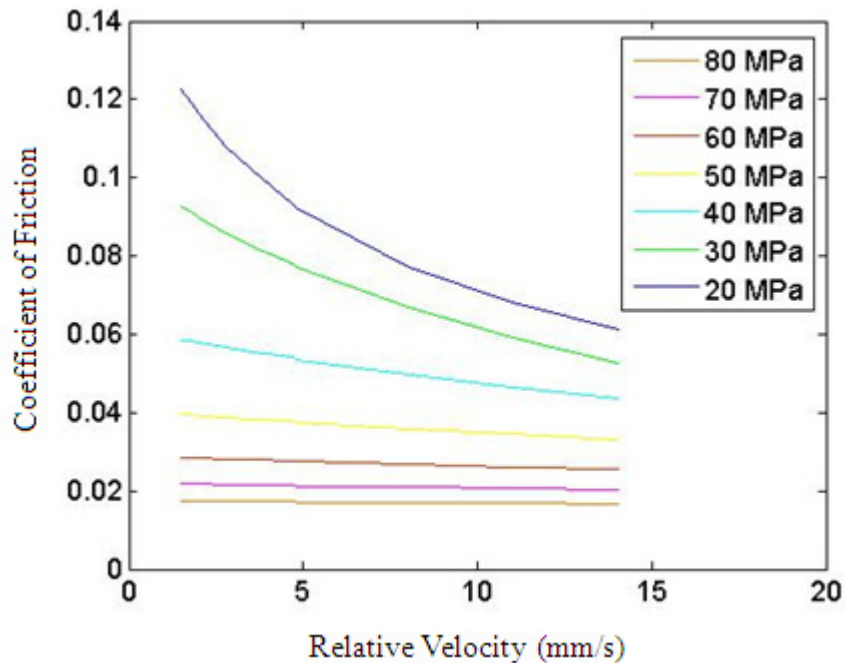


Figure C.1 Friction input data for the parameters in Table 4.3

Stribeck curves, which are obtained in the calculations of friction data, are shown in Figure C.2 at different pressures with respect to non-dimensional parameter, \mathcal{L} .

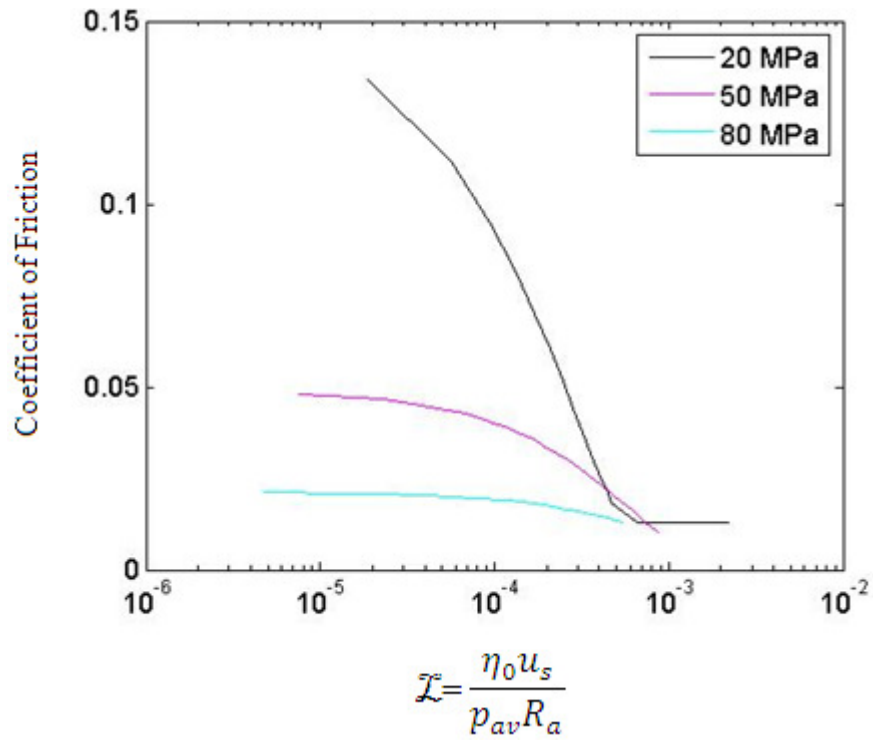


Figure C.2 Stribeck curves at different pressures

APPENDIX D

CODE OF COMBINED FRICTION MODEL

The program code of the combined friction model in MATLAB, is the following;

```
%-----  
function [] = combined()  
clc;  
clear all;  
close all;  
format long;  
warning off all;  
timeStart = cputime;  
ReadInput; % Reads inputs from ascii files.  
EqRadiusofCurvature; % Calculates equivalent radius.  
hSolver; % Calculates film thickness.  
  
global i Z ratio vf;  
vf=zeros(99,1);  
  
for i=1:1:99  
if ratio(i,1)>0.035 % Film thickness ratio criteria.  
% Calculates friction coefficient with Wilson's friction model.  
WilsonSolution;  
else  
% Calculates friction coefficient with Khonsari's friction model.  
KhonsariSolution;  
end
```

```

end

Plotter;                                % Plots the results.
timeFinish = cputime;
% Prints the CPU time into screen.
fprintf('\nTotal CPU time is = %f seconds.\n', timeFinish-timeStart);
%-----
function [] = ReadInput()                % Reads inputs from ascii files.
% Reads nodal velocities.
global Vx Vz dummy nodout count12 Vx1 Vz1;
inputFile = fopen(strcat('nodout'), 'r');
count12=1;
for i=1:4390
dummy=fgets(inputFile);
if 4290<i && i<4390
VReader;
Vx(count12,1)=Vx1*1000;                % Reads velocity in x-direction (mm/s).
Vz(count12,1)=Vz1*1000;                % Reads velocity in z-direction (mm/s).
count12=count12+1;
end
end
fclose(inputFile);
% Reads current position of the nodes.
global Cx Cy Cz ncforc count2 Cx1 Cy1 Cz1;
inputFile = fopen(strcat('ncforc'), 'r');
count2=1;
for i=1:215092
dummy=fgets(inputFile);
if 214894<i && i<215092 && mod(i,2)==1
CReader;
Cx(count2,1)=Cx1;                      % Reads x coordinate (mm).
Cy(count2,1)=Cy1;                      % Reads y coordinate (mm).

```

```

Cz(count2,1)=Cz1;          % Reads z coordinate (mm).
count2=count2+1;
end
end
fclose(inputFile);
% Reads initial position of the nodes.
global Cx1 ncforc count7 Cxini;
inputFile = fopen(strcat('ncforc'), 'r');
count7=1;
for i=1:452
dummy=fgets(inputFile);
if 254<i && i<452 && mod(i,2)==1
CReader;
Cxini(count7,1)=Cx1;      % Reads initial x coordinate (mm).
count7=count7+1;
end
end
fclose(inputFile);
% Reads nodal pressures.
global P pressure1 count3 P1;
inputFile = fopen(strcat('pressure'), 'r');
count3=1;
for i=1:(99*2)
dummy=fgets(inputFile);
if mod(i,2)==1
PReader;
P(count3,1)=(abs(P1))*power(10,9); % Reads nodal pressure (Pa).
count3=count3+1;
end
end
fclose(inputFile);
% Reads material properties.

```

```

global dummy temp k Mu0 alpha Sigmas theta c l;
global properties count8 E1 E2 v1 v2;
inputFile = fopen(strcat('properties'), 'r');
count8=1;
for i=1:22
dummy=str2num(fgets(inputFile));
if mod(i,2)==0
temp(count8,1)=dummy(1);
count8=count8+1;
end
end
k=temp(1,1); % Reads sheet shear strength (Pa).
Mu0=temp(2,1); % Reads viscosity at inlet temperature (Pa.s).
alpha=temp(3,1); % Reads pressure-viscosity index (1/Pa).
theta=(pi()/180)*temp(4,1); % Reads mean slope of tooling asperities (rad).
c=temp(5,1); % Reads adhesion coefficient.
l=temp(6,1); % Reads asperity half spacing (mm).
E1=temp(7,1); % Reads modulus of elasticity (surface 1) (Pa).
v1=temp(8,1); % Reads Poisson's ratio (surface 1).
E2=temp(9,1); % Reads modulus of elasticity (surface 2) (Pa).
v2=temp(10,1); % Reads Poisson's ratio (surface 2).
fclose(inputFile);
global EffEps dummy effepsrate count9 epsrate;
inputFile = fopen(strcat('effepsrate'), 'r');
count9=1;
for i=1:(99*3)
dummy=fgets(inputFile);
if mod(i,3)==0
EpsRateReader;
epsrate(count9,1)=1000*abs(EffEps);
count9=count9+1;
end

```

```

end
fclose(inputFile);
%-----
% Reduced code
%-----
function [] = Plotter()           % Plots the results.
global vf Cxini V Vr P ratio;
plot(Cxini,V,'k+:');             % Plots average velocity.
figure;
plot(Cxini,Vr,'k+:');            % Plots relative velocity.
figure;
scatter(Cxini,P,'o');            % Plots pressure distribution.
figure;
scatter(Cxini,ratio,'o');        % Plots film thickness ratio.
figure;
scatter(Cxini,vf,'o');           % Plots friction coefficient.
%-----

function [] = EqRadiusofCurvature() % Calculates equivalent radius.
global mx mz X Z dx2 dz2 t a0 b0 R1 R2 Req Cx Cz;
% Calculates local radius of blank.
for i=1:98
if i>1
ThriceX=[Cx(i-1,1); Cx(i,1); Cx(i+1,1)];
ThriceZ=[Cz(i-1,1); Cz(i,1); Cz(i+1,1)];
end
if i<2
ThriceX=[Cx(i+1,1); Cx(i,1); Cx(i+1,1)];
ThriceZ=[Cz(i+1,1); Cz(i,1); Cz(i+1,1)];
end
end
mx=mean(ThriceX);
mz=mean(ThriceZ);
X=ThriceX-mx;

```

```

Z=ThriceZ-mz;
dx2=mean(X.^2);
dz2=mean(Z.^2);
t=[X,Z]\(X.^2-dx2+Z.^2-dz2)/2;
a0=t(1);
b0=t(2);
R1(i,1)=sqrt(dx2+dz2+a0^2+b0^2);
end
R1(99,1)=R1(98,1);
% Calculates equivalent radius.
for i=1:99
if Cx(i,1)>16.5 && Cx(i,1)<(22.5+0.333)
R2=6;
Req(i,1)=(R1(i,1)*R2)/(R1(i,1)+R2);
end
if Cx(i,1)<16.5
Req(i,1)=R1(i,1);
end
if Cx(i,1)<29 && Cx(i,1)>(24-0.333)
R2=5;
Req(i,1)=(R1(i,1)*R2)/(R1(i,1)+R2);
end
if Cx(i,1)>29
Req(i,1)=R1(i,1);
end
end
%-----
function [] = hSolver() % Calculates film thickness.
global ratio Sigma Z P Req h V w Mu0 alpha E1 E2 v1 v2 Vx Vy Vz;
global CosAlpha1 CosBeta1 CosAlpha2 CosBeta2 Cx Cz Vr i n Beta; global Eprime
Sigmas;
% Calculates effective modulus of elasticity.

```

```

Eprime=1/((((1-v1*v1)/E1)+((1-v2*v2)/E2))*0.5);
% Calculates average velocity (mm/s).
for i=1:99
if Cx(i,1)<16.5
V(i,1)=(abs(Vx(i,1)))/2;
end
if Cx(i,1)>16.5 && Cx(i,1)<22.5+0.333
CosAlpha1=abs((abs(Cx(i,1))-16.5)/6.333);
CosBeta1=abs((6.333-abs(Cz(i,1)-Cz(1,1)))/6.333);
V(i,1)=(abs(Vx(i,1)*CosBeta1+(Vz(i,1)-10)*CosAlpha1))/2;
end
if Cx(i,1)>22.5+0.333 && Cx(i,1)<24-0.333
V(i,1)=0;
end
if Cx(i,1)>24-0.333 && Cx(i,1)<29
CosAlpha2=abs((5.333-abs(Cz(i,1)))/5.333);
CosBeta2=abs((29-abs(Cx(i,1)))/5.333);
V(i,1)=(abs(Vx(i,1)*CosAlpha2+Vz(i,1)*CosBeta2))/2;
end
if Cx(i,1)>29
V(i,1)=(abs(Vx(i,1)))/2;
end
end
n=(1.9)*power(10,10); % Defines density of asperities (m-2).
Beta=(13)*power(10,-6); % Defines average radius of asperities (μm).
Sigmas=(0.15)*power(10,-6); % Defines standard deviation of summits (μm).
Sigma=1.25*1.1*1000*Sigmas; % Defines combined surface roughness (μm).
% Calculates load per unit length (N/m).
w(i,1)=(32*Req(i,1)*P(i,1)*P(i,1))/(pi()*Eprime);
if Req(i,1)>0 && P(i,1)>0
% Calculates fim thickness (mm).
h(i,1)=1.6*(power(alpha,0.6))*(power((Mu0*V(i,1)),0.7))*

```

```

(power(Eprime,0.03))*(power(Req(i,1),0.43))/(power(w(i,1),0.13));
ratio(i,1)=h(i,1)/(Sigma);           % Calculates film thickness ratio.
Z(i,1)=h(i,1)/(3*(Sigma));          % Calculates non-dimensional film thickness.
else
h(i,1)=0;
ratio(i,1)=0;
Z(i,1)=0;
end
end
% Calculates relative velocity (mm/s).
for i=1:99
if Cx(i,1)<16.5
Vr(i,1)=abs(Vx(i,1));
end
if Cx(i,1)>16.5 && Cx(i,1)<22.5+0.333
CosAlpha1=(abs(Cx(i,1))-16.5)/6.333;
CosBeta1=abs((6.333-abs(Cz(i,1)-Cz(1,1)))/6.333);
Vr(i,1)=abs(Vx(i,1)*CosBeta1+(Vz(i,1)+10)*CosAlpha1);
end
if Cx(i,1)>22.5+0.333 && Cx(i,1)<24-0.333
Vr(i,1)=0;
end
if Cx(i,1)>24-0.333 && Cx(i,1)<29
CosAlpha2=abs((5.333-abs(Cz(i,1)))/5.333);
CosBeta2=abs((29-abs(Cx(i,1)))/5.333);
Vr(i,1)=abs(Vx(i,1)*CosAlpha2+Vz(i,1)*CosBeta2);
end
if Cx(i,1)>29
Vr(i,1)=abs(Vx(i,1));
end
end
%-----

```

```

% Calculates friction coefficient with Wilson's friction model.
function [] = WilsonSolution()
global alpha Mu0 epsrate ratio vf Mu Phif Ta Tp c k;
global Edim l theta A f1 f2 Vr Z H P Pb h Vx Vy Vz Tf;
global Cx Cz Req V i w ratio E w Sigma n Beta Sigmas Th;
if ratio(i,1)>0 && Req(i,1)>0 && P(i,1)>0
if ratio(i,1)<3
% Calculates fractional contact area.
A(i,1)=(35/32)*((16/35)-Z(i,1)+power(Z(i,1),3)-
(3/5)*power(Z(i,1),5)+(1/7)*power(Z(i,1),7));
f1(i,1)=(-0.86)*A(i,1)*A(i,1)+0.345*A(i,1)+0.515;
f2(i,1)=1/(2.571-A(i,1)-A(i,1)*(log(1-A(i,1))));
% Calculates non-dimensional strain rate.
Edim(i,1)=((epsrate(i,1)*l)/(theta*Vr(i,1)));
H(i,1)=2/(f1(i,1)*Edim(i,1)+f2(i,1)); % Calculates effective hardness.
Pb(i,1)=P(i,1)-H(i,1)*A(i,1)*k; % Calculates mean lubricant pressure (Pa).
Ta(i,1)=c*k; % Calculates adhesion friction stress component (Pa).
Tp(i,1)=theta*k*H(i,1); % Calculates plowing friction stress component (Pa).
% Calculates shear stress factor.
Phif(i,1)=(35/32)*Z(i,1)*((1-Z(i,1)*Z(i,1))*(1-Z(i,1)*Z(i,1))*(1-
Z(i,1)*Z(i,1))*log(300*Z(i,1)+300)...
+(1/60)*(-55+Z(i,1)*(132+Z(i,1)*(345+Z(i,1)*(-160+Z(i,1)*(-
405+Z(i,1)*(60+147*Z(i,1)))))))));
if Pb(i,1)>0
Mu(i,1)=Mu0*exp(alpha*Pb(i,1)); % Calculates dynamic viscosity (Pa.s).
Th(i,1)=Phif(i,1)*Mu(i,1)*Vr(i,1)/h(i,1); % Calculates hydrodynamic friction (Pa).
% Calculates friction stress (Pa).
Tf(i,1)= Ta(i,1)*A(i,1)+Tp(i,1)*A(i,1)+Th(i,1)*(1-A(i,1));
else
KhonsariSolution;
end
end
end

```

```

if ratio(i,1)<=10 && ratio(i,1)>3
% Calculates fractional contact area.
A(i,1)=(35/32)*((16/35)-Z(i,1)+power(Z(i,1),3)-
(3/5)*power(Z(i,1),5)+(1/7)*power(Z(i,1),7));
f1(i,1)=(-0.86)*A(i,1)*A(i,1)+0.345*A(i,1)+0.515;
f2(i,1)=1/(2.571-A(i,1)-A(i,1)*(log(1-A(i,1))));
% Calculates non-dimensional strain rate.
Edim(i,1)=((epsrate(i,1)*1)/(theta*Vr(i,1)));
H(i,1)=2/(f1(i,1)*Edim(i,1)+f2(i,1)); % Calculates effective hardness.
Pb(i,1)=P(i,1)-H(i,1)*A(i,1)*k; % Calculates mean lubricant pressure (Pa).
% Calculates shear stress factor.
Phif(i,1)=(35/32)*Z(i,1)*((1-Z(i,1)*Z(i,1))*(1-Z(i,1)*Z(i,1))*(1-
Z(i,1)*Z(i,1))*log((Z(i,1)+1)/(Z(i,1)-1))...
+(Z(i,1)/15)*(66+Z(i,1)*Z(i,1)*(30*Z(i,1)*Z(i,1)-80)));
Mu(i,1)=Mu0*exp(alpha*Pb(i,1)); % Calculates dynamic viscosity (Pa.s).
Th(i,1)=Phif(i,1)*Mu(i,1)*Vr(i,1)/h(i,1); % Calculates hydrodynamic friction (Pa).
Tf(i,1)=Th(i,1); % Calculates friction stress (Pa).
end
if ratio(i,1)>10
% Calculates fractional contact area.
A(i,1)=(35/32)*((16/35)-Z(i,1)+power(Z(i,1),3)-
(3/5)*power(Z(i,1),5)+(1/7)*power(Z(i,1),7));
f1(i,1)=(-0.86)*A(i,1)*A(i,1)+0.345*A(i,1)+0.515;
f2(i,1)=1/(2.571-A(i,1)-A(i,1)*(log(1-A(i,1))));
% Calculates non-dimensional strain rate.
Edim(i,1)=((epsrate(i,1)*1)/(theta*Vr(i,1)));
H(i,1)=2/(f1(i,1)*Edim(i,1)+f2(i,1)); % Calculates effective hardness.
Pb(i,1)=P(i,1)-H(i,1)*A(i,1)*k; % Calculates mean lubricant pressure (Pa).
Mu(i,1)=Mu0*exp(alpha*Pb(i,1)); % Calculates dynamic viscosity (Pa.s).
Th(i,1)=Mu(i,1)*Vr(i,1)/h(i,1); % Calculates hydrodynamic friction (Pa).
Tf(i,1)=Th(i,1); % Calculates friction stress (Pa).
end

```

```

vf(i,1)=Tf(i,1)/P(i,1);          % Calculates local friction coefficient.
else
vf(i,1)=0;
end
%-----
% Calculates friction coefficient with Khonsari's friction model.
function [] = KhonsariSolution()
global Ubar u Eprime Rprime FT l2 a hc Pm Mu alpha;
global Beta nbar n Sigmasbar Sigmas M W FTbar G L sf1 sf2;
global vf a1 a2 a3 a4 Ffc Ffh TL0 Beta0 temp hc V ratio;
global HEI HRI HEP HRP Z Mu1 Ldim guess1 guess2 lambda Cxini;
global P Vr Vx Vy Vz Cx Cz Sigma Req tempsf1 temp hc E1 E2 v1 v2 i;
if ratio(i,1)>0 && Req(i,1)>0 && P(i,1)>0
guess1=1.00001;          % Initial guess for scaling factor 1.
guess2=0.0000001;      % Initial guess for film thickness.
Mu0=0.025;             % Defines oil viscosity at inlet temperature.
Rprime=Req(i,1)*0.001; % Converts equivalent radius.
fc=0.15;               % Defines friction coefficient in BL regime.
Beta0=0.047;           % Defines rate of limiting shear stress vs pressure.
TL0=2.5*power(10,6);   % Defines limiting shear stress.
l2=0.0005;             % Defines length of line contact.
a1=1.558;              % Defines a1 constant.
a2=0.0337;             % Defines a2 constant.
a3=-0.442;             % Defines a3 constant.
a4=-1.70;              % Defines a4 constant.
u=2*V(i,1)*0.001;     % Calculates sliding velocity.
Ptemp=P(i,1);
if Req(i,1)>0 && P(i,1)>0
syms z;
func=Ptemp-(z/(2*(power(((8*z*Rprime)/(pi()*Eprime*l2)),0.5))*l2));
soln=solve(func,z);
FT=double(soln);      % Calculates total load.

```

```

% Calculates half width of Hertzian contact.
a=power((((8*FT*Rprime)/(pi()*Eprime*12)),0.5);
Pm=P(i,1);
W=FT/(Eprime*Rprime*12);           % Calculates W.
G=alpha*Eprime;                    % Calculates G.
Ubar=(Mu0*u)/(Eprime*Rprime);     % Calculates  $\bar{U}$ .
L=G*power(Ubar,0.25);              % Calculates L.
M=W*power(Ubar,-0.5);              % Calculates M.
HEI=2.621*power(M,-0.2);           % Calculates HEI.
HRI=3*(1/M);                       % Calculates HRI.
HEP=1.311*power(M,(-1/8))*power(L,0.75); % Calculates HEP.
HRP=1.287*power(L,2/3);            % Calculates HRP.
nbar=n*Rprime*power((Rprime*Beta),0.5); % Calculates  $\bar{n}$ .
Sigmasbar=Sigmas/Rprime;          % Calculates Sigmasbar.
FTbar=power((2*pi()*12*Rprime*Eprime/FT),0.5); % Calculates  $\overline{FT}$ .
solveeqs;                          % Solves 2 nonlinear equations.
Ldim(1,i)=(Mu0*u)/(Pm*Sigmas);    % Calculates lubrication number,  $\mathcal{L}$ .
Fc=FT/tempsf1;                    % Calculates asperity contact force.
Ffc=fc*Fc;                        % Calculates asperity contact friction force.
% Calculates hydrodynamic friction force.
Ffh=(TL0+Beta0*Pm)*(1-exp((-Mu)*u/(temphc*(TL0+Beta0*Pm))))*2*a*12;
vf(i,1)=(Ffc+Ffh)/FT;             % Calculates local friction coefficient.
else
vf(i,1)=0;
end
end
%-----
function solveeqs()
global resultsf1 resulthc i guess1 guess2 tempsf1 temphc;
guess=[guess1 guess2];
options =optimset('Display','off','MaxIter',50000,'TolFun',1e-7);

```

```

[result,fval,exit,output]=fsolve(@eqns,guess,options);
resultsf1(1,i)=result(1,1);
tempsf1=result(1,1);
resulthc(1,i)=result(1,2);
temphec=result(1,2);
%-----
function fcns=eqns(z)
global Ubar u hbar Eprime Rprime FT l2 a hc Pm Mu Mu0 alpha;
global Beta nbar n Sigmasbar Sigmas s eqn1 M W FTbar G L sf1 sf2;
global f a1 a2 a3 a4 eqn2 Ffc Ffh TL0 Beta0;
global HEI HRI HEP HRP Muinf Mu1;
syms x real;
sf1=z(1);
hc=z(2);
% First nonlinear equation in Khonsari's friction model.
fcns(1)=(power((power((1/(1-(1/sf1))),((1/5)*(7+8*exp((-2)*power((1/(1-(1/sf1))),-
0.4)*(HEI/HRI))))/2))*power(power(HRI,7/3)+power((1/(1-(1/sf1))),(-
14/15))*power(HEI,7/3),(3*((1/5)*(7+8*exp((-2)*power((1/(1-(1/sf1))),-
0.4)*(HEI/HRI))))/7))+power((1/(1-(1/sf1))),(-(1/5)*(7+8*exp((-2)*power((1/(1-
(1/sf1))),-0.4)*(HEI/HRI))))/2))*power(power(HRP,(-7/2))+power(HEP,(-7/2)),(-
2*((1/5)*(7+8*exp((-2)*power((1/(1-(1/sf1))),-
0.4)*(HEI/HRI))))/7)),(1/((1/5)*(7+8*exp((-2)*power((1/(1-(1/sf1))),-
0.4)*(HEI/HRI))))))*power((1/(1-(1/sf1))),0.5)-(hc/Rprime)*power(Ubar,-0.5);
% Second nonlinear equation in Khonsari's friction model.
fcns(2)=((power((1+power((a1*power(nbar,a2)*power(Sigmasbar,a3)*power(W,(a2
-a3)*power((1/(1-(1/sf1))),a2)),a4)),(1/a4)))*(1/sf1))-
(2/3)*nbar*power(Sigmasbar,1.5)*FTbar*(1/power(2*pi(),0.5))*double(int((power((
x-((hc/Rprime)-1.15*Sigmasbar)/Sigmasbar)),(3/2)).*exp(x.*x*(-
0.5))),x,((hc/Rprime)-1.15*Sigmasbar)/Sigmasbar,10));
%-----

```